Dynamics and Stability of Gravity–Capillary Solitary Waves

by

David C. Calvo

B.S., Mechanical Engineering (1995)
Carnegie Mellon University

M.S.M.E., Mechanical Engineering (1997)
Massachusetts Institute of Technology

Submitted to the Department of Mechanical Engineering
in partial fulfillment of the requirements for the degree of

Doctor of Philosophy in Mechanical Engineering

at the

MASSACHUSETTS INSTITUTE OF TECHNOLOGY

February 2001

Signature of Author ____________________
Department of Mechanical Engineering
September 13, 2000

Certified by ____________________
Triantaphyllos R. Akylas
Professor of Mechanical Engineering
Thesis Supervisor

Accepted by ____________________
Ain A. Sonin
Professor of Mechanical Engineering
Chairman, Graduate Committee

Dynamics and Stability of Gravity–Capillary Solitary Waves

by

David C. Calvo

Submitted to the Department of Mechanical Engineering
on September 13, 2000 in partial fulfillment
of the requirement of the degree of
Doctor of Philosophy in Mechanical Engineering

ABSTRACT

Over the past several years, it has been recognized that a new class of solitary waves can propagate in nonlinear dispersive wave systems if the phase speed of linear waves attains a local extremum at some finite wavenumber. Near such a point, solitary waves in the form of small-amplitude wavepackets can be obtained for which the phase speed of the carrier oscillations matches the group speed of their envelope. Such an extremum is found in the analysis of water waves when the restoring forces of both gravity and surface tension are taken into account, and certain kinds of these gravity–capillary solitary waves have been observed in experiments. While past theoretical studies have focussed mainly on determining steady solitary wave profiles, very little work has been done on examining their stability properties which is the thrust of this thesis.

Beginning in the weakly nonlinear regime, an asymptotic analysis of linear stability is presented and comparison is made with numerical computations. Contrary to predictions of the nonlinear Schrödinger (NLS) equation, some free solitary wave types are found to be unstable owing to exponentially effects terms that lie beyond standard two-scale perturbation theory. Moreover, numerical simulations show that unstable gravity–capillary solitary waves may decompose into stable solitary waves that have soliton properties. Stability results are then extended to the fully nonlinear regime to treat both free and forced situations using numerical techniques to solve the full hydrodynamic equations in steady form. A dramatic difference is found between the linear stability of free and forced waves in both weakly and fully nonlinear cases, and results obtained here are compared with laboratory experiments.

The analysis followed in the free-surface problem is then generalized to examine the dynamics of gravity–capillary interfacial solitary waves in a layered two-fluid system. Here, the linear stability and limiting wave forms of free solitary waves are determined over a range of system parameters using the full hydrodynamic equations. Finally, a related problem of gravity–capillary envelope solitons is considered under the general situation of unequal phase and group speeds. By asymptotic and numerical techniques it is found that envelope solitons are generally nonlocal—tails are radiated owing to a resonance mechanism that is beyond the NLS equation.

Thesis Supervisor: Triantaphyllos R. Akylas
Title: Professor of Mechanical Engineering

ACKNOWLEDGMENTS

I would foremost like to thank Professor Akylas for introducing me to the beautiful and fascinating subject of wave propagation which I have enjoyed immensely. I feel fortunate to have had his enduring support and guidance over the years, and I like to think that many of his good qualities have rubbed off on me. I would also like to thank Professors Mei and Mahadevan for serving on my thesis committee. Their comments and suggestions helped to improve this work.

Over the years, my parents and my sister provided me with a constant source of encouragement for which I have been grateful. I have also been very fortunate to have made some good friends while at MIT particularly Debbie Blanchard, Matt Lim, Kevin Davis, Julie Eisenhard, Dilip Prasad, and Missy Allen. In addition to providing an ear when I needed one, Debbie was also extremely helpful with typesetting advice. Chapter 5 was in fact typed by Debbie. I am also thankful for the encouragement and levity provided by my long-time friends William Ouyang, Daniel Kammerer, and Matthew Campbell over the course of graduate school.

This work was supported by the Air Force Office of Scientific Research, Air Force Materials Command, USAF, under Grant Numbers F49620-98-1-0388, F49620-95-1-0047, F49620-95-1-0443, and by the National Science Foundation Grant Number DMS-9701967 and INT-9512852. This work was partially supported by National Computational Science Alliance under a start-up allocation and utilized the NCSA SGI/CRAY Origin2000.

CONTENTS

LIST OF FIGURES

LIST OF TABLES

CHAPTER 1

GENERAL INTRODUCTION

1.1 Background

Remarkable strides have been made in understanding the effects of finite wave amplitude on dispersive wave phenomena over the past few decades. Much of the progress in this area of dispersive wave propagation has occurred in the study of water-wave dynamics where the effects of nonlinearity and dispersion are easily observed. For example, the self-steepening and eventual breaking of an ocean wave as it approaches a beach is a nonlinear effect with which most everyone is familiar. A careful observer who has ever tossed a pebble into a deep body of water and noticed that longer waves advance faster than shorter waves is also familiar with the effect of dispersion. An interplay between these two effects gives rise to a special phenomenon known as a solitary wave which can be observed in a variety of wave systems and is the general topic of this thesis.

More than just a simple pulse, a solitary wave exhibits an unusual amount of stability and propagation duration in comparison with smaller amplitude waves which disperse rapidly in the absence of nonlinear effects. These stable qualities first caught the eye of John Scott Russell in 1834 while observing a heap of water set into motion by an impulsively started carriage that was being pulled through a shallow canal. So impressed by the solitary wave's endurance, he followed it on horseback for some distance and also conducted a series of experiments to generate solitary waves. In modern times, it is now recognized that, in some instances, solitary waves may evolve out of general initial conditions, emerge intact from collisions with each other, and can be resonantly generated by moving forcing disturbances. Solitary waves possessing these attributes are popularly known as solitons (Newell 1985).

Much of the progress in theoretically analyzing solitary waves has centered on studying the weakly nonlinear and weakly dispersive propagation regimes in which approximations to the full and often complicated governing equations can be made to obtain simpler model equations. The two most famous model equations which form the pillars of modern nonlinear dispersive wave theory are the Korteweg–de Vries (KdV) equation and nonlinear Schrödinger (NLS) equation. As these equations will be referred to throughout this thesis, a presentation of some general background is warranted.

In water-wave theory, the KdV equation governs the free-surface profile of a unidirectional wave that is very long in comparison with the water depth (a weakly dispersive condition) with an amplitude that is small in comparison with the depth (a weakly nonlinear condition). Under these circumstances, the waveform essentially propagates with the characteristic long-wave speed and is slowly modified by weak dispersion and nonlinearity.

Whereas the KdV equation governs disturbances with very long wavelength, the NLS equation governs the amplitude and phase of a wavetrain with an essentially uniform and finite carrier wavelength. The condition of weak dispersion is satisfied on account of a small amount of modulation about the dominant wavelength, and therefore does require the water depth to be shallow. Weak nonlinear effects again require the amplitude to be small in comparison with some finite length (the carrier wavelength, say). Under these conditions, the wavetrain propagates at the group velocity corresponding to the carrier wavelength and is slowly modified by weak dispersion and nonlinearity.

Based on these two model equations, a great deal of rigorous work has been done in examining mathematical solutions to their initial-value problems using the inverse-scattering transform (Ablowitz & Clarkson 1991). It is now well established that both equations possess a solitary wave solution and their soliton dynamics can be precisely described. A key difference between the significance of each solution, however, is that the solitary wave of the KdV equation, a $\mathrm{sech}^2(x)$ function, physically represents the displacement of the water surface, while the $\mathrm{sech}(x)$ solution of the NLS equation only represents the envelope of a wavepacket. In other words, if one adopts a reference frame moving at the envelope propagation speed (the group speed), one sees crests passing by at the phase speed which is generally different from the group speed. Hence, the wave group as a whole is unsteady and is usually termed an envelope soliton instead of a solitary wave to distinguish it from a solution which can be made steady in a reference frame moving with the wave speed.

As indicated above, KdV solitary waves can propagate in water of finite depth only. Only over the past decade, however, a new class of solitary wave has been discovered which can propagate on deep water. The origin of this new class of solitary waves can be intuitively understood by examining the consequences of the phase speed $c = \omega/k$ being stationary at some finite wavenumber:

$$\frac{\mathrm{d}}{\mathrm{d}k}\left(\frac{\omega}{k}\right) = \frac{1}{k}\left(\frac{\mathrm{d}\omega}{\mathrm{d}k} - \frac{\omega}{k}\right) = 0. \tag{1.1}$$

From (1.1) it is clear that at an extremum of the phase speed, the group speed ω' equals the phase speed ω/k, and so if one adopts a reference frame moving with the envelope of a slowly varying wavetrain the crests do not appear to translate. Furthermore, in the special case of a small-amplitude narrow-band wavepacket, the localized envelope is expected to satisfy the steady NLS equation, so as a whole the envelope soliton is truly a solitary wave in this instance (Akylas 1993). Because this argument is fairly general, it is expected that solitary waves belonging to this new class may arise in dispersive wave systems with local extrema in their phase speed relations (so that k is finite); two such systems will be considered in detail in the next chapter. In addition to having an extremum in the phase speed relation, the sign of the nonlinear term must be the same as the sign of the dispersive term in the NLS equation; this is the so-called anomalous dispersion regime and is necessary for $\operatorname{sech}(x)$ to be an acceptable solution of the steady NLS equation. This thesis is dedicated to examining the dynamics and stability of this new class of solitary waves with a focus on gravity–capillary waves arising in the water-wave problem with surface tension which will now be discussed.

The phase speed relation for gravity–capillary waves in deep water reads

$$c^2 = \frac{g}{k} + \frac{T}{\rho}k, \tag{1.2}$$

a plot of which is shown in Figure 1–1. Here, g is the gravitational acceleration, ρ is the liquid density, and T is the coefficient of surface tension. It is customary to refer to the

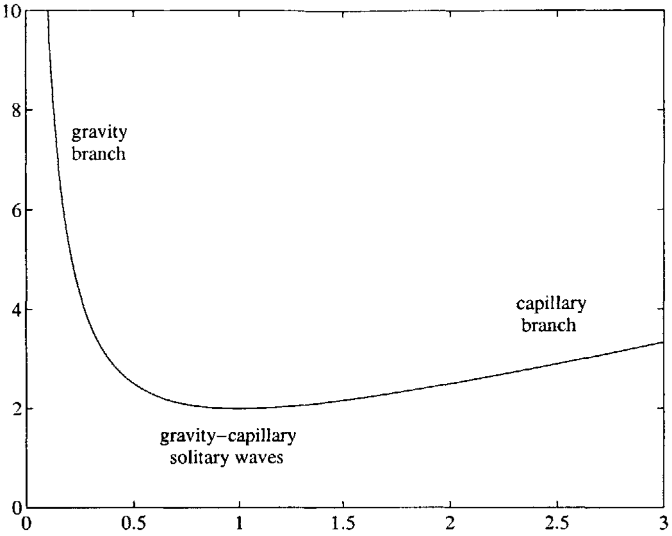

FIGURE 1–1. Linear phase speed relation for gravity–capillary waves in deep water. The square of the dimensionless phase speed $c^2(\rho/gT)^{\frac{1}{2}}$ is plotted on the vertical axis against the dimensionless wavenumber $k(T/\rho g)^{\frac{1}{2}}$.

phase speed relation as having two branches: a gravity branch for $(k \ll 1)$ and a surface tension dominated capillary branch for $(k \gg 1)$. These branches merge at $c_{\min} = (4gT/\rho)^{\frac{1}{4}}$ where $k = (\rho g/T)^{\frac{1}{2}}$; both gravity and surface tension effects are equally important there. For physical reference, these quantities translate to a speed of 23.1 cm/s and a wavelength of 1.72 cm for typical conditions. It is clear from (1.2) that a minimum, and hence this new class of solitary wave, cannot be obtained without including the effect of surface tension. In addition, a locally confined solitary wave is only possible if the wave speed is below the minimum phase speed, for if the solitary wave speed is used in (1.2), the corresponding roots k must have complex parts signifying the decaying oscillatory behavior of the small-amplitude tails of a wavepacket.

Historically, gravity–capillary solitary waves in deep water were first computed numerically by Longuet-Higgins (1989) using the full water-wave equations; the connection with small-amplitude envelope solitons as described by the NLS equation was not recognized until later (Akylas 1993; Longuet-Higgins 1993). The initial calculations of Longuet-Higgins revealed a symmetric (about a vertical plane) wave of depression with a steep trough and relatively flat crests. Further numerical work by Vanden-Broeck & Dias (1992) revealed a symmetric elevation solitary wave for which a crest lies on the plane of symmetry. An

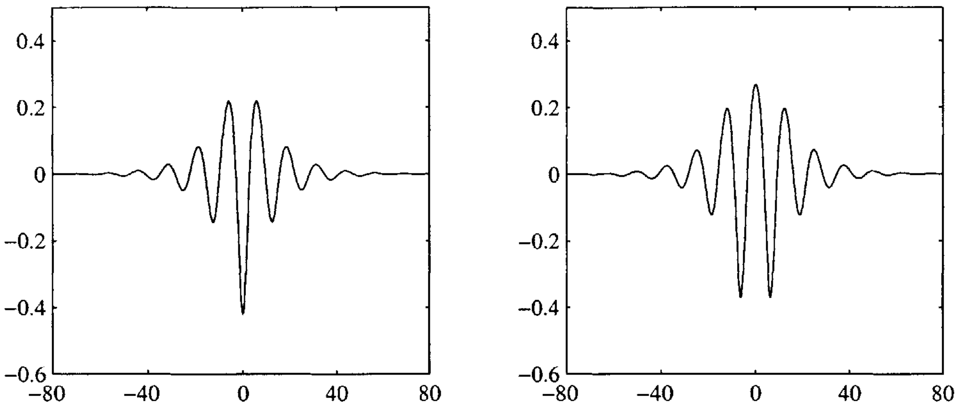

FIGURE 1–2. Free-surface profiles of small-amplitude depression (left) and elevation (right) gravity–capillary solitary waves with normalized speeds $c(\rho/gT)^{\frac{1}{4}} = 1.4045$. The length scale is $T/\rho c^2$.

example of both elevation and depression waves is shown in Figure 1–2.

When followed to large amplitude, the elevation wave turns into a solitary wave consisting of pair of overlapping depression waves. In fact, there is sufficient numerical evidence that there may be an infinity of gravity–capillary solitary waves that exist only at finite amplitude which resemble multi-packet waves (Yang & Akylas 1997). On the experimental side, steep gravity–capillary solitary waves have been observed experimentally in natural settings and in the laboratory (Zhang 1995; Longuet-Higgins & Zhang 1997; Zhang 1999). Apart from the free-surface problem, solitary waves of this new kind have also been theoretically identified in a layered two-fluid system (Benjamin 1992; 1996) and also in solid mechanics problems (Chen & McKenna 1997).

Early in the study of gravity–capillary solitary waves, it was observed that two important aspects revealed by numerical computation could not be explained solely on the the basis of the NLS theory. First, viewing the solitary wave as an envelope soliton, it would appear that generally asymmetric solitary waves with a 'sech' envelope should exist as these waves would correspond to shifting the carrier oscillations of the wavepacket relative to its envelope. This hypothesis could not be supported by numerical findings, however, as only two kinds of symmetric solitary-wave solutions could be found, also consistent with rigorous existence proofs (Zufiria 1987; Iooss & Kirchgassner 1990; Vanden-Broeck & Dias 1992; Champneys & Toland 1993; Buffoni *et al.* 1995). Second, based on the fifth-order KdV equation—a model for gravity–capillary waves in finite depth when the Bond number is close to $\frac{1}{3}$—

elevation solitary waves appear to be unstable, but depression waves are stable contrary to the predictions of the NLS theory which views both of these solutions as the same (stable) envelope soliton (see Chapter 2).

The cause of these discrepancies is that the NLS equation and its higher-order extensions only govern the wavepacket envelope which is uncoupled from the phase of the carrier oscillations. Based on the fifth-order KdV equation, Yang & Akylas (1997) carried the two-scale expansion underlying the NLS equation beyond all orders and showed that only symmetric elevation and depression waves bifurcate at the minimum value of the linear phase speed relation consistent with previous findings. The exponentially small effects they found which preclude the existence of asymmetric singe-packet solitary waves turn out to influence the stability properties of elevation and depression waves, and this will be discussed in Chapter 2.

1.2 Outline of this thesis

The dynamics and stability of this new class of solitary wave will be examined mostly in the gravity–capillary free-surface problem using both the fifth-order KdV equation (Chapters 2 & 5) and the full water-wave equations (Chapter 3). The goal of Chapter 2 is to clarify how exponentially small terms affect the stability of small-amplitude elevation and depression wave solution branches near the bifurcation point. The stability analysis presented there will also be applied to the case of solitary waves propagating on a beam with a nonlinear elastic foundation. In addition, a related problem on the stability of localized buckling states will be discussed as the equilibrium solution arising in this case satisfies the same equation found in the small-amplitude wave problems yet the stability properties are entirely different.

As the experimental measurements of gravity–capillary depression solitary waves have found them to be quite steep, the stability analysis in Chapter 2 is extended to large amplitude solving the full water-wave equations using numerical methods. Two cases of steep solitary waves will be considered: a free problem in which there is no external forcing and a forced problem in which a localized pressure distributions acts on the free surface. This latter case corresponds to the experimental situation considered in Longuet-Higgins & Zhang (1997).

In Chapter 4, the general case of gravity–capillary solitary waves in a layered two-fluid system will be studied in a manner somewhat parallel to the free-surface case. In the small-amplitude limit, interfacial gravity–capillary solitary waves will be computed on the basis of the Benjamin equation—a model equation for weakly nonlinear long waves when interfacial tension is relatively large and the fluid densities are close. The possibility of soliton behavior will be considered by direct time-dependent integration of the Benjamin equation. In the more general case of moderate interfacial tension and general density ratios, the full hydrodynamic equations in steady form will be numerically solved to extend the qualitative picture of gravity–capillary interfacial solitary waves predicted using Benjamin's equation. As it turns out, additional parameters in the two-fluid problem not arising in the free-surface problem can dramatically change which kinds of solutions are stable.

Finally, in Chapter 5, the free-surface problem is again considered with the goal of determining the stability of gravity–capillary envelope solitons in the general case when there is a mismatch between the phase and group speeds. Using the fifth-order KdV equation, it is found using both numerical and asymptotic methods that envelope solitons are generally nonlocal: special resonance conditions can be found for which linear waves are radiated by the soliton with an amplitude that depends on the bandwidth of the wavepacket.

CHAPTER 2

STABILITY OF SMALL-AMPLITUDE SOLITARY WAVES WITH DECAYING OSCILLATORY TAILS

2.1 Introduction

Under the condition that the solitary wave speed is close to the local extremum of the linear phase speed relation, solitary waves belonging to the new class have small peak amplitudes and decaying oscillatory tails. In this wavepacket regime, the envelopes of these solitary waves may be interpreted as solitons of the nonlinear Schrödinger (NLS) equation and so both elevation and depression wave types would appear to be stable. In this chapter, it will be shown that contrary to the predictions of the NLS theory, elevation solitary waves are in fact linearly unstable. As it turns out, the instability growth rates are exponentially small in the small-amplitude limit and hence the instability mechanism lies beyond the standard two-scale expansion underlying the NLS equation.

The role of exponentially small terms in deciding stability is closely related to the fact that the elevation and depression symmetric-wave types, which belong to a more exclusive class than that predicted by the NLS theory, can only be identified if these terms are taken into account. Specifically, the terms derived by Yang & Akylas (1997) to identify the conditions for a localized steady solution of the fifth-order Korteweg–de Vries (KdV) equation turn out to be crucial in determining the conditions for a localized (unstable) eigenfunction in the stability problem. Here, an asymptotic analysis of the eigenvalue problem that draws on the exponentially small terms derived in the steady problem will be presented which is valid if the instability growth rate is small—a condition which is expected to be true near the bifurcation point at zero amplitude. Although these exponentially small terms translate to dimensionless growth rates that are extremely small near the bifurcation point, they appear to decide the stability of much of the elevation and depression solitary wave branches over a range of speeds where the wave amplitude is moderate to large. This will be considered further in the next chapter.

The stability of this new class of solitary wave will first be demonstrated in the context of the gravity–capillary water-wave problem based on the fifth-order KdV equation which will be briefly derived. After presenting results of a numerical simulation showing the stable and unstable dynamics of gravity–capillary solitary waves, the asymptotic analysis of the stability eigenvalue problem will be described in detail and comparison will be made with numerical results.

In addition to applying the stability theory to the gravity–capillary wave problem, an example will be drawn from wave propagation in solid mechanics in which a phase speed minimum arises and solitary waves of the new class can be obtained. In particular, the propagation of solitary waves on a Bernoulli–Euler beam resting on a nonlinear elastic foundation will be considered. Again, it is found that elevation solitary waves are unstable with exponentially small growth rates. A closely related problem of localized buckling will also be considered which has received attention in the literature over the last few years (Champneys *et al.* 1997). As it turns out, finite-amplitude localized buckled states satisfy the same governing equation that arises in the wave propagation problems, but instability growth rates in this case turn out to be algebraic and can therefore be captured with standard multiple scaling techniques.

2.2 Steady wave equations

Although there are differences between the time-dependent wave equations arising in the fluid mechanics and solid mechanics problems as will be discussed, in both cases steady solitary waves satisfy the same nonlinear ordinary differential equation which reads (after a suitable rescaling of variables)

$$-cu + u_{\xi\xi} + u_{\xi\xi\xi\xi} + 3u^2 = 0 \qquad -\infty < \xi < \infty, \tag{2.1}$$

subject to the boundary conditions

$$u \to 0 \qquad (\xi \to \pm\infty), \tag{2.2}$$

where the parameter c represents a dimensionless speed. By linearizing (2.1) and looking for solutions $\propto \exp(ik\xi)$ it may be shown that the transition from pure real roots to mixed roots, which describes the bifurcation of solitary waves with decaying oscillatory tails from infinitesimal periodic waves, is obtained when c is slightly below the value of $-\frac{1}{4}$.

While an exact nonlinear solution of (2.1) is not known, Champneys & Toland (1993) and Buffoni *et al.* (1995) proved the existence of an infinite number of homoclinic orbits corresponding to solitary waves. Asymptotic approximations of solitary waves near the bifurcation point were first obtained by Grimshaw *et al.* (1994) using the higher-order nonlinear Schrödinger (NLS) equation. The expansion was then extended beyond all orders using techniques of exponential asymptotics by Yang & Akylas (1997) who showed that only elevation and depression solution branches are possible. In the latter study, it was also shown that (2.1) admits multi-packet solitary waves that exist only at finite amplitude, but our interest here centers only on the stability of single-packet solitary waves.

A modified form of (2.1) in which the quadratic nonlinearity is replaced by cubic nonlinearity will also be considered:

$$-cu + u_{\xi\xi} + u_{\xi\xi\xi\xi} - 2u^3 = 0. \tag{2.3}$$

In contrast to the problems with quadratic nonlinearity, solitary waves bifurcate from zero-amplitude only if a minus sign is present in front of the nonlinear term. In addition, there is no longer any distinction between elevation and depression solitary waves because of the invariance under the change $u \to -u$. Instead, using an analysis taking into account exponentially small terms, Wadee & Bassom (1999) found that symmetric and anti-symmetric solitary waves are possible. In this problem, it will be found that the former solution type is stable while the latter is unstable.

While the solitary waves to be discussed in this chapter satisfy (2.1) or (2.3), the specific forms of the stability eigenvalue problems depend on the time-dependent wave equations from which these steady equations are derived. In the gravity–capillary water-wave problem, (2.1) is derived from the fifth-order Korteweg–de Vries (KdV) equation which features a first-order time derivative along with third and fifth-order dispersive terms. The modified version of the steady fifth-order KdV (2.3) arises under special conditions in the layered two-fluid interfacial-wave problem for special depth and density ratios (Laget & Dias 1997). In the solid mechanics problem, (2.1) is derived from the governing equation for a Bernoulli–Euler beam resting on a nonlinear elastic (quadratic hardening) foundation. The dynamical equation differs from the fifth-order KdV in that it features a second-order time derivative and an even-order dispersive term. In this beam problem, the modified equation (2.3) is related to the fact that the beam rests on a cubic softening foundation.

2.3 Time-dependent wave equations

2.3.1 Fifth-order Korteweg–de Vries equation

The description of small-amplitude gravity–capillary waves in this chapter as well in Chapter 5 will be based on the fifth-order KdV equation; a short derivation is provided here. A full derivation can be found in Hunter & Scheurle (1988).

The dispersion relation for linear gravity–capillary surface waves propagating to the right in water of finite depth h reads

$$\omega = \frac{c_0}{h}\left[\left(1 + Bk^2h^2\right) kh \, \mathrm{tanh} kh\right]^{\frac{1}{2}}, \tag{2.4}$$

where $c_0 = \sqrt{gh}$ is the long-wave speed and $B = T/\rho g h^2$ is the Bond number; the surface-tension coefficient is given by T, the liquid density by ρ, and the gravitational acceleration by g.

By considering waves that are long in comparison with the depth ($kh \ll 1$), (2.4) may be expanded as

$$\omega = c_0 k \left[1 + \tfrac{1}{2}(B - \tfrac{1}{3})(kh)^2 + \tfrac{1}{4}\left(\tfrac{14}{90} - B^2\right)(kh)^4 + O[(kh)^6]\right]. \tag{2.5}$$

It is easy to see that if B is slightly below $\frac{1}{3}$ ($B - \frac{1}{3} \sim O[(kh)^2]$), then a balance between the third and fifth-order dispersive terms can be obtained. The minimum of the phase speed relation is then obtained for $kh < 1$ and so this balance translates physically to a balance between gravity and surface tension effects. Using this condition on B, and taking into account the leading-order effects of self-steepening in shallow water, one may infer the fifth-order KdV equation

$$\eta_t + c_0\eta_x + \frac{3c_0}{2h}\eta\eta_x + \tfrac{1}{2}c_0h^2\left(\tfrac{1}{3} - B\right)\eta_{xxx} + \tfrac{1}{4}c_0h^4\left(\tfrac{14}{90} - B^2\right)\eta_{xxxxx} = 0. \tag{2.6}$$

Adopting a reference frame moving with the long-wave speed, and adopting a 'slow' time and 'stretched' space variable, the following dimensionless form can be obtained

$$u_t + u_{xxx} + u_{xxxxx} + 6uu_x = 0. \tag{2.7}$$

By seeking localized travelling wave solutions of the form $u = u(x - ct)$, (2.1) can be obtained after one integration.

In the more general case of a layered two-fluid system, an equation analogous to (2.6) can be obtained with more complicated coefficients owing to additional physical parameters (Laget & Dias 1997). The additional freedom due to these parameters has some interesting consequences on stability as will be discussed in Chapter 4.

2.3.2 Bernoulli-Euler beam on a nonlinear elastic foundation

In solid mechanics problems involving flexural waves on a beam supported by a quadratic-hardening elastic foundation, the vertical displacement of the beam is governed by the dimensionless equation

$$w_{tt} + w_{xxxx} + w + 3w^2 = 0, \tag{2.8}$$

where in the derivation it is assumed that the slope of the vertical displacement is small (see, for example, Lindberg & Florence 1987). The nonlinear effects are then confined to the elastic foundation which is reflected by the last two terms in (2.8). It can be shown by standard methods that the linear phase speed relation has a local minimum and hence solitary waves akin to the gravity-capillary type are possible in the neighborhood below the minimum phase speed. By seeking travelling wave solutions of the form $w = \bar{w}(\eta)$ ($\eta = x - vt$) equation (2.1) directly follows after using the transformation $\xi = v\bar{\eta}$, $u = v^{-4}\bar{w}$ and $c = -v^{-4}$.

Numerical simulations of an evolution equation very similar to (2.8) performed by Chen & McKenna (1997) indicate that, as found in the gravity–capillary wave problem, elevation solitary waves are unstable in this instance while depression waves are stable. This result will also be confirmed in this chapter using the asymptotic analysis.

2.3.3 Axially-compressed nonlinear beam equation

A modified form of (2.7) which can be used to model localized buckling reads

$$w_{tt} + Pw_{xx} + w_{xxxx} + w + 3w^2 = 0, \tag{2.9}$$

where the second-order spatial-derivative term derives from an axially compressive load placed on the beam when $P > 0$. Localized equilibria can be obtained by setting w_{tt} equal to zero. Upon using the transformation $\xi = P^{\frac{1}{2}}x$, $u = P^{-2}\bar{w}$, and $c = -P^{-2}$ equation (2.1) is once again obtained. For $P < 2$ ($c < -\frac{1}{4}$) it has been proven by Sandstede (1997) that the primary 'single-packet' buckling mode (which represents both an elevation or a depression wave) which bifurcates from zero amplitude is unstable under the condition of dead loading in which P is constant and w adjusts according to (2.1). While the stability of this case is a settled problem, the instability growth rates obtained in the buckling problem provide an interesting contrast with those obtained in the solitary wave problems and so a small-amplitude treatment of the localized buckling problem will be discussed.

2.4 Solitary-wave solutions

The two-scale expansion of Grimshaw *et al.* (1994) of a solitary wave solution $u = \bar{u}(\xi)$ in which the speed is defined as $c = -\frac{1}{4} - 2\epsilon^2$, $(0 < \epsilon \ll 1)$ reads

$$\begin{aligned}\bar{u} \;=\; & \sqrt{\tfrac{2}{19}}\,\epsilon\cos(k_{\mathrm{m}}\xi+\phi_0)\,\mathrm{sech}X \;+\epsilon^2\Big\{\tfrac{187}{57\sqrt{19}}\sin(k_{\mathrm{m}}\xi+\phi_0)\,\mathrm{sech}X\,\tanh X \\ & -\tfrac{4}{19}\left(3+\tfrac{1}{3}\cos 2(k_{\mathrm{m}}\xi+\phi_0)\right)\mathrm{sech}^2X\Big\}+O(\epsilon^3),\end{aligned} \tag{2.10}$$

where $X = \epsilon\xi$, and $k_{\mathrm{m}} = \frac{1}{\sqrt{2}}$. Although to polynomial order (2.10) appears to be locally confined, a revised perturbation theory which takes into account exponentially small terms can reveal the presence of nonlocal terms. Specifically, assuming that $\bar{u}$ decays exponentially far upstream so that

$$\bar{u} \sim \sqrt{\tfrac{8}{19}}\,\epsilon\,\mathrm{e}^X\cos(k_{\mathrm{m}}\xi+\phi_0) \qquad (\xi\to-\infty), \tag{2.11}$$

the analysis of Yang & Akylas (1997) shows that both exponentially growing and decaying oscillatory tails generally appear downstream

$$\bar{u} \sim \frac{-16\pi D}{\epsilon^3}\exp\left(-\frac{\pi k_{\mathrm{m}}}{2\epsilon}\right)\sin\phi_0\,\mathrm{e}^X\cos(k_{\mathrm{m}}\xi+\phi_0)+\sqrt{\tfrac{8}{19}}\,\epsilon\,\mathrm{e}^{-X}\cos(k_{\mathrm{m}}\xi+\phi_0) \qquad (\xi\to\infty), \tag{2.12}$$

where $D = 0.0023$. From this expression it is clear that localized solitary waves can only be obtained for $\sin\phi_0 = 0$ $(\phi_0 = 0, \pi)$ in which case the solitary wave is symmetric. Elevation solitary waves are then obtained for $\phi_0 = 0$ while depression waves are obtained for $\phi_0 = \pi$.

It is important to note that (2.12) is the leading-order result of the analysis using exponential asymptotics. In fact, for a fixed value of the upstream phase constant ϕ_0 in (2.11), the downstream carrier oscillations in (2.12) undergo an $O(\epsilon)$ phase shift due to the $O(\epsilon)$ correction to the fundamental oscillation appearing in (2.10). Therefore, in addition to the growing term proportional to $\cos(k_{\mathrm{m}}\xi + \phi_0)$ appearing downstream, a relatively smaller amount of growing oscillations proportional to $\sin(k_{\mathrm{m}}\xi + \phi_0)$ is expected to appear but the precise amplitude of this term would require carrying the exponential asymptotics to higher order. For later purposes, however, this higher-order term may be written as

$$\frac{\sigma}{\epsilon^2} \exp\left(-\frac{\pi k_{\mathrm{m}}}{2\epsilon}\right) \sin\phi_0 \, \mathrm{e}^X \sin(k_{\mathrm{m}}\xi + \phi_0), \tag{2.13}$$

where $\sigma = O(1)$.

As the numerical constant D will play a crucial role in deciding stability, its significance is worthy of discussion. To capture the exponentially small terms, the expansion (2.10) must be extended beyond all orders in ϵ. This task can be performed most efficiently by working with the Fourier transform of $\bar{u}$ with respect to X. In the wavenumber domain, the expansion becomes nonuniform near its singularities near the real axis which correspond to exponentially growing far-field solutions. The residues of these singularities is partly determined by solving an integral equation in which all harmonics are strongly coupled. The asymptotic behavior of the solution of this integral equation near the singularities is proportional to D and so this constant contains information from all harmonics in (2.10).

A small-amplitude localized solution $u = \bar{u}(\xi)$ of the cubic equation (2.4) was constructed in a similar way by Wadee and Bassom (1999) who found that for $c = -\frac{1}{4} - 2\epsilon^2$

$$\begin{aligned} \bar{u} \;=\; & \frac{4}{\sqrt{6}}\,\epsilon \cos(k_{\mathrm{m}}\xi + \phi_0)\,\mathrm{sech}X \;+ 2\sqrt{3}\,\epsilon^2 \sin(k_{\mathrm{m}}\xi + \phi_0)\,\mathrm{sech}X\,\tanh X \\ & + \frac{\epsilon^3}{3\sqrt{6}} \cos 3(k_{\mathrm{m}}\xi + \phi_0)\,\mathrm{sech}^3 X + O(\epsilon^3). \end{aligned} \tag{2.14}$$

By using techniques of exponential asymptotics in a manner similar to Yang & Akylas (1997), it can be shown that by requiring $\bar{u} \to 0$ as $x \to -\infty$ both exponentially growing and decaying oscillations appear downstream:

$$\bar{u} \sim -\frac{16\pi D'}{\epsilon^3} \exp\left(-\frac{\pi k_{\mathrm{m}}}{\epsilon}\right) \sin 2\phi_0 \, \mathrm{e}^{X} \cos(k_{\mathrm{m}}\xi + \phi_0) + \frac{8}{\sqrt{6}} \epsilon \, \mathrm{e}^{-X} \cos(k_{\mathrm{m}}\xi + \phi_0) \qquad (\xi \to \infty), \tag{2.15}$$

where the constant $D' = -0.32$. From (2.15) it is clear that a localized solitary wave is only obtainable when $\sin 2\phi_0$ vanishes. The possibilities of $\phi_0 = 0$ and $\phi_0 = \pi$ correspond to symmetric states while $\phi_0 = \pm\frac{\pi}{2}$ corresponds to anti-symmetric states. Again, (2.15) is only the leading-order result; a relatively smaller amount of growing oscillations proportional to $\sin(k_{\mathrm{m}}\xi + \phi_0)$ are also expected to appear downstream.

2.5 Time-dependent simulations

In this section, results of a numerical time-dependent integration of (2.7) is presented using elevation solitary waves as initial conditions. These initial conditions are obtained by numerically solving (2.1) in the following way. Working on the half-domain $0 \le \xi \le \xi_\infty$, where ξ_∞ is a sufficiently large value, (2.1) is numerically integrated using a fourth-order Runge–Kutta method starting with the approximate downstream behavior

$$u \sim a_+ \, \mathrm{e}^{-\epsilon\gamma\xi} \cos(k_c\xi + \phi_+) \qquad (\xi \to +\infty),$$

where

$$k_c = \frac{1}{2}(1 + (1 + 8\epsilon^2)^{\frac{1}{2}})^{\frac{1}{2}},$$

and

$$\gamma = \frac{1}{2\epsilon}(-1 + (1 + 8\epsilon^2)^{\frac{1}{2}})^{\frac{1}{2}},$$

until the origin is reached and the symmetry conditions $u_\xi = u_{\xi\xi\xi} = 0$ are imposed. In the case of equation (2.3), anti-symmetric solitary waves may be obtained used the conditions

$u = u_{\xi\xi} = 0$ instead. Using initial guesses for a_+ and ϕ_+ suggested by the expansions (2.10) or (2.14), Newton iteration is used to adjust a_+ and ϕ_+ until the two conditions at the origin are met.

The numerical solution of (2.7) is performed using a split-step Fourier spectral method; the algorithm is described in Appendix A. Figure 2–1 shows the gradual instability of an elevation wavepacket with $\epsilon = 0.1$ as it evolves towards a stable depression wavepacket. As the steepness of the wave is increased to $\epsilon = 0.3$, Figure 2–2 shows that the instability is more dramatic: a fairly steep depression wave emerges along with a dispersive wave component. To explore whether the fifth-order KdV has soliton-like solutions, the evolution of a Gaussian depression of the free surface is shown in Figure 2–3. The depression evolves to two stable depression solitary waves with different amplitudes along with very little dispersion. If a Gaussian elevation is used instead as an initial condition, the resulting evolution is much more dispersive. Qualitatively, the results resemble a radiating KdV-like wave.

2.6 Stability analysis of gravity–capillary solitary waves

The asymptotic technique used to analyze the stability of solitary waves will first be demonstrated using the fifth-order KdV equation. After a comparison of asymptotic and numerically determined growth rates, results will then be obtained for symmetric and anti-symmetric solitary-wave solutions of the modified fifth-order KdV equation and comparison with numerical results will again be made.

2.6.1 Eigenvalue problem

Assuming small perturbations to the basic state $\bar{u}$ we write

$$u(x,t) = \bar{u}(\xi) + \mathrm{Re}\, U(\xi)\, \mathrm{e}^{\lambda t} \tag{2.16}$$

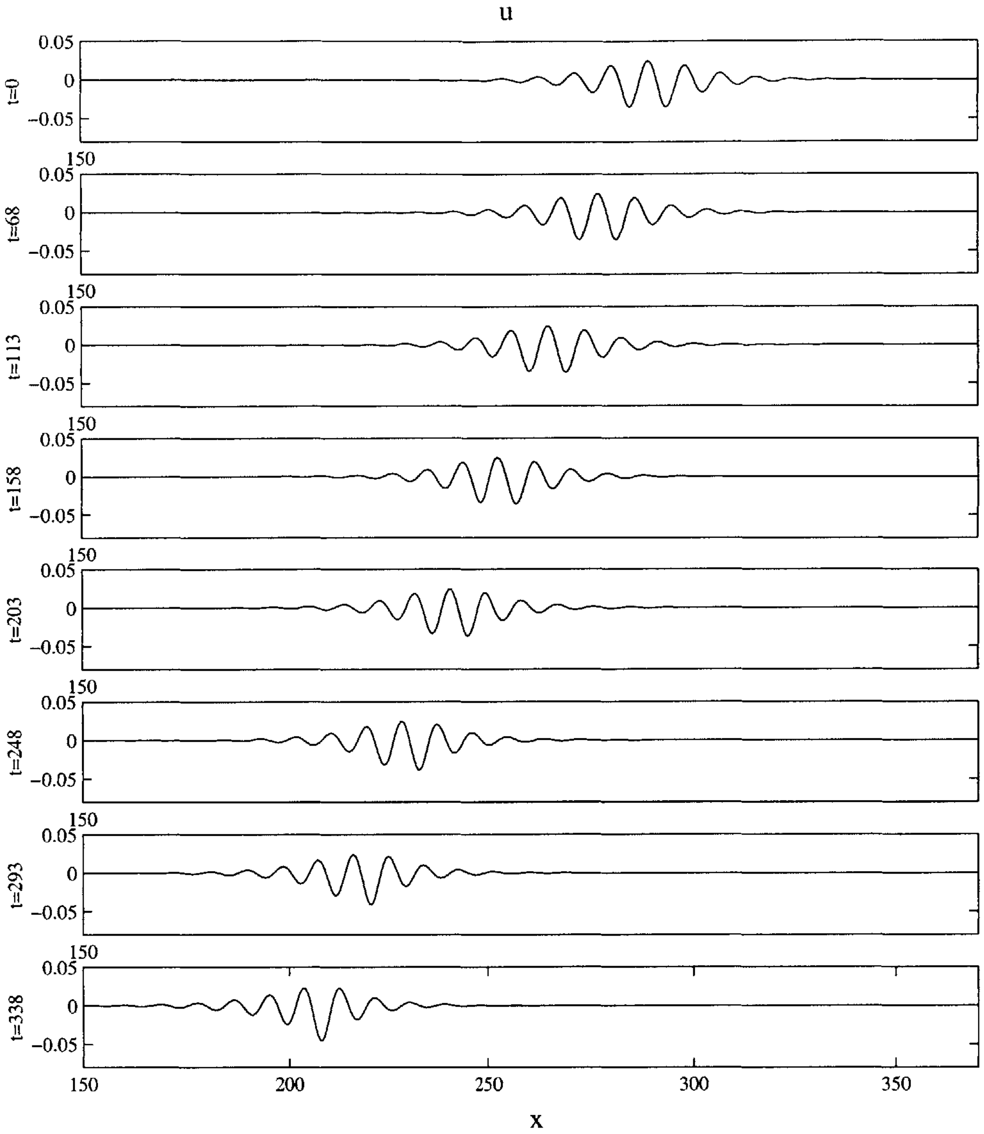

FIGURE 2-1. Numerical solution of the fifth-order KdV equation. The initial condition corresponds to an elevation solitary wave with $\epsilon = 0.1$. Because of an instability, the profile evolves to a stable depression wave.

where $\xi = x - ct$ $(c = -\frac{1}{4} - 2\epsilon^2)$. Upon substitution into (2.7) and linearization the mode shape U is found to satisfy

$$(-cU + 6\bar{u}U + U_{\xi\xi} + U_{\xi\xi\xi\xi})_\xi + \lambda U = 0. \tag{2.17}$$

To determine the boundary conditions that U must satisfy in the case of an instability, the far-field behavior can be examined by seeking linearized solutions of the form $U \sim \exp\,(\mathrm{i}\rho\xi)$

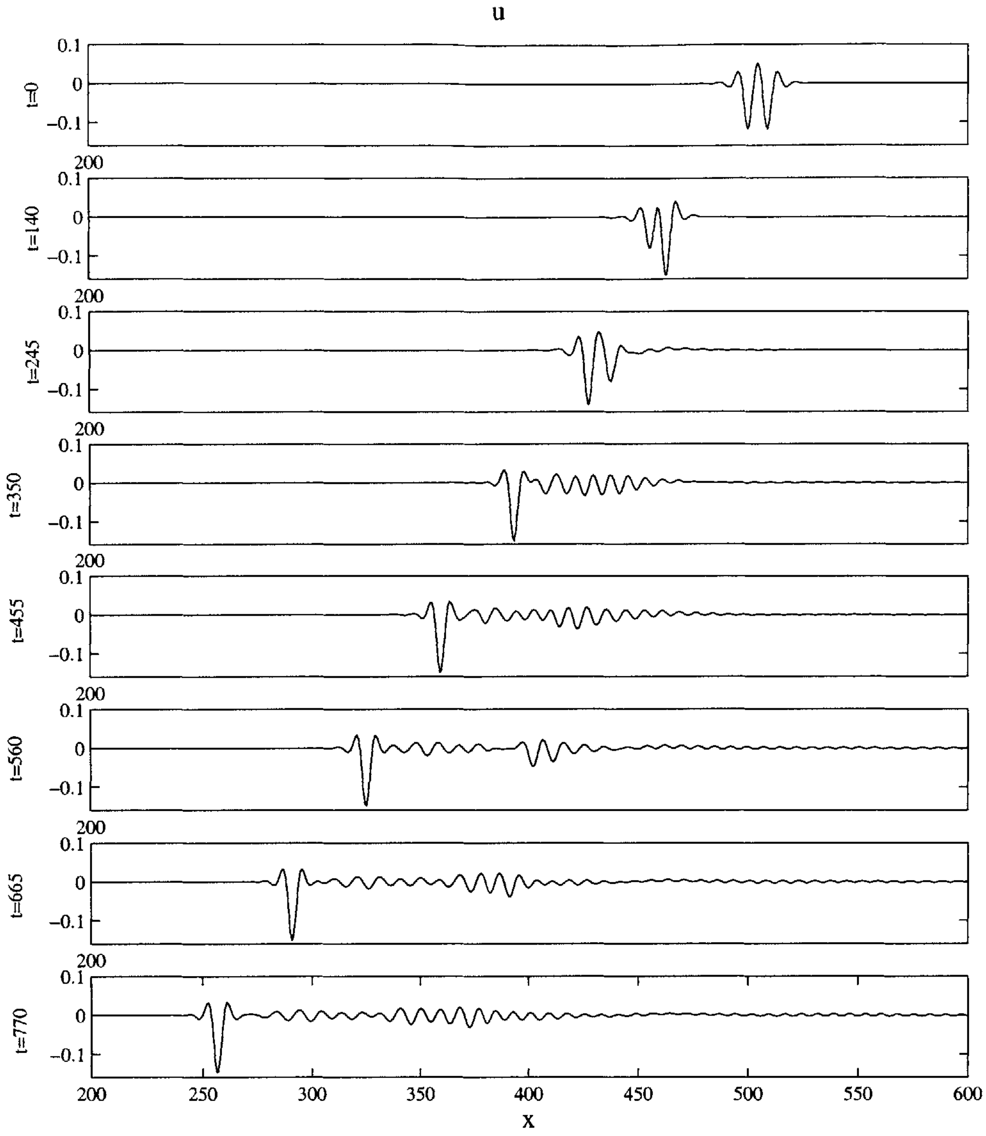

FIGURE 2–2. Same as Figure 2–1 but here $\epsilon = 0.3$ and the instability is stronger. Again, a stable depression wave emerges but with more dispersion than before.

for $|\xi| \to \infty$ thereby obtaining the characteristic polynomial

$$\rho(-c - \rho^2 + \rho^4) - \mathrm{i}\lambda = 0. \tag{2.18}$$

In the limit $\lambda \to 0$, one of the roots of (2.18) approaches zero; its value is given approximately by

$$\rho \sim 4\mathrm{i}\lambda. \tag{2.19}$$

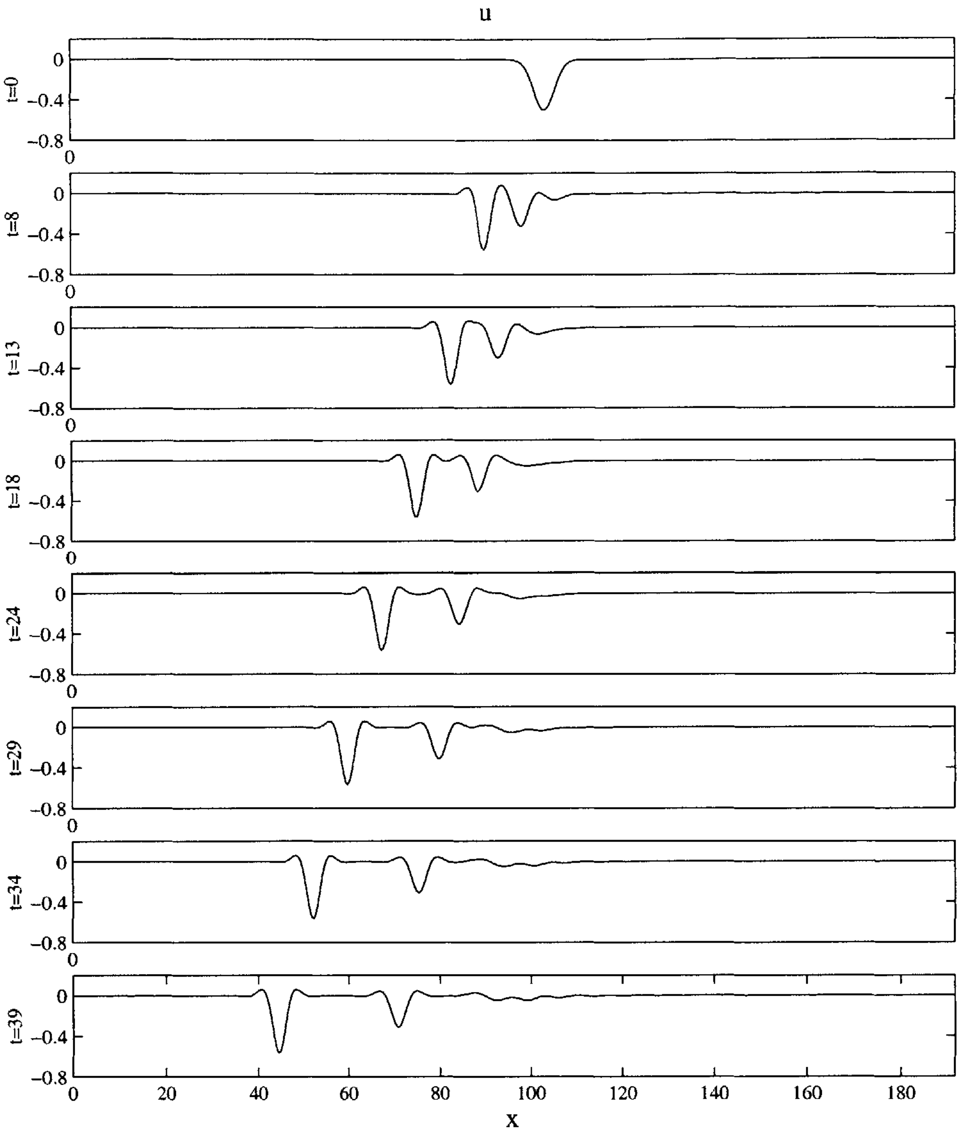

FIGURE 2–3. Numerical solution of the fifth-order KdV equation showing the emergence of depression solitons from a Gaussian depression initial condition.

The remaining roots can be found approximately by the expansion

$$\rho = \rho_0 + \lambda\rho_1 + \lambda^2\rho_2 \cdots, \tag{2.20}$$

where it is found that

$$\rho = \pm\left[\frac{1}{\sqrt{2}} + \frac{\lambda}{2\sqrt{2}\epsilon}\right] \pm \mathrm{i}\epsilon \cdots. \tag{2.21}$$

While the four roots given by (2.21) correspond to far-field solutions that can decay exponentially for $|\xi| \to \infty$, an exponential decay of the fifth far-field solution corresponding to (2.19) requires $\mathrm{Re}\,\lambda \neq 0$. Because both $U(\pm\xi)$ are solutions of (2.17) for $\pm\lambda$, $\mathrm{Re}\,\lambda \neq 0$ is a sufficient condition for instability; the unstable mode therefore satisfies

$$U \to 0 \qquad (|\xi| \to \infty). \tag{2.22}$$

Making the choice $\mathrm{Re}\,\lambda > 0$ with no loss, the upstream behavior of U can then be written approximately as

$$U \sim C_1\,\mathrm{e}^{\epsilon\xi}\cos(k_\mathrm{m}\xi + \phi_0) + C_2\,\mathrm{e}^{\epsilon\xi}\sin(k_\mathrm{m}\xi + \phi_0) \qquad (\xi \to -\infty), \tag{2.23}$$

while the downstream behavior is given by

$$U \sim C_3\,\mathrm{e}^{-\epsilon\xi}\cos(k_\mathrm{m}\xi + \phi_0) + C_4\,\mathrm{e}^{-\epsilon\xi}\sin(k_\mathrm{m}\xi + \phi_0) + C_5\,\mathrm{e}^{-4\lambda\xi} \qquad (\xi \to \infty). \tag{2.24}$$

If the solution of (2.17) is now viewed as a one-way marching problem in ξ starting far upstream with the behavior (2.23) then the problem of finding an instability is equivalent to determining a ratio C_1/C_2 and λ such that $U \to 0$ as $\xi \to \infty$ in accordance with (2.22). This idea motivates the remainder of the stability analysis.

2.6.2 Unstable modes

It is expected that if an instability exists its growth rate tends to zero as $\epsilon \to 0$; the limit in which neutrally stable periodic waves are approached. A natural starting point then is to examine the behavior of the mode shape corresponding to $\lambda = 0$ which is associated with the translational invariance of the governing equations.

Based on the asymptotic analysis of (2.1), the leading behavior of (2.10) is a modulated wavepacket with an envelope $A(X) = \frac{1}{\sqrt{38}}\,\mathrm{sech}X$ that satisfies the steady NLS equation

$$A - A_{XX} - 76|A|^2 A = 0. \tag{2.25}$$

It can be seen that (2.25) is invariant under translations of the origin of X as well as translations of the phase of the complex amplitude A. Thus, if $A(X)$ is a solution so are

$A(X+\delta)$ and $A(X)\mathrm{e}^{\mathrm{i}\delta}$. In the case that δ is infinitesimal, the disturbances to the basic state can be expressed as

$$A(X+\delta) = A(X) + \delta\, \frac{\mathrm{d}A}{\mathrm{d}X}_{\delta=0}, \tag{2.26}$$

and

$$A(X)\mathrm{e}^{\mathrm{i}\delta} = A(X) + \delta\, \mathrm{i}A(X). \tag{2.27}$$

Based on the NLS equation then, there are two independent neutral eigenfunctions A_X and $\mathrm{i}A$. The significance of these eigenfunctions in terms of the carrier oscillations can be brought out by rewriting $\bar{u} = \bar{u}(\epsilon;\xi)$ as $\bar{u} = \bar{u}(\epsilon,\xi;\phi_0,\psi_0)$

$$\begin{aligned} \bar{u} \;=\; & \sqrt{\tfrac{2}{19}}\,\epsilon\cos\theta\,\mathrm{sech}X \;+\epsilon^2\Big\{\tfrac{187}{57\sqrt{19}}\sin\theta\,\mathrm{sech}X\ \tanh X \\ & -\tfrac{4}{19}(3+\tfrac{1}{3}\cos 2\theta)\mathrm{sech}^2X\Big\} + O(\epsilon^3), \end{aligned}$$

where

$$\theta = k_\mathrm{m}\xi + \phi_0, \qquad X = \epsilon(\xi+\psi_0).$$

In terms of the shifts ϕ_0 and ψ_0, the eigenfunction $\mathrm{i}A$ corresponds then to $\bar{u}_{\phi_0}$ while A_X corresponds to $\bar{u}_{\psi_0}$ if ϕ_0 and ψ_0 are treated as the independent variables.

While the NLS theory indicates that both these modes are locally confined approximate solutions of (2.17) for $\lambda = 0$, revised perturbation theory shows that $\bar{u}_{\phi_0}$ and $\bar{u}_{\psi_0}$ are in fact not locally confined. Specifically, taking into account the shifts ϕ_0 and ψ_0 the downstream behavior of $\bar{u}$ is

$$\begin{aligned} \bar{u} \sim & -\frac{16\pi D}{\epsilon^3}\exp\left(-\frac{\pi k_\mathrm{m}}{2\epsilon}\right)\,\sin\hat{\phi}\,\mathrm{e}^X\cos\theta + \sqrt{\frac{8}{19}}\,\epsilon\,\mathrm{e}^{-X}\cos\theta \\ & +\frac{\sigma}{\epsilon^2}\exp\left(-\frac{\pi k_\mathrm{m}}{2\epsilon}\right)\,\sin\hat{\phi}\,\mathrm{e}^X\sin\theta \qquad (\xi\to\infty), \end{aligned} \tag{2.28}$$

where $\hat{\phi} = \phi_0 - k_\mathrm{m}\psi_0$. A locally confined solution is then obtainable when $\hat{\phi} = 0$ or π. Under either of these conditions, the mode $\bar{u}_{\phi_0}$ behaves as

$$\bar{u}_{\phi_0} \sim -\sqrt{\frac{8}{19}}\,\epsilon\,\mathrm{e}^{X}\sin\theta \qquad (\xi \to -\infty), \tag{2.29}$$

$$\begin{aligned}\bar{u}_{\phi_0} \quad \sim \quad & -\frac{16\pi D}{\epsilon^3}\exp\left(-\frac{\pi k_\mathrm{m}}{2\epsilon}\right)\cos(\hat{\phi}+\theta)\,\mathrm{e}^{X} - \sqrt{\frac{8}{19}}\,\epsilon\,\mathrm{e}^{-X}\sin\theta \\ & + \frac{\sigma}{\epsilon^2}\exp\left(-\frac{\pi k_\mathrm{m}}{2\epsilon}\right)\sin(\hat{\phi}+\theta)\,\mathrm{e}^{X} \qquad (\xi \to \infty),\end{aligned} \tag{2.30}$$

while $\bar{u}_{\psi_0}/\epsilon$ behaves as

$$\frac{\bar{u}_{\psi_0}}{\epsilon} \sim \sqrt{\frac{8}{19}}\,\epsilon\,\mathrm{e}^{X}\cos\theta \qquad (\xi \to -\infty), \tag{2.31}$$

$$\begin{aligned}\frac{\bar{u}_{\psi_0}}{\epsilon} \quad \sim \quad & -\frac{16\pi D}{\epsilon^4}\exp\left(-\frac{\pi k_\mathrm{m}}{2\epsilon}\right)\cos\theta\,(\epsilon\sin\hat{\phi} - k_\mathrm{m}\cos\hat{\phi})\,\mathrm{e}^{X} - \sqrt{\frac{8}{19}}\,\epsilon\,\mathrm{e}^{-X}\cos\theta \\ & + \frac{\sigma}{\epsilon^3}\exp\left(-\frac{\pi k_\mathrm{m}}{2\epsilon}\right)\sin\theta\,(\epsilon\sin\hat{\phi} - k_\mathrm{m}\cos\hat{\phi})\,\mathrm{e}^{X} \qquad (\xi \to \infty).\end{aligned} \tag{2.32}$$

It can then be seen that when $\hat{\phi} = 0$ or π, $\bar{u}_{\psi_0}$ and $\bar{u}_{\phi_0}$ are not locally confined even though $\bar{u}$ is. The linear combination

$$\frac{\mathrm{d}\bar{u}}{\mathrm{d}\xi} = k_\mathrm{m}\bar{u}_{\phi_0} + \bar{u}_{\psi_0} \qquad (\hat{\phi} = 0, \pi), \tag{2.33}$$

however, is locally confined since this is an exact eigenfunction of (2.17) when $\lambda = 0$ owing to the translational invariance of (2.1).

Returning to the general upstream solutions of (2.17) shown by (2.23), it is then apparent that $\bar{u}_{\phi_0}$ provides the main structure of U if the upstream behavior consists mostly of a growing term proportional to $\sin\theta$, while $\bar{u}_{\psi_0}$ provides the main structure of U if the upstream behavior is mostly a growing term proportional to $\cos\theta$. It is then suspected that for $\lambda \neq 0$, but small, U is possibly a linear combination of two expansions U_1 and U_2 with

$$U_1 = \frac{\bar{u}_{\psi 0}}{\epsilon} + \lambda U_1^{(1)} + \lambda^2 U_1^{(2)} \cdots , \tag{2.34}$$

$$U_2 = \bar{u}_{\phi 0} + \lambda U_2^{(1)} + \lambda^2 U_2^{(2)} \cdots , \tag{2.35}$$

so that

$$U = U_1 + C\, U_2. \tag{2.36}$$

The strategy then is to require that $U \to 0$ as $\xi \to -\infty$ and to seek values of C and λ so that $U \to 0$ as $\xi \to \infty$. One simple solution is of course $\lambda = 0$ and $C = k_{\mathrm{m}}/\epsilon$, according to (2.33). In this case, the dominant behavior upstream comes from $\bar{u}_{\phi 0}$ since $\bar{u}_{\psi 0}$ is $O(\epsilon)$ when $\bar{u}_{\phi 0}$ is $O(1)$. The approach for $\lambda \neq 0$, however, is to assume that if exponentially growing terms appear downstream in $U_1^{(1)}$, $U_1^{(2)}$, $U_2^{(1)}$ or $U_2^{(2)}$ that they are cancelled by the exponentially growing downstream tails of $\bar{u}_{\phi 0}$ and $\bar{u}_{\psi 0}/\epsilon$. As this cancellation will then require that the growing tails of the leading expressions are at most $O(\lambda)$, it is sufficient to treat the leading terms in (2.34) and (2.35) as being locally confined in the perturbation theory.

If this approach is carried out, the unknowns C and λ can be determined by setting the coefficients of the downstream growing terms proportional to cos θ and sin θ in (2.36) to zero. The resulting system of two equations can be solved for C and λ. When the growing behavior downstream is cancelled, it will be found that λ is indeed exponentially small as $\epsilon \to 0$.

To demonstrate how growing terms in U can arise in either of the expansions (2.34) or (2.35) one may write

$$U = U^{(0)} + \lambda U^{(1)} + \lambda^2 U^{(2)} \cdots \tag{2.37}$$

and assume, to be verified later, that λ is smaller than any power of ϵ.

Upon substitution into (2.17) it is found that at $O(1)$

$$(-cU^{(0)} + 6\bar{u}U^{(0)} + U^{(0)}_{\xi\xi} + U^{(0)}_{\xi\xi\xi\xi})_\xi = 0. \tag{2.38}$$

For the sake of demonstration, the locally confined part of $\bar{u}_{\phi_0}$ is selected as the approximate solution to this equation. Again, this corresponds to the neutral mode iA associated with the NLS equation.

At $O(\lambda)$ it is then found that

$$(-cU^{(1)} + 6\bar{u}U^{(1)} + U^{(1)}_{\xi\xi} + U^{(1)}_{\xi\xi\xi\xi})_\xi = -U^{(0)}. \tag{2.39}$$

The right-hand side, being odd, is orthogonal to $\bar{u}$ which is the solution of the adjoint problem. Therefore, if $U^{(1)} \to 0$ as $\xi \to -\infty$, it can be shown by integration by parts that $U^{(1)} \to 0$ as $\xi \to \infty$ provided that the orthogonality condition

$$\int_{-\infty}^{\infty} U^{(0)}\bar{u} \, \mathrm{d}\xi = 0 \tag{2.40}$$

is satisfied. This condition is automatically met.

Proceeding to $O(\lambda^2)$, it is found that

$$(-cU^{(2)} + 6\bar{u}U^{(2)} + U^{(2)}_{\xi\xi} + U^{(2)}_{\xi\xi\xi\xi})_\xi = -U^{(1)}. \tag{2.41}$$

In this case,

$$\int_{-\infty}^{\infty} U^{(1)}\bar{u} \, \mathrm{d}\xi \neq 0, \tag{2.42}$$

since $U^{(1)}$ is an odd function, and so if $U^{(2)} \to 0$ as $\xi \to -\infty$ it is expected that $U^{(2)}$ will have a growing tail as $\xi \to \infty$.

Upon substitution of (2.36) into (2.17), the forced problems for $U_1^{(1)}, U_1^{(2)}, U_2^{(1)}$, and $U_2^{(2)}$ are found to have the general form

$$(-cQ + 6\bar{u}Q + Q_{\xi\xi} + Q_{\xi\xi\xi\xi})_\xi = F, \tag{2.43}$$

which can be solved approximately by multiple scales using the expansions

$$F = \epsilon(f(X)\,\mathrm{e}^{\mathrm{i}\theta} + \mathrm{c.c.}) + \epsilon^2 f_0(X) + \epsilon^2(f_2(X)\,\mathrm{e}^{2\mathrm{i}\theta} + \mathrm{c.c.}) + \cdots, \tag{2.44}$$

$$\bar{u} = \epsilon(\bar{A}(X)\,\mathrm{e}^{\mathrm{i}\theta} + \mathrm{c.c.}) + \epsilon^2 \bar{A}_0(X) + \epsilon^2(\bar{A}_2(X)\,\mathrm{e}^{2\mathrm{i}\theta} + \mathrm{c.c.}) + \cdots, \tag{2.45}$$

$$Q = \frac{1}{\epsilon}(q(X)\,\mathrm{e}^{\mathrm{i}\theta} + \mathrm{c.c.}) + q_0(X) + (q_2(X)\,\mathrm{e}^{2\mathrm{i}\theta} + \mathrm{c.c.}) + \cdots. \tag{2.46}$$

This lengthy procedure is carried out in Appendix B; the results will only be stated here.

The first-order corrections are found to be

$$U_1^{(1)} = -\frac{1}{\sqrt{76}\,\epsilon}\,(X\ \mathrm{sech}X\ \mathrm{tanh}X - S)\cos\theta, \tag{2.47}$$

$$U_2^{(1)} = \frac{1}{\sqrt{76}\,\epsilon}\,X\ \mathrm{sech}X\ \mathrm{tanh}X\sin\theta. \tag{2.48}$$

At the next order, requiring that both $U_1^{(2)}$ and $U_2^{(2)}$ go to zero as $\xi \to -\infty$ it is subsequently found that

$$U_1^{(2)} \sim -\frac{1}{8\sqrt{38}\,\epsilon^3}\mathrm{e}^X\cos\theta \qquad (\xi \to \infty), \tag{2.49}$$

and

$$U_2^{(2)} \sim -\frac{1}{8\sqrt{38}\,\epsilon^3}\mathrm{e}^X\sin\theta \qquad (\xi \to \infty), \tag{2.50}$$

which are the exponentially growing tails as expected. It should be noted that the secular terms appearing in (2.47) and (2.48) are consistent with the $O(\lambda)$ corrections to the wavenumber of the oscillatory tails of U as shown in (2.21) and are not troublesome.

Having determined U_1 and U_2, it remains to cancel the growing downstream behavior of U in (2.36). When this is carried out, the following system of two equations is obtained

$$\lambda^2 = 128\sqrt{38}\,\pi\,D\exp\left(-\frac{\pi k_{\mathrm{m}}}{2\epsilon}\right)\cos\hat{\phi}\,(\frac{k_{\mathrm{m}}}{\epsilon} - C), \tag{2.51}$$

$$\epsilon\sigma\cos\hat{\phi} - \frac{\lambda^2}{8\sqrt{38}}\exp\left(\frac{\pi k_{\mathrm{m}}}{2\epsilon}\right) = \frac{\sigma\,k_{\mathrm{m}}}{C}\cos\hat{\phi}. \tag{2.52}$$

Eliminating λ^2 and solving the resulting quadratic for C it is found that

$$C = \frac{k_{\mathrm{m}}}{2\epsilon} \pm \frac{k_{\mathrm{m}}}{2\epsilon}\left(1 + \frac{2\sigma\epsilon^2}{k_{\mathrm{m}}} + O(\epsilon^4)\right). \tag{2.53}$$

When the negative sign in (2.53) is taken, it is found that $C = O(\epsilon)$ and

$$\lambda^2 = 128\sqrt{19}\,\pi\,D\,\frac{1}{\epsilon}\exp\left(-\frac{\pi k_{\mathrm{m}}}{2\epsilon}\right)\cos\hat{\phi} \tag{2.54}$$

to leading-order in ϵ. Noting that $D > 0$, it follows that when $\hat{\phi} = 0$ which corresponds to elevation solitary waves, λ is real and elevation waves are therefore unstable. The eigenfunction in this case is given by

$$U \sim \bar{u}_{\psi_0}/\epsilon \sim \sqrt{\frac{2}{19}}\,\epsilon\cos(k_{\mathrm{m}}\xi)\,\mathrm{sech}X\,\tanh X \qquad (\epsilon \to 0). \tag{2.55}$$

When $\hat{\phi} = \pi$, which corresponds to depression waves, the analysis yields that λ is imaginary. In this case, the last term appearing in the downstream behavior (2.24) represents a purely oscillatory term and hence the analysis is inconclusive although it suggests that depression waves might be stable which is confirmed by the numerical results to be presented.

When the positive sign is taken in (2.53), it is found that $C = k_{\mathrm{m}}/\epsilon + O(\epsilon)$ and $\lambda^2 = O[\epsilon\exp(-1/\epsilon)]$. Thus, to leading-order in ϵ, $U \sim \bar{u}_{\phi_0}$ and by comparison with (2.33) this case tends to the neutral mode when $\epsilon \to 0$. The dominant growth rate is therefore given by (2.54).

2.6.3 Modified fifth-order KdV equation

The stability analysis can also be applied to the modified fifth-order KdV equation given in time-dependent form by

$$u_t + u_{xxx} + u_{xxxxx} - 6u^2 u_x = 0, \tag{2.56}$$

which has a steady solitary wave solution $u = \bar{u}(x - ct)$ given by (2.14) that approximately satisfies (2.3).

The eigenvalue problem associated with (2.56) reads

$$(-cU - 6\bar{u}^2 U + U_{\xi\xi} + U_{\xi\xi\xi\xi})_\xi + \lambda U = 0, \tag{2.57}$$

$$U \to 0 \qquad (|\xi| \to \infty). \tag{2.58}$$

The only difference that appears in carrying out the stability analysis as before is that the general forced problem (2.43) is solved by expansions in odd harmonics. When this procedure is carried out, it is found that exponentially growing terms again appear in $U_1^{(2)}$ and $U_2^{(2)}$. By cancelling the growing behavior of U downstream it is found that the dominant growth rate is given to leading-order in ϵ by

$$\lambda^2 = 128\sqrt{3}\pi D' \frac{1}{\epsilon} \cos 2\hat{\phi} \exp(-\frac{\pi k_{\mathrm{m}}}{\epsilon}), \tag{2.59}$$

while the eigenfunction is given by

$$U \sim \bar{u}_{\psi_0}/\epsilon \sim -\sqrt{\frac{4}{6}}\, \epsilon \sin(k_{\mathrm{m}}\xi)\, \mathrm{sech} X \, \tanh X \qquad (\epsilon \to 0). \tag{2.60}$$

As $D' < 0$ in this case, λ is real when $\hat{\phi} = \pm\pi/2$ which implies that anti-symmetric solitary waves are unstable. The eigenfunction U is again given to leading-order by $\bar{u}_{\psi_0}/\epsilon$. When $\hat{\phi} = 0$ or π, λ is imaginary and therefore a localized mode shape is not obtained.

2.6.4 Comparison with numerical results

The stability calculations are first performed by discretizing either (2.17) or (2.57) using fourth-order accurate finite-difference approximations over the domain $-\xi_\infty \leq \xi \leq \xi_\infty$ and expressing the resulting system as a matrix eigenvalue problem

$$[L]\, U = \lambda\, U. \tag{2.61}$$

After a global eigensolver was used to detect the presence of unstable modes, a shooting procedure was used to refine the eigenvalue λ and the mode shape U.

The shooting procedure is to decompose U as

$$U(\xi) = C_1\, S_1(\xi) + C_2\, S_2(\xi) \qquad (-\xi_\infty \leq \xi \leq 0), \tag{2.62}$$

and

$$U(\xi) = C_3\, S_3(\xi) + C_4\, S_4(\xi) + C_5\, S_5(\xi) \qquad (0 \leq \xi \leq \xi_\infty), \tag{2.63}$$

where the far-field behavior of each S_n ($n = 1...5$) corresponds to a homogeneous solution appearing in either (2.23) or (2.24). The point of continuity is taken as $\xi = 0$ for simplicity. By imposing continuity of $U, U_\xi, U_{\xi\xi}, U_{\xi\xi\xi}, U_{\xi\xi\xi\xi}$ at $\xi = 0$ a homogeneous $5x5$ system of equations can be obtained. Solvability of this system requires that the determinant of the coefficient matrix vanishes which only occurs for special values of λ. Once a correct eigenvalue is obtained, one of the C_n may be normalized to 1 and the remaining C_n can be obtained by solving the reduced $4x4$ system of equations.

The functions S_n are obtained by solving (2.17) or (2.57) numerically using a fourth-order Runge-Kutta method starting with the independent far-field solutions (2.23) and (2.24) and integrating to $\xi = 0$. Accurate growth and oscillation rates in the far-field can be obtained by solving the characteristic polynomial (2.18) numerically. Note that in (2.62) and (2.63) it has again been assumed that $\text{Re}\lambda > 0$ with no loss.

When the numerical procedure was carried out for the fifth-order KdV problem, it was confirmed that elevation waves are linearly unstable owing to the presence of a single

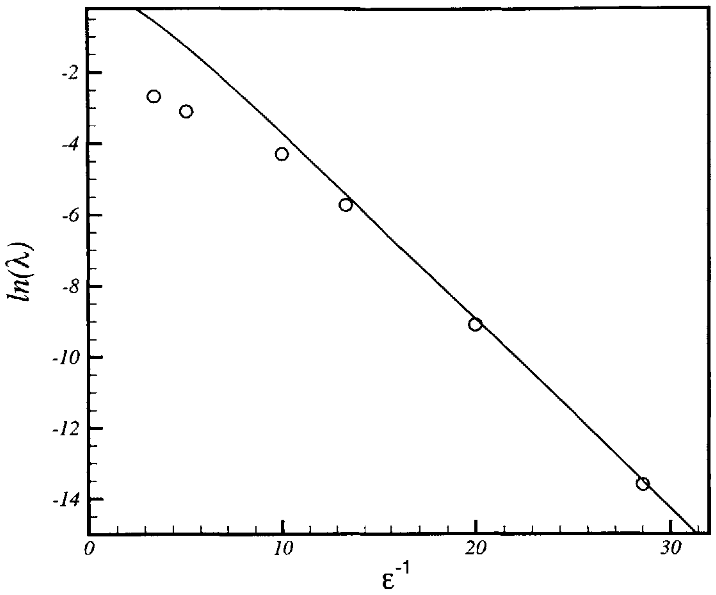

FIGURE 2–4. Comparison of the asymptotic result (2.54) (–) against numerically computed (○) instability growth rates for elevation solitary waves of the fifth-order KdV equation for various values of the wave steepness ϵ.

trapped mode with a corresponding eigenvalue that is real. The eigenvalue spectrum of depression waves on the other hand possesses no unstable modes; depression waves appear to be linearly stable. The numerical procedure was also applied to the modified fifth-order KdV problem which showed that anti-symmetric waves are indeed unstable in agreement with the analysis; the eigenvalue spectrum again possesses a single pair of real eigenvalues. No unstable modes were found in the eigenvalue spectrum of symmetric waves and so they appear to be stable.

A comparison of the numerically determined growth rates for both cases are compared with the asymptotic values given by (2.54) and (2.59) for a range of ϵ as shown in figures 2–4 and 2–5 for the quadratic and cubic fifth-order KdV equations, respectively. As can be seen, λ is exponentially small as $\epsilon \to 0$ in both cases with λ approaching zero faster in the cubic case. Overall the agreement with the analysis is excellent. In addition, the unstable eigenfunctions are in excellent agreement with the asymptotic predictions.

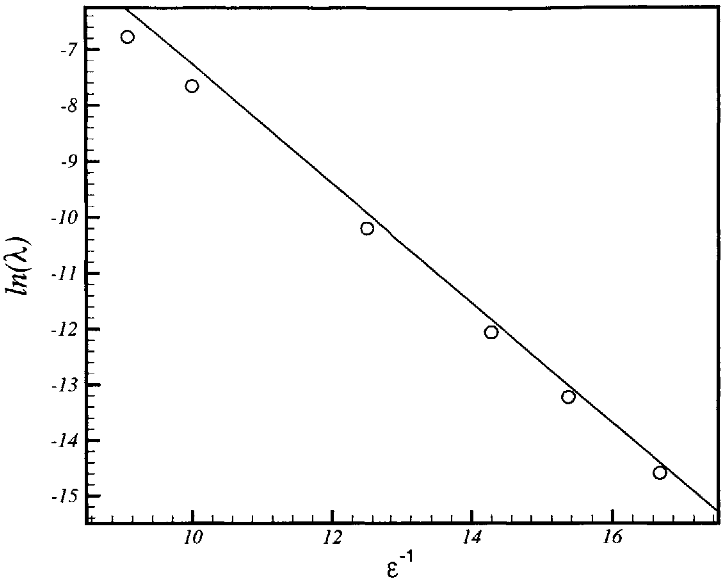

FIGURE 2–5. Comparison of the asymptotic result (2.59) (–) against numerically computed (∘) instability growth rates for elevation solitary waves of the modified fifth-order KdV equation for various values of the wave steepness ϵ.

2.7 Stability of solitary waves of the nonlinear Bernoulli–Euler beam equation

In this section, the stability theory is applied to solitary waves propagating on the Bernoulli–Euler beam supported by a nonlinear elastic foundation. The analysis of this section differs somewhat from the previous one in that a multiple scales approach is adopted from the start. As will be seen, this simplifies the analysis.

The eigenvalue problem for unstable modes in the form $W(\eta)\exp(\lambda t)$ associated with (2.8) reads

$$\lambda^2 W - 2v\lambda W_\eta + v^2 W_{\eta\eta} + W + W_{\eta\eta\eta\eta} + 6\bar{w}W = 0, \tag{2.64}$$

$$W \to 0 \qquad (|\eta| \to \infty), \tag{2.65}$$

where $\bar{w}$ is the steady state that satisfies (2.1) when the proper transformation is used. Instead of expanding W in powers of λ, a reduced form of (2.64) is obtained by expanding

W and $\bar{w}$ in harmonics

$$\bar{w} = \epsilon(\bar{A}(X)\mathrm{e}^{\mathrm{i}\theta} + \text{c.c.}) + \epsilon^2(\bar{A}_2(X)\mathrm{e}^{2\mathrm{i}\theta} + \text{c.c.} + \bar{A}_0(X)) \cdots, \tag{2.66}$$

$$W = (a(X)\mathrm{e}^{\mathrm{i}\theta} + \text{c.c.}) + \epsilon(a_2(X)\mathrm{e}^{2\mathrm{i}\theta} + \text{c.c.} + a_0(X)) \cdots \tag{2.67}$$

where $X = \sqrt{2}\epsilon\eta$, $v = \sqrt{2}(1 - 2\epsilon^2)$, and $\theta = \eta + \phi_0$ which is equivalent to a stability approach based on the NLS equation thus far. Collecting the mean, second harmonic, and fundamental terms yields

$$a_0 = -6(\bar{A}\ a^* + \bar{A}^* a) + O(\epsilon), \tag{2.68}$$

$$a_2 = -\frac{2}{3}\ \bar{A}a + O(\epsilon), \tag{2.69}$$

$$-\mathrm{i}\hat{\lambda}\ a - a_{XX} + a + \frac{3}{4}(\bar{A}^* a_2 + \bar{A}_2 a^* + \bar{A}_0 a + \bar{A}a_0) = O(\epsilon), \tag{2.70}$$

where $\hat{\lambda} = \frac{\sqrt{2}}{4}\frac{\lambda}{\epsilon^2}$. By using $\bar{A}_0 = -6|\bar{A}|^2$ and $\bar{A}_2 = -\frac{1}{3}\bar{A}^2$ it is then found that a satisfies

$$a - a_{XX} - \frac{19}{2}|\bar{A}|^2 a - \frac{19}{4}\bar{A}^2 a^* - \mathrm{i}\hat{\lambda}a = 0. \tag{2.71}$$

Upon using the leading behavior of the steady state $\bar{A} = 2\sqrt{\frac{2}{19}}\ \text{sech}X$ it is then found that a satisfies

$$a - a_{XX} - 2\ \text{sech}^2 X(a^* + 2a) - \mathrm{i}\hat{\lambda}a = 0. \tag{2.72}$$

From the analysis of Section 2.6, it is expected that by assuming $|\hat{\lambda}| \ll 1$ and expanding a in powers of $\hat{\lambda}$ that exponentially growing terms will appear downstream if $a \to 0$ as $X \to -\infty$. The strategy then is to once again cancel any growing terms arising downstream with the exponentially growing tail of the leading-order behavior.

In the present approach, however, (2.72) can be solved exactly by using the transformation

$$a = -f_{XX} + 2\ \tanh X f_X - \tanh^2 X f + \text{sech}^2 X f^*, \tag{2.73}$$

which reduces (2.72) to

$$f - f_{XX} - \mathrm{i}\hat{\lambda} f = 0 \tag{2.74}$$

and so it is not necessary to expand a from the outset. Requiring that $a \to 0$ as $X \to -\infty$ it is found that

$$a = R(-s^2 + 2\, s \tanh X - \tanh^2 X)\mathrm{e}^{sX} + P^* \mathrm{sech}^2 X \mathrm{e}^{s^* X} \tag{2.75}$$

where $s = (1 - \mathrm{i}\hat{\lambda})^{\frac{1}{2}}$ and R is a complex constant. In the limit $\hat{\lambda} \to 0$, (2.75) may be expressed as

$$a \sim \mathrm{sech}^2 X \, (-P\mathrm{e}^{-X} + P^* \mathrm{e}^{X}) + O(\hat{\lambda}). \tag{2.76}$$

It can be verified that if P is imaginary, then $a \sim \mathrm{i}\bar{A}$, while if R is real, $a \sim \bar{A}_X$. Based on the arguments presented in Section 2.6, the dominant unstable eigenfunction is obtained when R is real as this possibility corresponds to $W \sim \bar{u}_{\psi_0}/\epsilon$. The eigenfunction U may then be normalized to u_{ψ_0}/ϵ by taking $R = -\sqrt{\frac{2}{19}}\epsilon$. With this normalization it is found that

$$a \sim -\frac{1}{2\sqrt{38}}\, \epsilon \, \hat{\lambda}^2 \, \mathrm{e}^X \qquad (X \to \infty). \tag{2.77}$$

However, from Section 2.6 it is known from revised perturbation theory that $\bar{A}_X$ is not locally confined. Specifically, when $\hat{\lambda} = 0$ the refined downstream behavior of a is

$$a \sim \frac{32\pi \, D}{\sqrt{2}\epsilon^4} \exp(-\frac{\pi k_{\mathrm{m}}}{2\epsilon}) \cos\hat{\phi} \, \mathrm{e}^X \qquad (X \to \infty). \tag{2.78}$$

Cancellation of (2.77) with (2.78) then requires

$$\lambda^2 = 512\sqrt{19}\pi D \frac{1}{\epsilon} \exp(-\frac{\pi k_{\mathrm{m}}}{2\epsilon}) \cos\hat{\phi} \tag{2.79}$$

in which case elevation waves ($\hat{\phi} = 0$) are unstable.

The numerical procedure described in Section 2.6 can be easily modified for use with the beam equation. It was confirmed that elevation solitary waves are again unstable in this instance, while depression waves are stable. Figure 2–6 shows a comparison of the predicted instability growth rates given by (2.79) with the numerically computed growth rates. The agreement is again very good and the corresponding eigenfunctions are also in good agreement.

2.8 Discussion

In the actual gravity–capillary water wave problem, viscous effects cannot be entirely neglected. In fact, the dissipation rate of gravity–capillary wavepackets is $O(1)$ and overwhelms the exponentially small effects of instability. It is expected that for large-amplitude solitary waves, the growth rates increase to be on the level of dissipation rates and this will be explored further in the next chapter. The findings here are at least consistent with the observation of depression solitary waves by Zhang (1995; 1999) and Longuet-Higgins & Zhang (1997).

As described in the introduction, the localized equilibria of the buckling model (2.9) also satisfy (2.1) after rescalings. In contrast to the solitary wave examples, an instability can be readily found by straightforward expansions in the amplitude parameter. Specifically, for subcritical loads $P = 2 - 8\epsilon^2$ ($0 \le \epsilon \ll 1$) the expansion reads

$$w(x,t) = \epsilon(B(\chi,T)\mathrm{e}^{\mathrm{i}kx} + \text{c.c.}) + \epsilon^2(B_2(\chi)\mathrm{e}^{2\mathrm{i}kx} + \text{c.c.} + B_0(\chi)) \cdots \tag{2.84}$$

where $T = \epsilon t$, $\chi = \epsilon x$ and $k = 1 - \epsilon^2 + O(\epsilon^4)$. By substituting (2.84) into (2.9) it can be shown that B satisfies

$$B_{TT} + 8B - 4B_{\chi\chi} - 38|B|^2 B = O(\epsilon). \tag{2.85}$$

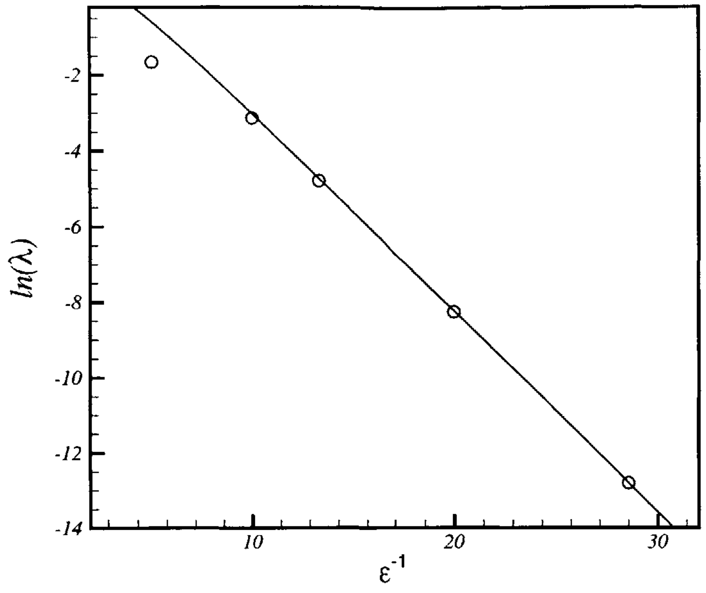

FIGURE 2–6. Comparison of the asymptotic result (2.79) (–) against numerically computed (∘) instability growth rates of elevation solitary waves of the nonlinear beam equation for various values of the wave steepness ϵ.

By setting B_{TT} to zero, the leading behavior of the localized equilibrium reads $\bar{B}$

$$\bar{B} = \frac{4}{\sqrt{38}} \operatorname{sech}\sqrt{2}\chi. \tag{2.86}$$

The stability of this solution to small disturbances can determined by writing $B(\chi, T) = \bar{B}(\chi) + (h(\chi) + ig(\chi))\exp(\sigma T)$ where h and g are real functions. Upon substitution into (2.85) it is found that the eigenvalue problems for h and g read

$$h_{\chi\chi} + (12 \operatorname{sech}^2\sqrt{2}\chi - 2 - \sigma^2/4)h = 0, \tag{2.87}$$

$$g_{\chi\chi} + (4 \operatorname{sech}^2\sqrt{2}\chi - 2 - \sigma^2/4)g = 0, \tag{2.88}$$

to leading order in ϵ, and both h and $g \to 0$ as $\chi| \to \infty$. Exploiting the transformation $Z = \tanh\chi$ reduces (2.87) and (2.88) to Legendre form after which it is straightforward to show that there is an unstable eigenfunction $h \propto \operatorname{sech}^2\sqrt{2}\chi$ with a growth-rate $\lambda = 2\sqrt{6}$. The unscaled growth-rate is therefore $2\sqrt{6}\epsilon$ which is algebraically small in the amplitude parameter in contrast to the solitary wave examples. Although revised perturbation theory shows that only elevational or depressional equilibria are possible, this clearly has no bearing on the stability in this case.

In the solitary wave examples discussed involving systems with quadratic nonlinearity, it was always the case that elevation waves were unstable. If the signs of the nonlinear terms are reversed though, it can immediately be concluded that depression waves would instead be unstable. In the solid mechanics problem, this would simply amount to using a quadratic-softening nonlinear foundation. Although in the surface wave problem there is no way of changing the sign of the nonlinear term in the fifth-order KdV equation by varying physical parameters, it is possible in a two-fluid system to make this change by varying the density and depth ratios (see Laget & Dias 1997). Hence, in the interfacial-wave problem, the stability of elevation waves is likely to depend on system parameters. This hypothesis will be explored further in Chapter 4.

CHAPTER 3

STABILITY OF STEEP GRAVITY-CAPILLARY SOLITARY WAVES IN DEEP WATER

3.1 Introduction

Thus far, the analysis of gravity–capillary solitary waves has only considered the small-amplitude limit in which the wave profiles resemble modulated wavepackets. In field experiments, however, observations of gravity–capillary solitary waves have reported profiles that resemble steep depressions in the free surface with maximum surface steepnesses approaching 50 degrees (Zhang 1995, Zhang 1999). While forcing by wind was involved in the original observations, Longuet-Higgins & Zhang (1997) were able to excite such depression solitary waves on deep water more directly in the laboratory by applying a localized pressure distribution to a stream moving below the minimum phase speed of infinitesimal gravity–capillary waves; once excitation was removed, a free depression wave propagated with speed and profile consistent with theory taking into account viscous dissipation. In light of these experiments, it appears that an analysis of solitary wave dynamics would be incomplete without considering the large-amplitude limit which is examined in this chapter.

Experimental studies have so far only reported solitary waves with single-depression profiles on deep water. Potential-flow theory, on the other hand, suggests a wide variety of other possible solitary-wave solutions. Specifically, the computations of Vanden-Broeck & Dias (1992), apart from depression waves, revealed an elevation-wave solution branch as well. This branch was later studied in detail by Dias, Menasce & Vanden-Broeck (1996) who discovered solitary waves consisting of a series of depression waves by numerically tracing the elevation branch past successive limit points. Representative depression and elevation wave profiles for certain values of the speed parameter $\alpha = gT/\rho c^4$ are displayed in Figure 3–1; here, as in Vanden-Broeck & Dias (1992), dimensionless variables are used throughout

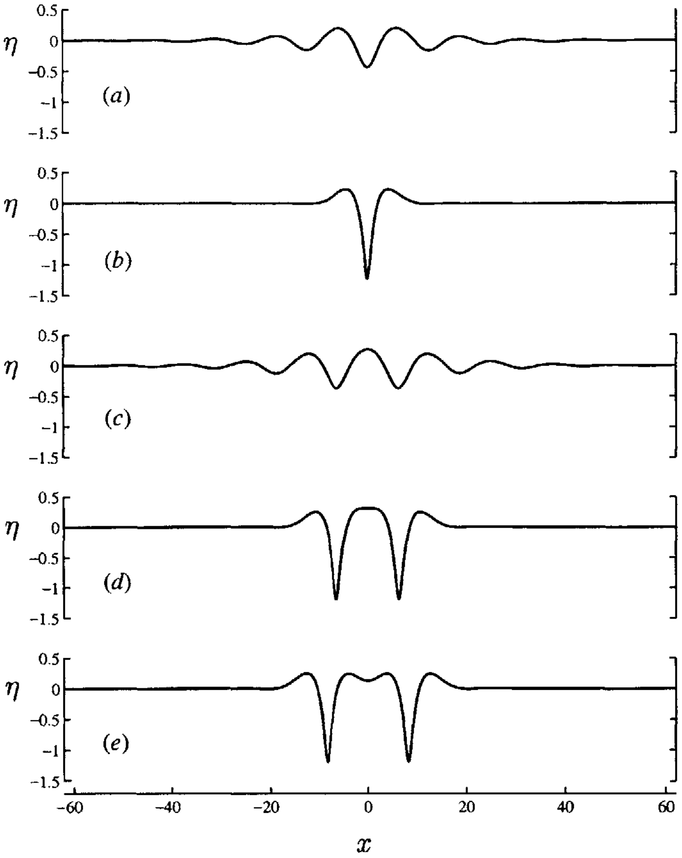

FIGURE 3–1. Representative free-surface profiles of gravity–capillary solitary waves in deep water. Depression waves are shown in (a) and (b) with speed parameters $\alpha = 0.257$ and $\alpha = 0.4$, respectively; elevation waves are shown in (c), (d) and (e) for $\alpha = 0.257$, $\alpha = 0.38$ (upper branch) and $\alpha = 0.38$ (lower branch), respectively.

with $T/\rho c^2$ as unit length and the wave speed c as unit speed, T being the coefficient of surface tension, ρ the fluid density and g the gravitational acceleration. The elevation and depression solution branches are shown in Figure 3–2 along with the locations on these branches of the particular profiles displayed in Figure 3–1. All solutions have $\alpha > \frac{1}{4}$, implying that wave speeds are less than the minimum phase speed $c_{\min} = (4gT/\rho)^{\frac{1}{4}}$ of infinitesimal gravity–capillary waves. As the solitary-wave speed approaches $c_{\min}$ (see Figures 3–1(a) and 3–1(c)) the small-amplitude limit is obtained, and these wavepacket solutions bifurcate from infinitesimal periodic waves at $\alpha = \frac{1}{4}$ (see Figure 3–2).

The stability results obtained in Chapter 2 are interesting from a theoretical viewpoint

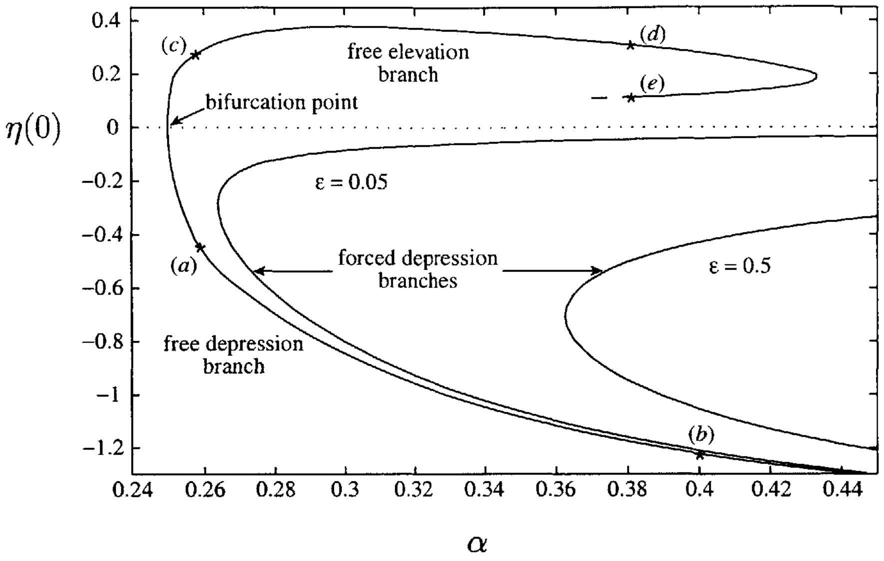

FIGURE 3–2. Solution diagrams for free and forced deep-water gravity–capillary solitary waves. The free-surface amplitude $\eta(0)$ is plotted against the wave speed parameter $\alpha = gT/\rho c^4$. The dimensionless amplitude of the pressure distribution is $\epsilon = p_{\max}/\rho c^2$, $p_{\max}$ being the pressure peak amplitude.

but their relevance can be questioned on physical grounds, given the rather limited validity of the fifth-order KdV equation—for the Bond number to be close to $\frac{1}{3}$, the water depth is restricted to a few mm so neglecting viscous dissipation cannot be justified (Zufiria 1987). Accordingly, in the present work, having in mind the relatively steep gravity–capillary solitary waves observed experimentally, we shall work with the full deep-water wave equations using numerical techniques. Moreover, while our stability analysis will be based on potential-flow theory, we shall assess the effects of viscosity following the approach proposed by Longuet-Higgins (1997).

The same numerical procedure also proves useful in the stability analysis of forced gravity–capillary solitary waves generated by a localized pressure distribution on the free surface of a stream with speed less than $c_{\min}$; this case corresponds directly to the experimental set-up of Longuet-Higgins & Zhang (1997). Steady inviscid solutions to this problem have already been computed by Vanden-Broeck & Dias (1992) who found, in addition to Rayleigh's linearized solution, a finite-amplitude branch of solutions connected to

Rayleigh's solution branch by a limit point; the geometry of these forced solution branches is shown in Figure 3–2 for blowing on the free surface with two different peak pressure amplitudes. Our numerical stability results for the forced problem are supported by an asymptotic analysis in the weakly nonlinear regime when the pressure amplitude is small and the current speed is close to $c_{\min}$. Finally, based on our findings, we shall comment on the observations of forced dynamics reported in the experiments of Longuet-Higgins & Zhang (1997).

3.2 Formulation

It is convenient to present the formulation in the context of the forced problem where a stationary localized pressure distribution is applied on the free surface of a fluid stream; the case of a free solitary wave then follows by simply setting the pressure amplitude equal to zero. For computing nonlinear steady solutions to the governing equations, we shall use the boundary-integral-equation method described in Vanden-Broeck & Dias (1992). The stability of these solutions then is tackled following a procedure similar to that devised by Tanaka (1986) for studying the stability of steep gravity solitary waves of the KdV type on water of finite depth, the essential difference being that here the additional effects of surface tension and forcing are included.

3.2.1 Governing equations and steady solutions

In the frame of the pressure distribution, the flow at large depth is a uniform stream moving to the right at constant speed $c < c_{\min}$. The y-axis points upward, $y = 0$ corresponding to the undisturbed level of the free surface. The pressure distribution is taken to be symmetric about $x = 0$, x being the streamwise coordinate. The flow, which is assumed to be incompressible and irrotational, is described by the velocity potential ϕ, and the free-surface elevation is denoted by η.

The governing equations in dimensionless form read

$$\phi_{xx} + \phi_{yy} = 0 \qquad (-\infty < x < \infty,\ -\infty < y < \eta) \tag{3.1}$$

$$\phi_t + \tfrac{1}{2}(\phi_x^2 + \phi_y^2) + \alpha\eta - \frac{\eta_{xx}}{(1+\eta_x^2)^{\frac{3}{2}}} + \epsilon p(x) = \tfrac{1}{2} \qquad (y = \eta) \tag{3.2}$$

$$\eta_t + \phi_x \eta_x = \phi_y \qquad (y = \eta) \tag{3.3}$$

$$(\phi_x, \phi_y) \to (1, 0) \qquad (\sqrt{x^2 + y^2} \to \infty), \tag{3.4}$$

where $p(x)$ represents the externally applied pressure. Two dimensionless parameters arise: the speed parameter $\alpha = gT/\rho c^4$, introduced earlier, and $\epsilon = p_{\max}/\rho c^2$ which controls the amplitude of the applied pressure, $p_{\max}$ being the pressure peak amplitude.

For obtaining nonlinear steady solutions of (3.1)–(3.4), it is convenient to use the velocity potential ϕ and stream function ψ, rather than x and y, as independent variables. Specifically, $\psi = 0$ is chosen to define the free-surface streamline and $\phi = 0$ to define the line of symmetry; the fluid region then lies in $\psi < 0$. Moreover, the horizontal (u) and vertical (v) velocity components may be expressed in terms of $f = \phi + \mathrm{i}\psi$ and $z = x + \mathrm{i}y$ by using the fact that

$$u - \mathrm{i}v = \left(\frac{\mathrm{d}z}{\mathrm{d}f}\right)^{-1} = \frac{1}{x_\phi + \mathrm{i}y_\phi}. \tag{3.5}$$

The method of solution then is to seek $x_\phi + \mathrm{i}y_\phi$ as an analytic function of f in $\psi \leq 0$.

To this end, applying Cauchy's integral theorem to $x_\phi + \mathrm{i}y_\phi - 1$ using a path including $\psi = 0$ and a large semicircle that encloses the fluid region, the integrand along the semicircle vanishes on account of (3.4). Setting $\psi = 0$ and taking the real part of the resulting expression then yields the following relation between x_ϕ and $\eta_\phi = y_\phi$:

$$x_\phi = 1 - \frac{1}{\pi}\int_{-\infty}^{\infty} \frac{\eta_\xi}{\xi - \phi}\mathrm{d}\xi \qquad (\psi = 0), \tag{3.6}$$

the integral being of Cauchy's principal-value form. Furthermore, by considering only symmetric waves and working in the half-domain ($0 \leq \phi < \infty$), (3.6) reduces to

$$x_\phi = 1 - \frac{1}{\pi}\int_{0}^{\infty} \eta_\xi \left(\frac{1}{\xi - \phi} + \frac{1}{\xi + \phi}\right)\mathrm{d}\xi \qquad (\psi = 0). \tag{3.7}$$

The kinematic boundary condition (3.3) is automatically satisfied by the choice of independent variables and, making use of (3.5), the steady version of the dynamic boundary condition (3.2) transforms to

$$\frac{1}{2(x_\phi^2 + \eta_\phi^2)} + \alpha\eta + \frac{\eta_\phi x_{\phi\phi} - x_\phi \eta_{\phi\phi}}{(x_\phi^2 + \eta_\phi^2)^{\frac{3}{2}}} + \epsilon p(\phi) = \tfrac{1}{2} \qquad (\psi = 0); \tag{3.8}$$

the pressure distribution is now a function of the velocity potential on the free-surface and is taken in the form

$$p(\phi) = \begin{cases} \exp\left(\dfrac{1}{\phi^2 - 1}\right) & (|\phi| \leq 1) \\ 0 & (|\phi| > 1) \end{cases},$$

as in Vanden-Broeck & Dias (1992).

Equations (3.7) and (3.8) define an integro-differential system for η_ϕ and x_ϕ on the free-surface. Solving this system, the free-surface profile $\eta(x)$ can be readily determined.

3.2.2 Linear stability

We denote the steady free-surface elevation, velocity potential and stream function by $H(x)$, $\Phi(x,y)$ and $\Psi(x,y)$, respectively, and consider small disturbances to these quantities:

$$\eta(x,t) = H(x) + \tilde{\eta}(x,t), \tag{3.9}$$

$$\phi(x,y,t) = \Phi(x,y) + \tilde{\phi}(x,y,t), \tag{3.10}$$

$$\psi(x,y,t) = \Psi(x,y) + \tilde{\psi}(x,y,t), \tag{3.11}$$

with $\tilde{\phi}_x = \tilde{\psi}_y$ and $\tilde{\phi}_y = -\tilde{\psi}_x$ so as to satisfy Laplace's equation.

In preparation for the ensuing linear stability analysis, both the dynamic condition (3.2) and kinematic condition (3.3), that apply along the free-surface streamline $y = H + \tilde{\eta}$, must be expanded about $y = H$ and then linearized. Carrying this out, the linearized dynamic boundary condition is

$$\begin{aligned}\tilde{\phi}_t + \Phi_x\tilde{\phi}_x + \Phi_y\tilde{\phi}_y + (\Phi_x\Phi_{xy} + \Phi_y\Phi_{yy})\tilde{\eta} + \alpha\tilde{\eta} + \epsilon p_{\Phi}\Phi_y\tilde{\eta} - \frac{\tilde{\eta}_{xx}}{(1+H_x^2)^{\frac{3}{2}}}& \\ + \frac{3H_{xx}H_x}{(1+H_x^2)^{\frac{5}{2}}}\tilde{\eta}_x = 0 \qquad (y = H),&\end{aligned} \tag{3.12}$$

and the linearized kinematic boundary condition is

$$\tilde{\eta}_t + \Phi_x\tilde{\eta}_x + H_x\tilde{\phi}_x + \Phi_{xy}\tilde{\eta} = \tilde{\phi}_y + \Phi_{yy}\tilde{\eta} \qquad (y = H). \tag{3.13}$$

It is convenient to use the arclength s of the undisturbed streamline as an independent variable, $s = 0$ being the point of symmetry, and to represent the steady state in terms of the magnitude of the velocity on the free-surface, $q = (\Phi_x^2 + \Phi_y^2)^{\frac{1}{2}}$, and the angle the velocity vector makes with the horizontal, $\theta = \arctan\,(\mathrm{d}H/\mathrm{d}x)$. Assuming normal-mode perturbations $\propto \exp(\lambda t)$ and making use of $\Phi_x = q \cos\theta$, $\mathrm{d}x = \mathrm{d}s \cos\theta$, (3.12) then transforms to

$$\lambda\tilde{\phi} = -q\frac{\mathrm{d}\tilde{\phi}}{\mathrm{d}s} - \left(q\frac{\mathrm{d}(q\sin\theta)}{\mathrm{d}s} + \alpha\right)\tilde{\eta} + \frac{1}{\cos\theta}\frac{\mathrm{d}}{\mathrm{d}s}\left(\cos^2\theta\frac{\mathrm{d}\tilde{\eta}}{\mathrm{d}s}\right) + \epsilon\frac{\mathrm{d}p}{\mathrm{d}s}\sin\theta\,\tilde{\eta}. \tag{3.14}$$

By similar manipulations, (3.13) becomes

$$\lambda\tilde{\eta} = -q\frac{\mathrm{d}\tilde{\eta}}{\mathrm{d}s} - \frac{1}{\cos\theta}\frac{\mathrm{d}\tilde{\psi}}{\mathrm{d}s} - \frac{1}{\cos\theta}\,\frac{\mathrm{d}(q\cos\theta)}{\mathrm{d}s}\,\tilde{\eta}. \tag{3.15}$$

Clearly, solutions of the linearized system (3.14) and (3.15) that are bounded and oscillatory as $|\Phi| \to \infty$ $(\Psi = 0)$ correspond to linear waves superposed on a uniform stream at infinity and have neutral stability. If unstable modes exist, therefore, they must decay to zero at infinity. Using this condition, Cauchy's theorem can again be applied to the function $\tilde{\phi} + \mathrm{i}\tilde{\psi}$ using the same semicircular contour as before in the (Φ, Ψ) plane. After taking the imaginary part of the resulting expression, we find that $\tilde{\phi}$ and $\tilde{\psi}$ form a Hilbert-transform pair:

$$\tilde{\psi} = \frac{1}{\pi}\int_{-\infty}^{\infty}\frac{\tilde{\phi}(s)}{s-\Phi}\mathrm{d}s = \mathcal{H}(\tilde{\phi}) \qquad (\Psi = 0). \tag{3.16}$$

Making the change $\mathrm{d}\;/\mathrm{d}s = q\,\mathrm{d}\;/\mathrm{d}\Phi$, the eigenvalue problem (3.14) and (3.15) then takes the final form

$$\lambda\tilde{\eta} = -q^2\frac{\mathrm{d}\tilde{\eta}}{\mathrm{d}\Phi} - q\frac{\mathrm{d}\mathcal{H}(\tilde{\phi})}{\mathrm{d}\Phi} - q\,\tilde{\eta}\,\frac{\mathrm{d}(q\cos\theta)}{\mathrm{d}\Phi} \tag{3.17}$$

$$\lambda\tilde{\phi} = -q^2\,\frac{\mathrm{d}\tilde{\phi}}{\mathrm{d}\Phi} - \left(q^2\,\frac{\mathrm{d}(q\sin\theta)}{\mathrm{d}\Phi} + 1\right)\tilde{\eta} - \frac{q}{\cos\theta}\frac{\mathrm{d}}{\mathrm{d}\Phi}\left(q\cos^2\theta\frac{\mathrm{d}\tilde{\eta}}{\mathrm{d}\Phi}\right) + \epsilon\,q\,\frac{\mathrm{d}p}{\mathrm{d}\Phi}\sin\theta\,\tilde{\eta}, \tag{3.18}$$

where both $\tilde{\eta}$ and $\tilde{\phi}$ decay to zero as $|\Phi| \to \infty$. Apart from a difference in normalization scales, this eigenvalue problem agrees with the deep-water limit of the problem solved by Tanaka (1986) if the effects of forcing and surface tension, which contribute the last two terms in (3.18), are neglected. It is noted that if $\theta \to \frac{1}{2}\pi$, a case that can occur for steep depression waves when the wave speed is low enough, the coefficient of the surface-tension term in (3.18) becomes singular, and a modified stability analysis is necessary to treat this case. We shall only consider the stability of solitary waves with single-valued surface profiles.

3.3 Numerical results

3.3.1 Numerical method

The numerical procedure for computing nonlinear steady wave disturbances is along the same lines as that presented in Vanden-Broeck & Dias (1992) and Dias *et al.* (1996): x_Φ and η_Φ and thereby $\eta(x)$ are determined using finite-difference approximations of equations (3.7) and (3.8). Truncating the domain at a sufficiently large value $\Phi = \Phi_{\mathbf{max}}$, N uniformly spaced mesh points $\Phi_i = (i-1)\Delta\Phi \;\; i = 1, ..., N$ are introduced and the boundary conditions $\eta_\Phi(0) = \eta_\Phi(\Phi_{\mathbf{max}}) = 0$ are imposed. To reduce the size of matrices that arise in the stability problem, it is advantageous to use high-order centered finite-difference approximations to represent the spatial derivatives. To handle the boundaries, intermediate centered–one-sided difference approximations were used (Fornberg 1995, Appendix C). The principal-value integral was computed using a nine-point Legendre scheme to interpolate the integrand at the mid-points. The integral was then computed just as an ordinary integral using the trapezoidal rule (Vanden-Broeck & Dias 1992, Tanaka 1986).

Starting with an initial guess for η_Φ (which in the small-amplitude limit can be found in Dias *et al.* 1996), the iteration procedure is as follows. First, equation (3.7) directly yields a compatible x_Φ after integration, both x_Φ and η_Φ are then differentiated to evaluate (3.8). The $N-2$ unknowns η_Φ are then updated by Newton iteration until (3.8) is satisfied at the $N-2$ interior points. Typically, the free-surface amplitude $\eta(0)$ was well converged when $\Delta\Phi = 0.1$, though more resolution was needed near limit points. Generation of solution curves, such as those shown in Figure 3–2, can be made by slowly varying α (or ϵ in the case of forced waves). While limit points can be traversed by well known continuation methods, often a jump to a new solution branch can be made by chance in the vicinity of the limit point if, say, the increment in α is large.

In the case of depression waves, which can have high curvature in the trough regions, a non-uniform grid was introduced, in terms of a new independent variable γ, via the transformation $\Phi = \beta\gamma + \gamma^m$, where β is a small positive number and m is an odd integer. This transformation is identical to that used by Tanaka (1986) for handling steep solitary gravity waves which have high curvature in the crest regions. In the problem of interest here, when β is small, the transformation stretches out the steep trough region and brings the tails closer to the origin; this proves especially useful for treating solitary waves in deep water which feature algebraically decaying tails (Akylas, Dias & Grimshaw 1998). The values $m = 3$ and $\beta = 0.1$ were found to be sufficient for most computations.

The discretization of the eigenvalue problem (3.17) and (3.18) was carried out in a manner similar to that followed in the steady nonlinear problem, resulting in a standard matrix eigenvalue problem of the form $[C]\mathbf{x} = \lambda\mathbf{x}$. For ease with matrix manipulation and sparse matrix storage, all stability calculations were performed using MATLAB v5.3. The d/ds and $\mathcal{H}$ operators were first represented in matrix form. Next, the matrix $[C]$ was assembled taking $\mathbf{x} = \{\tilde{\eta}\ \tilde{\phi}\}^t$. The eigenvalues in fact appear in quartets $[\lambda, -\lambda, \lambda^*, -\lambda^*]$ owing to certain symmetries of the eigenvalue problem; these symmetries can be used to reduce the dimension of the eigenvalue problem, treating λ^2 as the eigenvalue parameter, but, as it turned out, at a great increase in the required resolution, so the eigenvalue problem for λ was solved instead.

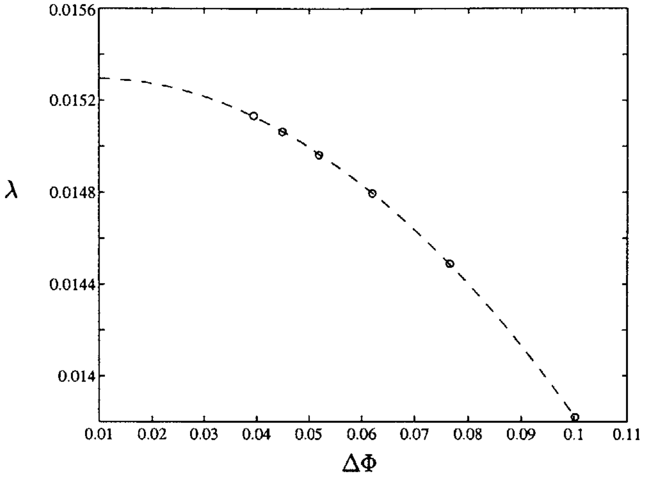

FIGURE 3–3. Eigenvalue convergence as the grid size is decreased for an elevation-wave instability ($\alpha = 0.30$)

The procedure for solving the eigenvalue problem was to first use a moderately fine grid and the QR algorithm to detect possible candidates for eigenvalues; the grid was then refined and the inverse-power method with shifting was used to obtain fully converged eigenvalues (see Appendix C). The spectrum, which obeyed the symmetries mentioned above, contains an array of imaginary eigenvalues which approximate the continuous spectrum of the actual problem. When an instability was present, in addition to these neutral eigenvalues, a pair of real eigenvalues was found with eigenvectors decaying to zero at the tails of the solitary wave, as required for eigenfunctions corresponding to unstable modes of the original continuous problem.

A typical case of convergence of the eigenvalue computations for free solitary waves as the grid size $\Delta\Phi$ was decreased, is illustrated in Figure 3–3 for an elevation solitary wave with $\alpha = 0.3$. Generally, the eigenvalue computations in the forced problem converged much faster than those for free solitary waves, and more resolution was needed in both cases as the wave steepness was increased. Details on code performance and compilers can be found in Appendix D.

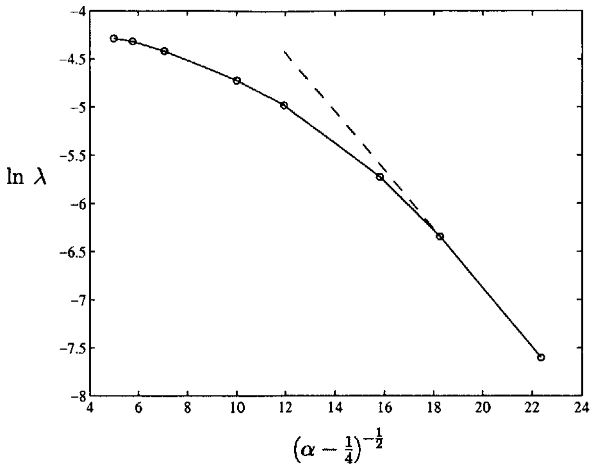

FIGURE 3–4. **Instability growth rates of small-amplitude elevation solitary waves in deep water as the bifurcation point $\alpha = \frac{1}{4}$ is approached.**

3.3.2 Free solitary waves

Based on the fifth-order KdV equation, in the small-amplitude limit, elevation solitary waves are unstable with exponentially small growth rates, but depression waves are stable (Calvo *et al.* 2000). We begin by presenting numerical evidence that small-amplitude solitary waves in deep water behave similarly.

In Figure 3–4, the instability growth rate of elevation waves is plotted on a logarithmic scale against the inverse of the parameter $(\alpha - \frac{1}{4})^{\frac{1}{2}}$. The growth rates begin to fall on a straight line as the bifurcation point is approached ($\alpha \to \frac{1}{4}$), consistent with the behavior found using the fifth-order KdV equation. Since the wave profile spreads out into a wavepacket in this limit, however, it is computationally difficult to extend the numerical results further. Nevertheless, employing this interpretation in terms of a wavepacket it was confirmed that the computed instability mode shape agrees approximately with the derivative of the solitary-wave profile with respect to the envelope variable, as predicted by the asymptotic theory for the fifth-order KdV equation (Calvo *et al.* 2000). No unstable modes were found for small-amplitude depression waves, in agreement with the fifth-order KdV theory as well.

α	$\eta(0)$	$\theta_{\max}$ (deg.)	λ	α	$\eta(0)$	$\theta_{\max}$ (deg.)	λ
0.253	0.2077	7.03	0.0016	0.30	0.3782	24.1	0.0153
0.254	0.2275	7.91	0.0033	0.32	0.3729	28.7	0.0148
0.257	0.2669	9.90	0.0069	0.34	0.3576	32.8	0.014
0.26	0.2924	11.4	0.0089	0.36	0.3477	36.5	0.012
0.27	0.3411	15.4	0.012	0.38	0.3106	39.8	0.0098
0.28	0.3647	18.6	0.014	0.40	0.2802	42.9	0.0077
0.29	0.3761	21.5	0.0145				

TABLE 3–1. Instability growth rate λ of free elevation solitary waves for various values of the speed parameter α. The free-surface elevation at the point of symmetry $\eta(0)$ and the maximum surface steepness $\theta_{\max}$ are listed for reference.

As the elevation-wave steepness increases, the instability growth rate increases as well, attaining a maximum when $\alpha = 0.30$, as shown in Table 3–1. Beyond this value of α, the growth rate decreases as the limit point at $\alpha = 0.43$ is approached. Near the limit point, instability could be detected but convergence deteriorated so results are presented only up to $\alpha = 0.40$. After the limit point is passed, profiles resembling steep overlapping depression waves are obtained, an example of which is shown in Figure 3–1(*e*). For $\alpha = 0.38$, no instability could be found for this solution type, suggesting that an exchange of stability occurs near the limit point. For the depression solution branch, instabilities could not be found for either small-amplitude or steep solitary waves.

3.3.3 Forced depression solitary waves

Having in mind the experiments of Longuet-Higgins & Zhang (1997), attention was focussed on forced depression solitary waves. We consider both weak ($\epsilon = 0.05$) and strong ($\epsilon = 0.5$) forcing amplitudes corresponding to the response curves shown in Figure 3–2. Starting on the lower-amplitude branch (corresponding to Rayleigh's solution) of each of these curves far from the limit point, no instability can be detected. As the limit point is approached, however, instability sets in as a pair of real eigenvalues, and the onset of this instability occurs closer to the nose of the response curve as the pressure amplitude

$\epsilon = 0.05$					$\epsilon = 0.5$				
α	Speed (cm/s)	$\eta(0)$	$\theta_{\max}$ (deg.)	λ	α	Speed (cm/s)	$\eta(0)$	$\theta_{\max}$ (deg.)	λ
0.279	22.5	-0.612	16.1	0.014	0.368	21.0	-0.840	25.1	0.059
0.320	21.8	-0.928	27.1	0.021	0.447	20.0	-1.203	43.3	0.100
0.368	21.0	-1.127	36.3	0.027	0.549	19.0	-1.343	56.4	0.122
0.447	20.0	-1.296	47.9	0.033	0.681	18.0	-1.395	68.2	0.133
0.549	19.0	-1.386	59.1	0.039					
0.681	18.0	-1.416	69.8	0.041					

TABLE 3–2. **Instability growth rates λ for forced depression solitary waves located on the higher-amplitude branches of the response curves in Figure 3–2. The free-surface elevation at the point of symmetry $\eta(0)$ and the maximum surface steepness $\theta_{\max}$ are listed for reference.**

is decreased. As the limit point is passed and transition is made to the higher-amplitude branch, the growth rate increases monotonically with α (see Table 3–2).

The instability found here is in dramatic contrast with the results for free depression waves discussed earlier: when the surface steepness is large and ϵ is small, in particular, the forced response is essentially a free depression solitary wave profile that is lightly forced; nevertheless, this small amount of forcing is enough to cause instability. Of course, as the pressure amplitude is increased, the instability becomes stronger; for example, in the range of speeds considered here, the growth rates corresponding to $\epsilon = 0.5$ and $\epsilon = 0.05$ differ by a factor of roughly three (see Table 3–2).

These stability results suggest that, under flow conditions for which two steady states are possible, Rayleigh's solution would most likely be attained, the higher-amplitude solution being unstable; on the other hand, the flow presumably would remain unsteady when no stable steady state is available. A detailed description of the dynamics would require a time-dependent simulation of the full equations which is beyond the present study. Some insight into the dynamics can be obtained, however, when the pressure amplitude is small and the forced response resembles a small-amplitude wavepacket. As discussed below, the flow then is governed by a forced NLS equation, allowing one to explore the evolution of the induced disturbance in this weakly nonlinear regime.

3.4 Weakly nonlinear forced dynamics

According to linear theory, the steady-state response to a localized pressure disturbance (Rayleigh's solution) becomes unbounded owing to a resonance phenomenon as the current speed approaches $c_{\min}$ (Whitham 1974, §13.9). In the weakly nonlinear regime, when the pressure amplitude is small, this singular behavior may be resolved by an asymptotic theory. The problem is mathematically similar to the generation of surface waves in a channel by a wavemaker oscillating near a cut-off frequency (Barnard, Mahony & Pritchard 1977), the excitation of acoustic waves in a duct by a piston oscillating near a cut-off frequency (Aranha, Yue & Mei 1982), and the forcing of gravity waves by a moving pressure distribution oscillating at resonant frequency (Akylas 1984). In the latter study, it was found that weakly nonlinear near-resonant flow is governed by a forced NLS equation and, not unexpectedly, this turns out to be the case here as well. We shall only sketch the main points in the derivation of the forced NLS equation.

3.4.1 Forced NLS equation and localized steady solutions

When the forcing amplitude is small ($\epsilon \ll 1$) and the current speed is close to resonant conditions ($\alpha \to \frac{1}{4}$), the weakly nonlinear response is expected to take the form of a modulated wavepacket with carrier wavenumber $k_{\min}$ corresponding to the minimum gravity–capillary phase speed; in the present nondimensional formulation, $k_{\min} = \frac{1}{2}$. Moreover, since the phase and group speeds are equal at this wavenumber, the wavepacket envelope is nearly stationary relative to the carrier oscillations.

Accordingly, in terms of the envelope variable $X = \epsilon^{\frac{1}{2}} x$ and the 'slow' time variable $T = \epsilon t$, the appropriate expansions for the velocity potential and free-surface elevation are

$$\phi(x,y,t) = x + \epsilon^{\frac{1}{2}}\{A(X,T)\mathrm{e}^{\mathrm{i}\frac{x}{2}} + \text{c.c.}\}\mathrm{e}^{\frac{1}{2}y} + \epsilon\{A_2(X,T)\mathrm{e}^{\mathrm{i}x} + \text{c.c.}\}\mathrm{e}^{y} + \cdots, \tag{3.19}$$

$$\eta(x,t) = \epsilon^{\frac{1}{2}}\{S(X,T)\mathrm{e}^{\mathrm{i}\frac{x}{2}} + \text{c.c.}\} + \epsilon\{S_2(X,T)\mathrm{e}^{\mathrm{i}x} + \text{c.c.}\} + \cdots, \tag{3.20}$$

where $\alpha = \frac{1}{4} + \sigma\epsilon$, $\sigma = O(1)$ being a detuning parameter.

To avoid heavy algebraic details in deriving the forced NLS equation, ignoring dependence on x for the moment we shall first obtain the forcing and nonlinear terms, which will then be combined with the familiar linear dispersive term to deduce the complete evolution equation.

Upon substitution of (3.19) and (3.20) into the dynamic and kinematic boundary conditions (3.2) and (3.3), the second-harmonic amplitudes are related to the primary-harmonic amplitudes by

$$S_2 = -S^2, \qquad A_2 = -\frac{3}{2}\,\mathrm{i}\,S^2. \tag{3.21}$$

The equations for the primary harmonic then are

$$\mathrm{i}S - A + 2\epsilon\left(S_T + \tfrac{13}{16}\,\mathrm{i}\,S^2S^*\right) = 0 \tag{3.22}$$

$$\mathrm{i}A + (1 + 2\sigma\epsilon)S + 2\epsilon\left(\mathrm{i}S_T + \tfrac{15}{32}S^2S^*\right) = -2\epsilon^{\frac{1}{2}}p(x)\mathrm{e}^{-\mathrm{i}\frac{x}{2}}. \tag{3.23}$$

Eliminating A from (3.22) and (3.23) and combining the result with the linear dispersive term, as obtained directly from the dispersion relation, yields the forced NLS equation

$$\mathrm{i}S_T + \tfrac{1}{2}\sigma S - \tfrac{1}{2}S_{XX} - \tfrac{11}{64}S^2S^* = -\pi\hat{p}_{\mathrm{m}}\delta(X), \tag{3.24}$$

where the pressure distribution has been replaced by its limiting form

$$\frac{1}{\epsilon^{\frac{1}{2}}}p\left(\frac{X}{\epsilon^{\frac{1}{2}}}\right)\exp\left(-\mathrm{i}\frac{X}{2\epsilon^{\frac{1}{2}}}\right) \longrightarrow 2\pi\hat{p}_{\mathrm{m}}\delta(X), \tag{3.25}$$

and

$$\hat{p}_{\mathrm{m}} = \frac{1}{2\pi}\int_{-\infty}^{\infty} p(x)\mathrm{e}^{-\mathrm{i}\frac{x}{2}}\,\mathrm{d}x. \tag{3.26}$$

We next look for localized steady solutions of (3.24) for $\sigma > 0$ which correspond to forced finite-amplitude steady flow states for $c < c_{\min}$. To this end, it is convenient to work in the half-domain $(0 < X < \infty)$, using the jump condition at $X = 0$ imposed by the delta function in (3.26):

$$S_X = -\pi\hat{p}_{\mathrm{m}} \qquad (X = 0). \tag{3.27}$$

Following Barnard *et al.* (1977), we write $S(X) = R(X)\,\mathrm{e}^{\mathrm{i}\varphi(X)}$ and look for solutions which decay at infinity

$$R \to 0 \qquad (X \to \infty). \tag{3.28}$$

It is straightforward to show that φ is constant and hence S is real by (3.27). Moreover, $S(0)$ is given by

$$S(0) = \pm\left\{\tfrac{32}{11}\sigma \pm \tfrac{32}{11}\sigma\left[1 - \tfrac{11}{16}\left(\frac{\pi\hat{p}_{\mathrm{m}}}{\sigma}\right)^2\right]^{\frac{1}{2}}\right\}^{\frac{1}{2}}. \tag{3.29}$$

Depending on the sign of $\hat{p}_{\mathrm{m}}S(0)$, two types of responses are possible: when $\hat{p}_{\mathrm{m}}S(0) < 0$, the envelope varies monotonically in $X > 0$ and corresponds to blowing (suction) on a depression (elevation) wave profile given implicitly by

$$X = \sigma^{-\frac{1}{2}} \ln\left(\frac{1 + (1 + 11S^2/64\sigma)^{\frac{1}{2}}}{1 + (1 + 11S(0)^2/64\sigma)^{\frac{1}{2}}}\,\frac{S(0)}{S}\right) \qquad (X > 0); \tag{3.30}$$

when $\hat{p}_{\mathrm{m}}S(0) > 0$, on the other hand, S attains a local extremum at some $X > 0$. This latter type of response may be interpreted as blowing (suction) on an elevation (depression) wave and was also found by Vanden-Broeck & Dias (1992) by numerically solving the full water-wave equations.

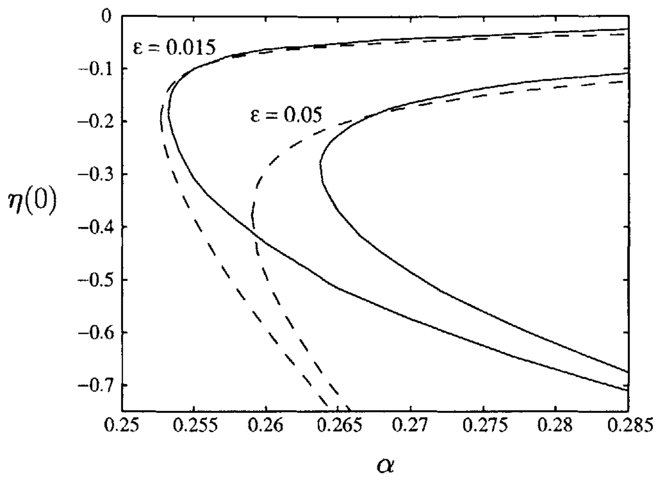

FIGURE 3–5. Comparison of response curves predicted by the forced NLS equation (- -) with response curves obtained by solving the water-wave equations (—).

In both cases, the ± sign inside the braces in (3.29) implies that two real solution branches exist for $\sigma > \sigma^* = 11^{\frac{1}{2}}\pi\hat{p}_{\mathrm{m}}/4 = 0.1804$ and converge to a limit point at $\sigma = \sigma^*$, where the quantity in the brackets vanishes. The response curves found using the forced NLS equation (for $\hat{p}_{\mathrm{m}}S(0) < 0$) are compared in Figure 3–5 with those found numerically using the full water-wave equations as described earlier, for pressure amplitudes $\epsilon = 0.05$ and $\epsilon = 0.015$. Although agreement between the limit-point locations clearly improves as ϵ is decreased, the weakly nonlinear solution rapidly loses accuracy away from the limit point.

3.4.2 Eigenvalue problem

It is most convenient to examine the stability of the localized solutions $S = \bar{S}$ over the full domain $-\infty < X < \infty$, using symmetry to extend $\bar{S}$ to $X < 0$. Again, small disturbances in the form of normal modes are assumed by writing $S(X,T) = \bar{S}(X) + \{F(X) + \mathrm{i}G(X)\}\exp(\hat{\lambda}T)$, and upon substituting into (3.24), linearizing, and separating real and imaginary parts, the following system is obtained

$$\hat{\lambda}F + \tfrac{1}{2}\sigma G + aG_{XX} + b\bar{S}^2G = 0 \tag{3.31}$$

$$\hat{\lambda} G - \tfrac{1}{2}\sigma F - aF_{XX} - 3b\bar{S}^2 F = 0. \tag{3.32}$$

It may be readily shown that for an instability to be possible (Re $\hat{\lambda} > 0$), both eigenfunctions F and G must decay to zero as $|X| \to \infty$. This eigenvalue problem was solved numerically by discretizing (3.31) and (3.32) using finite differences and then using the QR algorithm to find unstable eigenvalues.

Focussing on solutions with $\hat{p}_{\mathrm{m}} S(0) < 0$, Rayleigh's solution branch was again found to be stable. Once σ passes through the critical value σ^* corresponding to the limit point, however, a pair of real eigenvalues appears, signalling the onset of instability which becomes stronger as σ is further increased. The asymptotic analysis of weakly nonlinear forced solitary waves then confirms the results found directly using the water-wave equations and shows that the instability growth rate of forced solutions is $O(\epsilon)$ in the weakly nonlinear regime, unlike the case of free solitary waves which feature exponentially small growth rates in this limit.

A quantitative comparison of instability growth rates predicted by the forced NLS equation with those found using the water-wave equations was made for several values of ϵ between 0.0125 and 0.05. Although the error between the growth rates was significant for $\epsilon = 0.05$, agreement improves as ϵ becomes smaller. Finally, we remark in passing that both branches of the response curves with $\hat{p}_{\mathrm{m}} S(0) > 0$ were found to be unstable.

3.4.3 Initial-value problem

Based on the stability results presented above, out of the two steady states that are possible when $\sigma > \sigma^*$, one would expect Rayleigh's solution to be reached from a general locally confined initial disturbance. We confirmed this by numerically solving the forced NLS equation (3.24) on the half-domain ($X > 0$) using the semi-implicit Crank–Nicolson method described in Aranha *et al.* (1982). It was first verified that if a solution on Rayleigh's branch was used as initial condition, the response stayed on this solution, but if a solution on the higher-amplitude branch was chosen, the envelope disintegrated, consistent with the previous stability results.

Starting with quiescent initial conditions it was found that two scenarios are possible: if $\sigma > \sigma^*$, Rayleigh's steady-state solution is eventually reached after long enough times (a decaying oscillation occurs about the steady state). If, on the other hand, $\sigma < \sigma^*$, so that no steady state is available, the response remains locally confined but is inherently unsteady and features large periodic fluctuations. Before relating these results to experimental observations, we shall discuss the role of viscous dissipation.

3.5 Viscous effects

The effects of viscous dissipation cannot be entirely neglected for short water waves in the gravity–capillary regime, and a steady state cannot be maintained without some type of forcing. The stability analysis of free solitary waves presented here is therefore most meaningful if the underlying damped wave is quasi-steady, i.e., from one instant to the next, the wave profiles agree with steady profiles obtained using potential-flow theory. This quasi-steady assumption was used by Longuet-Higgins (1997) to compute theoretical decay rates of solitary waves, in good agreement with experimental observations (Longuet-Higgins & Zhang 1997). In these studies, a dramatic increase in the dissipation rate was found when the maximum surface steepness $\theta_{\max}$ rose above about 55 degrees. The stability analysis of free waves presented here then appears to have merit provided that the surface steepness is not far above this value.

When forcing, as described in this study, is in effect, the assumption of a steady underlying state used in the stability analysis is reasonable. A deviation between the forced potential-flow solutions and those that might be physically observed is expected though in proportion to the strength of viscous dissipation. Again, if the wave profile is not too steep the inviscid forced solutions appear to be reasonable.

A quantitative comparison must still be made, however, between the effects of instability and those of dissipation and so we first summarize the essential details of Longuet-Higgins's theory.

3.5.1 Model for viscous dissipation

Assuming the effects of dissipation are only moderate, the approach is to compute the rate of external working that must be done on the free surface to balance viscous stresses at the surface and thereby maintain steady motion. This work is balanced by viscous dissipation occurring throughout the body of the fluid. It is then only necessary to compute a single integral for the total rate of working done on the free surface at steady state instead of a double integral over the fluid volume. This method then provides an estimate of the dissipation rate of free solitary waves once the applied surface stresses are removed.

For a solitary wave, the total rate of working against surface stresses is defined as

$$D = \int_{-\infty}^{\infty} W \mathrm{d}s, \tag{3.33}$$

where W is the rate of working per unit length in the s direction which is the product of the normal and tangential stresses with the normal and tangential velocities relative to the stationary reference frame. For a steady solitary wave, the only contribution arises from the tangential stress in which case D is given by

$$D = 2\mu \int_{-\infty}^{\infty} q^2 \frac{\partial \theta}{\partial s} \mathrm{d}s. \tag{3.34}$$

Finally, by energy conservation we have

$$\frac{\mathrm{d}E}{\mathrm{d}t} = -D, \tag{3.35}$$

where E is the total energy of the solitary wave.

α	V_G	V_T	T	E	D/μ
0.253	0.1249	0.1270	0.2508	0.5027	1.0746
0.254	0.1378	0.1410	0.2772	0.5560	1.2337
0.257	0.1767	0.1837	0.3570	0.7174	1.6974
0.260	0.2128	0.2243	0.4314	0.8685	2.1752
0.270	0.3218	0.3536	0.6595	1.3348	3.8979
0.280	0.4189	0.4777	0.8672	1.7638	5.8698
0.290	0.5050	0.5962	1.0555	2.1566	8.0899
0.300	0.5818	0.7102	1.2278	2.5197	10.561
0.320	0.7089	0.9209	1.5239	3.1537	16.134
0.340	0.8082	1.1126	1.7688	3.6896	22.569
0.360	0.8848	1.2861	1.9703	4.1412	29.826
0.380	0.9427	1.4431	2.1358	4.5217	37.858
0.400	0.9851	1.5845	2.2699	4.8395	46.619
0.410	1.0013	1.6497	2.3270	4.9780	51.247
0.420	1.0126	1.7099	2.3742	5.0967	55.986

TABLE 3–3. Integral quantities for elevation solitary waves in deep water.

Besides the dissipation integral (3.34), the total energy E of a solitary wave is needed to compute the rate of dissipation. This energy is the sum of the gravitational potential energy V_G, the surface tension potential energy V_T, and the kinetic energy T. These energies are given by integrals that are described in detail in Longuet-Higgins (1989). We list them here for reference in terms of the dimensionless variables used in this study:

$$V_G = \frac{1}{\alpha^{1/2}} \int_{-\infty}^{\infty} \frac{1}{2}\eta^2 \, \mathrm{d}x \tag{3.36}$$

$$V_T = \int_{-\infty}^{\infty} (\mathrm{d}s - \mathrm{d}x) \tag{3.37}$$

$$T = -\frac{1}{2} \int_{-\infty}^{\infty} \eta \, \mathrm{d}\Phi. \tag{3.38}$$

The computed quantities for elevation solitary waves in deep water are listed in Table 3–3.

We define the instantaneous damping rate of a free solitary wave as

$$\frac{1}{\theta_{\max}}\frac{\mathrm{d}\theta_{\max}}{\mathrm{d}t} = \frac{1}{\theta_{\max}}\frac{\mathrm{d}\theta_{\max}}{\mathrm{d}E}\frac{\mathrm{d}E}{\mathrm{d}t}. \tag{3.39}$$

For small-amplitude gravity–capillary solitary waves for which an asymptotic (wavepacket) solution is available, the right-hand side can be computed analytically and is equal to a constant value, $-4\nu k^2$: a linear damping rate that is twice that of a train of infinitesimal waves with the same wavenumber. When the wave steepness increases though, the right hand side of (3.39) is no longer constant and the instantaneous damping rate changes with the wave steepness. For this nonlinear case, we define the average damping rate to be the inverse of the time required for the maximum surface steepness to decay by a factor of e to be consistent with time scale of instability $1/\lambda$ which is the time over which an unstable mode grows by a factor of e. The damping rate must then be computed by numerically integrating (3.39). For the forced problem, we compute the damping rate in the same way but use a free depression solitary wave with the same maximum surface steepness.

3.5.2 Competition between unstable and dissipative effects

The effect of instability on an elevation solitary wave is exponentially in the small-amplitude limit and is overwhelmed by the $O(1)$ linear dissipation described previously. The competing effects are compared in Figure 3–6 which indicates that as the wave steepness increases, the effects of instability grow to be on the same level as those of dissipation. An initial decrease in the damping rate is seen due to a decreases in $\mathrm{d}\theta_{\max}/\mathrm{d}E$ away from the small-amplitude limit. The maximum surface steepness range over which the effects are most comparable is between 7 and 25 degrees. As α approaches the limit point value ($\alpha = 0.43$), however, dissipative effects continue to increase and dominate the effects of instability.

The comparison for forced waves with pressure amplitudes $\epsilon = 0.05$ and $\epsilon = 0.5$ is shown in Figure 3–7. When forcing is weak, the effects of dissipation and instability are at the

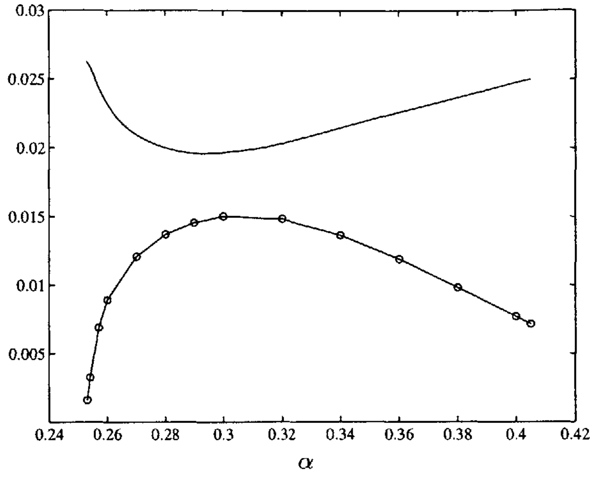

FIGURE 3–6. Comparison of growth rates (–o–) and damping rate (—) for free elevation solitary waves.

same level. When the pressure amplitude is increased by an order of magnitude though, instability begins to dominate over dissipation and so we expect that the instability of strongly forced solitary waves is physically observable.

We may use these results to comment on the usefulness of the small-amplitude stability analysis based on the forced NLS equation. For very small pressure amplitudes, the effects of instability will be overwhelmed by those of dissipation and the forced NLS equation is a poor model. For moderate pressure amplitudes ($\epsilon \geq 0.05$), however, where instability begins to be stronger than dissipation, the forced NLS equation may qualitatively make good predictions. In a recent theoretical and experimental study of Benjamin–Feir instability of moderately steep periodic gravity–capillary waves made by Shemer & Chamesse (1999) using the Zakharov integral equation modified for linear dissipation, it was found that for frequencies near the one considered in this study (12.9 Hz), the effects of viscous dissipation only modify inviscid growth rates for long disturbances in a relatively minor way. Moreover, the theoretical predictions were in reasonable agreement with experimental findings. The evidence suggests then that the time-dependent simulations discussed in the last section are not without merit, and we return to the physical implications of the results in the next section.

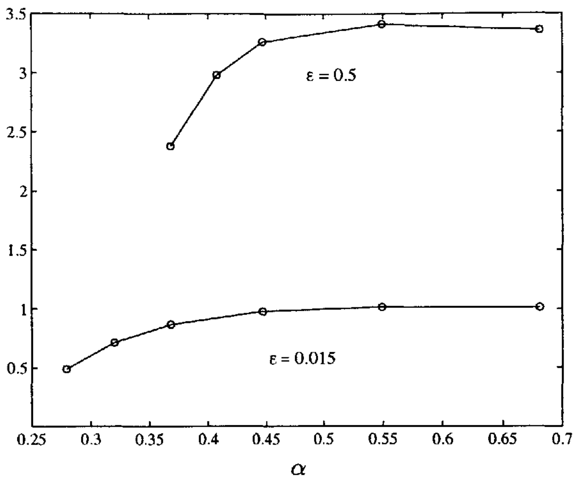

FIGURE 3–7. **Ratio of growth rate of forced depression solitary waves with damping rate of free depression waves with the same maximum surface steepness.**

3.6 Discussion

The stability of free solitary waves with a single dip is consistent with reported experimental observations of them in unforced situations (Longuet-Higgins & Zhang 1997). Based on our results, it appears that a combination of these dips (such as the one shown Figure 3–1 *e*) are stable as well provided that the dip separation is sufficient and so pairings of dips might too be physically observable.

On the theoretical side, it is of interest to know how an unstable elevation wave might evolve if the water-wave equations were solved numerically using an elevation wave as an initial condition. An approximate evolution over short times may be seen by superimposing a small proportion of the unstable mode $\tilde{\eta}$ on the underlying free-surface elevation and monitoring the development over a few instability times $1/\lambda$. When this is carried out for the elevation wave in Figure 3–1(*d*) the result is shown in Figure 3–8. The instability initially develops as a slight depression forming in the middle crest and a deepening of the right trough relative to the left trough. What occurs in the nonlinear stage of development would have to be determined by a solution of the full equations, but most likely the elevation wave splits into two depression waves that propagate at slightly different speeds. This behavior would be in agreement with what was seen using the fifth-order KdV equation for moderately steep waves (Chapter 2) and in a similar problem of solitary waves propagating on a nonlinear Bernoulli-Euler beam (Chen & McKenna 1997). Another possibility may be that the stable wave profile in Figure 3–1(e) is obtained if the value of speed parameter is near the elevation branch limit point.

The theoretical findings of this study that can be compared most directly with water-wave experiments are obtained for strongly forced depression solitary waves. This case corresponds to the situation in the forced part of the experiment by Longuet-Higgins & Zhang (1997). Two reported observations that are relevant to the present study are the persistent unsteadiness of the forced profiles and a substantial discrepancy between the maximum surface steepness and the theoretical steepness of free depression solitary waves for a given speed. While the latter disagreement might be expected, we cannot account for this discrepancy by only solving the steady problem with forcing effects.

Specifically, the theoretical maximum surface steepness of forced steady solitary waves for typical current speeds considered in the experiment can be computed by renormalizing variables such that the new pressure amplitude parameter is given by $\tilde{\epsilon} = p_{\mathrm{max}}/(\rho g T)^{\frac{1}{2}}$. Each value of $\tilde{\epsilon}$ then specifies one in a set of limit curves analogous to those shown in Figure 3–2. The theoretical curve corresponding to experimental conditions therefore depends on an estimation of p_{max}, which represents the stagnation pressure of the air impinging on the free surface, and can be made based on the geometry and data given in the experiment.

The experimental set-up consists of an air chamber in sequence with a flow straightener and a converging nozzle which issues an air jet directed downward to the water surface. The air chamber pressure (assumed to be a stagnation pressure) was reported to be always less than 3 mm of water. As an approximation, if loss only due to the flow straightener is accounted for (which turns out to be small), it is found that $\tilde{\epsilon} = 1.1$ (assuming standard conditions for water properties). We note in passing that this O(1) pressure amplitude only creates a small static free-surface deflection when there is no current, consistent with experimental observations.

The theoretical location of the limit curve is shown in Figure 3–9 along with a highly conservative curve which assumes an (arbitrary) 50% loss in air chamber pressure ($\tilde{\epsilon} = 0.55$) due to possible losses outside the flow straightener. The high surface steepness of the higher-amplitude branch of each curve is undoubtedly exaggerated since viscous effects are not being accounted for in the forced solutions. On the other hand, the location of the limit points as well as Rayleigh's solution branches occur for maximum surface steepnesses below 55 degrees and so potential-flow theory is expected to be a good model.

Comparing the experimental data with the theoretical limit curves, a likely scenario is that the true theoretical limit curve lies somewhere between the two curves shown since if Rayleigh's (stable) solution were possible in the high-loss situation ($\tilde{\epsilon} = 0.55$), the scatter in the measurements would probably not be observed. The observed scatter in the maximum surface steepnesses is most likely due to the fact that no steady states are obtainable at the speeds considered. This explanation is in agreement with the qualitative picture provided by the time-dependent simulations of the forced NLS equation. It should be noted, however, that the theoretical results predicted here are based on two-dimensional theory while the unsteadiness observed in the forced experiments had a three-dimensional aspect.

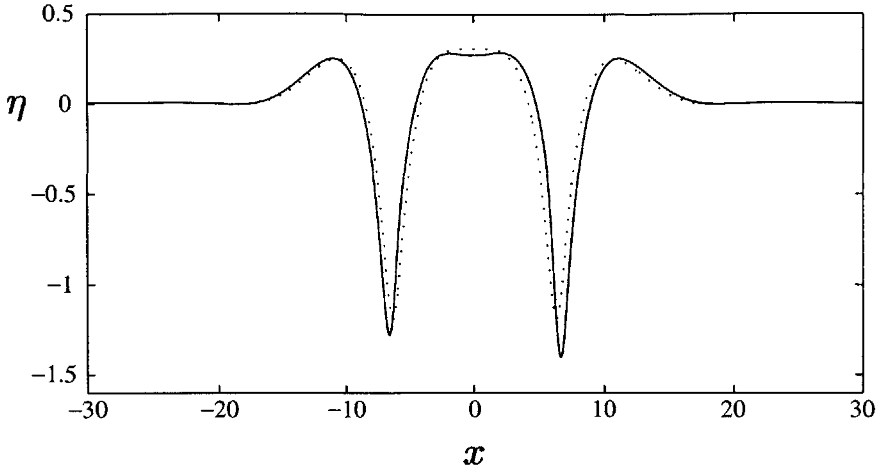

FIGURE 3–8. Approximate evolution of an unstable elevation wave shown at times $t = 0$ (· ·) and $t = 2/\lambda$ (—). The initial state has speed parameter $\alpha = 0.38$ and corresponds to point (d) in Figure 3–2.

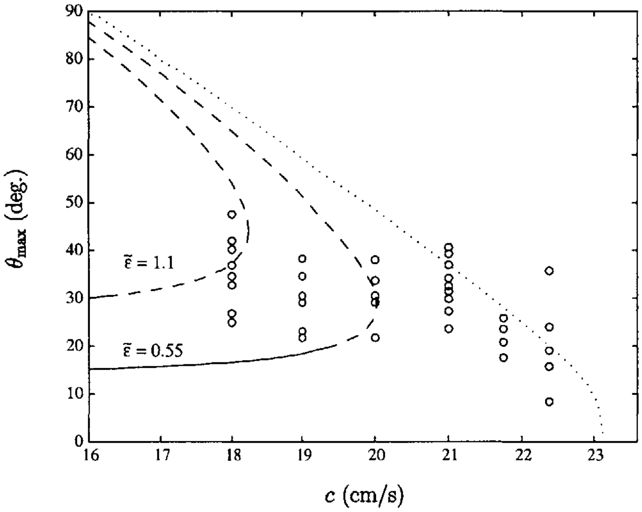

FIGURE 3–9. Comparison of theoretical steady state limit curves with experimental measurements obtained in the forced part of the experiments of Longuet-Higgins & Zhang (1997). Both stable (—) and unstable segments (- -) of each theoretical curve are indicated.

CHAPTER 4

DYNAMICS OF GRAVITY–CAPILLARY INTERFACIAL SOLITARY WAVES IN A LAYERED TWO-FLUID SYSTEM

4.1 Introduction

When an interface separating two incompressible fluid layers is subject to capillarity, a local minimum in the phase speed relation for small disturbances is generally obtained, and therefore solitary waves of the new class are expected to arise here as well. These gravity–capillary interfacial solitary waves tend to wavepackets in the small-amplitude limit, and are therefore distinct from interfacial solitary waves of the Korteweg–de Vries and Benjamin–Ono types that tend to infinitely long waves (Benjamin 1967; Ono 1975). In contrast to what was found in the free-surface problem, here the presence of additional dimensionless parameters lead to important differences in limiting wave forms and stability properties from what was found before. These differences will be demonstrated mainly by numerical solution of both the weakly and fully nonlinear wave problems which will be based upon potential-flow theory.

To demonstrate the main differences between the free-surface and interfacial-wave problems, we will focus (mostly for computational simplicity) on the case in which the upper fluid is bounded above by a rigid wall and lower fluid is deep. In this geometry, weakly nonlinear long gravity–capillary waves were studied by Benjamin (1992; 1996) who derived a model equation and proved the existence and global stability of a small-amplitude elevation solitary wave. These results were latter verified using different methods by Albert, Bona & Restrepo (1999) who also explicitly computed the elevation solitary wave profile.

Approximations of solitary-wave solutions to the Benjamin equation were obtained by Akylas, Dias & Grimshaw (1998) using the nonlinear Schrödinger (NLS) equation. According to their analysis, in addition to an elevation wave, a depression wave type should also exist. Moreover, extrapolating the analysis of Chapter 2, it is expected that this solitary wave type may be unstable. Both the existence and linear instability of the depression wave is confirmed here by numerical solutions of both the Benjamin equation and the full hydrodynamic equations.

The nonlinear dynamics of these solitary waves will then be considered by numerically solving the time-dependent Benjamin equation. Of particular interest from an experimental standpoint is the possibility that interfacial gravity–capillary solitary waves can evolve out of general localized initial conditions. Because of a mathematical similarity between the Benjamin and KdV equations, it is also of interest to know whether Benjamin solitary waves have other soliton properties: stable emergence from collisions with other solitary waves for example.

The accuracy of approximate solitary-wave solutions obtained using the Benjamin equation will then be compared with solutions of the full hydrodynamic equations obtained numerically using the boundary-integral-equation method (Laget & Dias 1997). Using the full equations, it will be shown that the qualitative picture of solitary waveforms predicted by the Benjamin equation are obtained over a fairly broad range of parameter space. Finally, using a linear stability analysis of solutions to the full equations, results will be presented which support a hypothesis that the stability and limiting wave forms of gravity–capillary interfacial solitary waves in the case of two fluid layers of finite depth depends critically on the depth and density ratios.

4.2 Motivation

The geometry of general interest consists of a layer of incompressible fluid of density ρ_2 and thickness h_2 which lies above an incompressible fluid of higher density ρ_1 and thickness h_1. Denoting the coefficient of interfacial tension by T and the gravitational acceleration by g, the phase speed c of infinitesimal waves with wavenumber k is given by

$$c^2 = \frac{g(\rho_1 - \rho_2) + Tk^2}{k(\rho_1 \coth kh_1 + \rho_2 \coth kh_2)}. \tag{4.1}$$

An asymptotic approximation of small-amplitude gravity–capillary solitary waves may be obtained by either of two approaches analogous to those followed in the free-surface problem. In the first approach, a two-scale perturbation expansion of solitary wavepackets can be made using the NLS equation provided that the wave speed is slightly below the minimum phase speed. As discussed before in the free-surface problem, a shortcoming of the NLS approach is that it neglects the phase of the wave which is expected to influence stability.

To obtain insight into stability, a weakly nonlinear long-wave approach may instead be followed leading to a fifth-order Korteweg–de Vries (KdV) equation as discussed in Laget & Dias (1997) and shown here in steady form as

$$\left(\frac{1}{F^2} - \frac{1}{F^{*2}}\right)\eta + (W^* - W)\eta_{xx} + \frac{1}{45}(H_1^3 + RH_2^3)\eta_{xxxx} + \frac{3}{2H_1^2}\left(1 - \frac{R}{H^2}\right)\eta^2 = 0,$$

where

$$W = \frac{T}{\rho_1(h_1 + h_2)c^2}, \quad F^2 = \frac{c^2}{(1-R)g(h_1+h_2)}, \quad W^* = \frac{1}{3}(H_1 + RH_2), \quad F^{*2} = \frac{1}{H_1} + \frac{R}{H_2},$$

and

$$R = \frac{\rho_2}{\rho_1}, \qquad H = \frac{h_2}{h_1}, \qquad H_1 = \frac{h_1}{h_1 + h_2}, \qquad H_2 = \frac{h_2}{h_1 + h_2}.$$

The validity of the fifth-order KdV equation depends on $W \approx W^*$ and $F^2 \approx F^{*2}$. The presence of additional physical parameters not found in the free-surface problem ($R = 0$) lead to an interesting result suggested by the form of the coefficient of the nonlinear term: keeping the signs of all the linear terms positive, it is possible to make the nonlinear coefficient negative which implies that small-amplitude elevation waves would be stable — a situation opposite to the free-surface case. This condition can be physically obtained if the thickness of the lower fluid is a few times that of the upper fluid for instance and would be qualitatively consistent with Benjamin's proof of a stable elevation solitary wave when the lower fluid is infinitely deep. Furthermore, the profiles of moderately steep gravity–capillary solitary waves would appear to reverse: the picture of deep troughs and short crests would flip across the undisturbed free-surface level.

Because the fifth-order KdV equation is valid for restrictive parameter values, it would be of interest to know if such an exchange of stabilities can be observed over less restrictive ranges of parameter space. To this end, linear stability analysis will be used in conjunction with the full hydrodynamic equations. To probe the aforementioned points, it suffices to consider the case in which the lower fluid is infinitely deep ($h_1 \to \infty$). In this limit, (4.1) reduces to

$$c^2 = \frac{g(\rho_1 - \rho_2) + Tk^2}{\rho_1 |k| + \rho_2 \coth kh}, \tag{4.2}$$

where from here on $h \equiv h_2$.

4.3 Weakly nonlinear solitary wave dynamics

4.3.1 Benjamin equation

To explore the dynamics of gravity–capillary solitary waves with speeds slightly below the minimum phase speed, an asymptotic equation can be developed using the long-wave approximation as described in Benjamin (1992). Specifically, in the limit of very long waves, c may be expanded in powers of $|k|h$ to obtain

$$c = c_0 \left\{ 1 - \frac{1}{2}\frac{\rho_1}{\rho_2}|k|h + \left[\frac{1}{2}\frac{T}{g(\rho_1 - \rho_2)h^2} + \left(\frac{3}{4}\frac{\rho_1^2}{\rho_2^2} - \frac{1}{6} \right) \right] (kh)^2 \right\}, \tag{4.3}$$

where

$$c_0 = \left[gh \left(\frac{\rho_1}{\rho_2} - 1 \right) \right]^{\frac{1}{2}}. \tag{4.4}$$

It is essential that the wavenumber k_{min} at which the minimum linear phase speed is attained satisfies $k_{\text{min}}h \ll 1$ which requires a balance between the first and second-order dispersive terms. This balance can be obtained if the fluid densities are close and interfacial tension is relatively high:

$$\frac{T}{g(\rho_1 - \rho_2)h^2} = O\left(\frac{1}{kh}\right). \tag{4.5}$$

By consideration of the linear pseudo-differential operator corresponding to (4.3) and the leading-order effects of self-steepening, one may infer the evolution equation governing the wave amplitude η^* in terms of the normalized variables

$$\eta = \frac{\eta^*}{a}, \qquad x = \frac{x^*}{l}, \qquad t = \frac{c_0}{l}t^*,$$

where a represents a typical wave amplitude, l a typical wavelength, and the starred quantities are dimensional. Benjamin's equation in normalized form then reads

$$\eta_t + \eta_x - \epsilon\eta\eta_x - \alpha\mathcal{H}(\eta_{xx}) - \beta\eta_{xxx} = 0, \tag{4.6}$$

where

$$\epsilon = \frac{3}{2}\frac{a}{h}, \qquad \mu = \frac{1}{2}\frac{\rho_1}{\rho_2}\frac{h}{l}, \qquad \beta = \frac{T}{2g(\rho_1 - \rho_2)\, l^2},$$

and $\mathcal{H}$ denotes the Hilbert transform,

$$\mathcal{H}(\cdot) = \int_{-\infty}^{\infty} \frac{(\cdot)}{s-x} \mathrm{d}s.$$

To obtain a balance between weak nonlinear ($\epsilon \ll 1$) and weak dispersive ($\mu \ll 1$) effects we must have $\epsilon = O(\mu)$. In addition, we require $\mu = O(\beta)$ which is equivalent to condition (4.5). It is noted in passing that as $\rho_2 \to 0$, the parameter $\mu \to \infty$ and so a free-surface case cannot be recovered from the Benjamin equation.

Under further transformation

$$t' = \epsilon t, \qquad x' = (\epsilon/\beta)^{1/3}(x-t), \qquad \eta' = \tfrac{1}{2}(\epsilon/\beta)^{1/3}\eta,$$

we arrive at a form of Benjamin's equation suitable for time-dependent simulation:

$$\eta_t - 2\eta\eta_x - 2\gamma\mathcal{H}(\eta_{xx}) - \eta_{xxx} = 0, \tag{4.7}$$

where the primes have been dropped and the parameter $\gamma \equiv \mu/2\epsilon^{\frac{1}{3}}\beta^{\frac{2}{3}} = O(1)$.

4.3.2 Solitary waves

A travelling wave solution with speed below the long-wave speed can be sought in terms of $\eta(x,t) = \bar{\eta}(\xi)$ $(\xi = x + Ct)$. The steady Benjamin equation then assumes the form

$$C\bar{\eta} - \bar{\eta}^2 - 2\gamma\mathcal{H}(\bar{\eta}_\xi) - \bar{\eta}_{\xi\xi} = 0. \tag{4.8}$$

If the speed parameter C is taken to be 1, without loss of generality (as $\bar{\eta}$ and ξ may be rescaled), a one-parameter family of solitary-wave solutions is expected characterized by $\gamma < 1$: $\gamma = 0$ corresponds to the known KdV solution $\frac{3}{2}\mathrm{sech}(\xi/2)^2$, while in the limit

$\gamma \to 1$ the tails of the solitary wave feature decaying oscillations which corresponds to a small-amplitude wavepacket near the bifurcation point.

Equation (4.8) was solved numerically using fourth-order accurate finite differences for the spatial derivatives and an evaluation of the Hilbert transform using the discrete Fourier transform. The nodal values of $\bar{\eta}$ were solved for using Newton's method. Both elevation and depression wave solutions are shown in Figure 4–1 for $\gamma = 0.94$ with $C = 1$. The elevation wave was obtained by starting at the KdV limit $\gamma = 0$ and then slowly increasing γ towards 1, while the depression wave was obtained by reflecting an elevation wave with $\gamma \approx 1$ across the horizontal.

To confirm the expected stability results for elevation waves and to determine the stability of depression waves, equation (4.7) was solved numerically using the same spatial discretization as in the steady problem and a predictor-corrector scheme for time-stepping (see Appendix A). Time-dependent solutions showing the evolution of the elevation and depression waves shown in Figure 4–1 are displayed in Figures 4–2 and 4–3, respectively. While the elevation wave propagates stably as expected, the depression wave is unstable and eventually decomposes into two elevation waves.

To test for soliton-like properties, (4.7) was again solved numerically this time using two elevation solitary waves with speeds $C = 1$ and $C = 1.5$. As can be seen in Figure 4–4, the higher amplitude wave passes through the smaller amplitude wave and both waves remain relatively intact after the collision. In contrast to collisions of stable depression waves seen in the free-surface problem using the fifth-order KdV equation, here small-amplitude radiation can be seen in the trail of each solitary wave indicating that the interaction is not completely conservative.

Finally, a simulation using a Gaussian initial condition, $u(x, 0) = \exp(-0.5\ x^2)$, was performed for $\gamma = 0.97$. The results in Figure 4–5 show the emergence of an elevation solitary wave along with radiation. Generally, as the width of the Gaussian increases an elevation wave will still emerge but with more radiation.

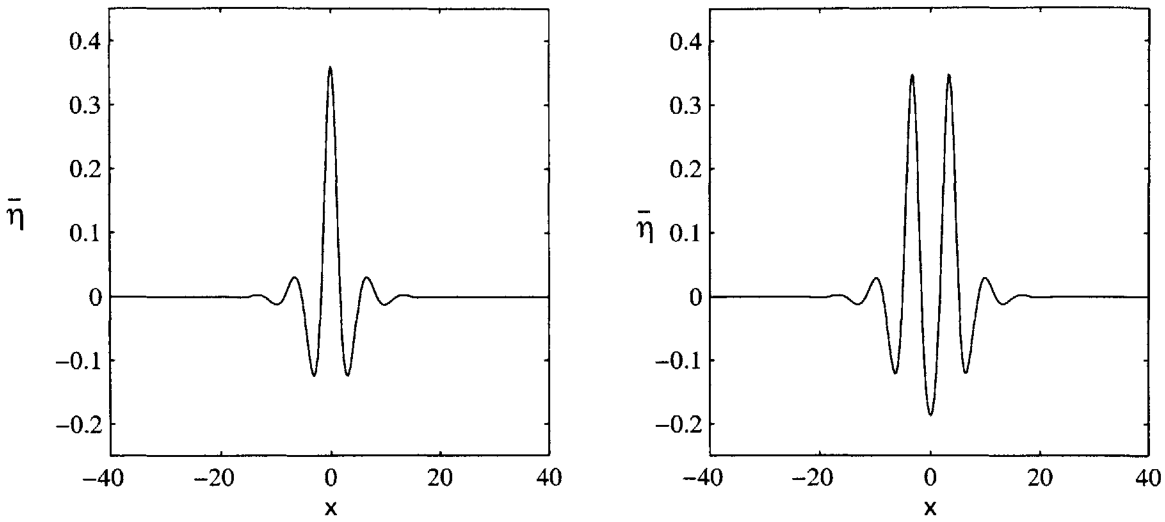

FIGURE 4–1. Elevation (left) and depression (right) solitary-wave solutions of the steady Benjamin equation (4.8) for $\gamma = 0.94$ and $C = 1$.

4.4 Fully nonlinear interfacial solitary waves

In this section, a comparison of the steady solitary-wave solutions of the Benjamin equation will be made with profiles obtained using the full hydrodynamic equations. An advantage of the latter method is that no restrictions are placed on the values of dimensionless parameters; for instance, the wavelength and amplitude of the solitary wave may be of the same order as the thickness of the upper fluid.

4.4.1 Wavepackets

In preparation for presenting results of computations using the full equations, it is first helpful to examine the necessary relationships between critical values of the system parameters which define bifurcation points about which small-amplitude wavepackets are expected.

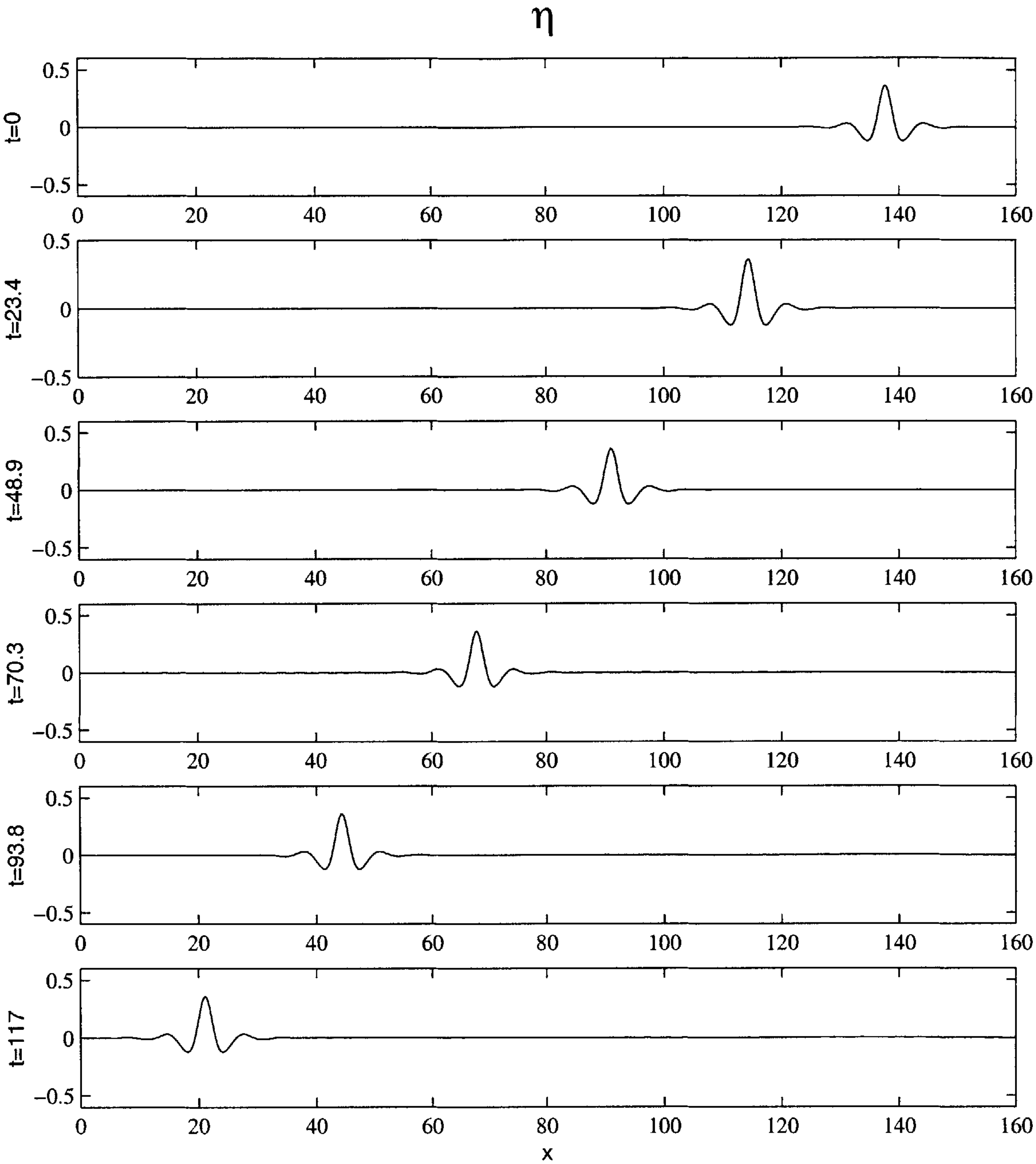

FIGURE 4–2. Numerical solution of the Benjamin equation (4.7) showing the stable evolution of an elevation solitary wave shown in Figure 4–1 with $\gamma = 0.94$.

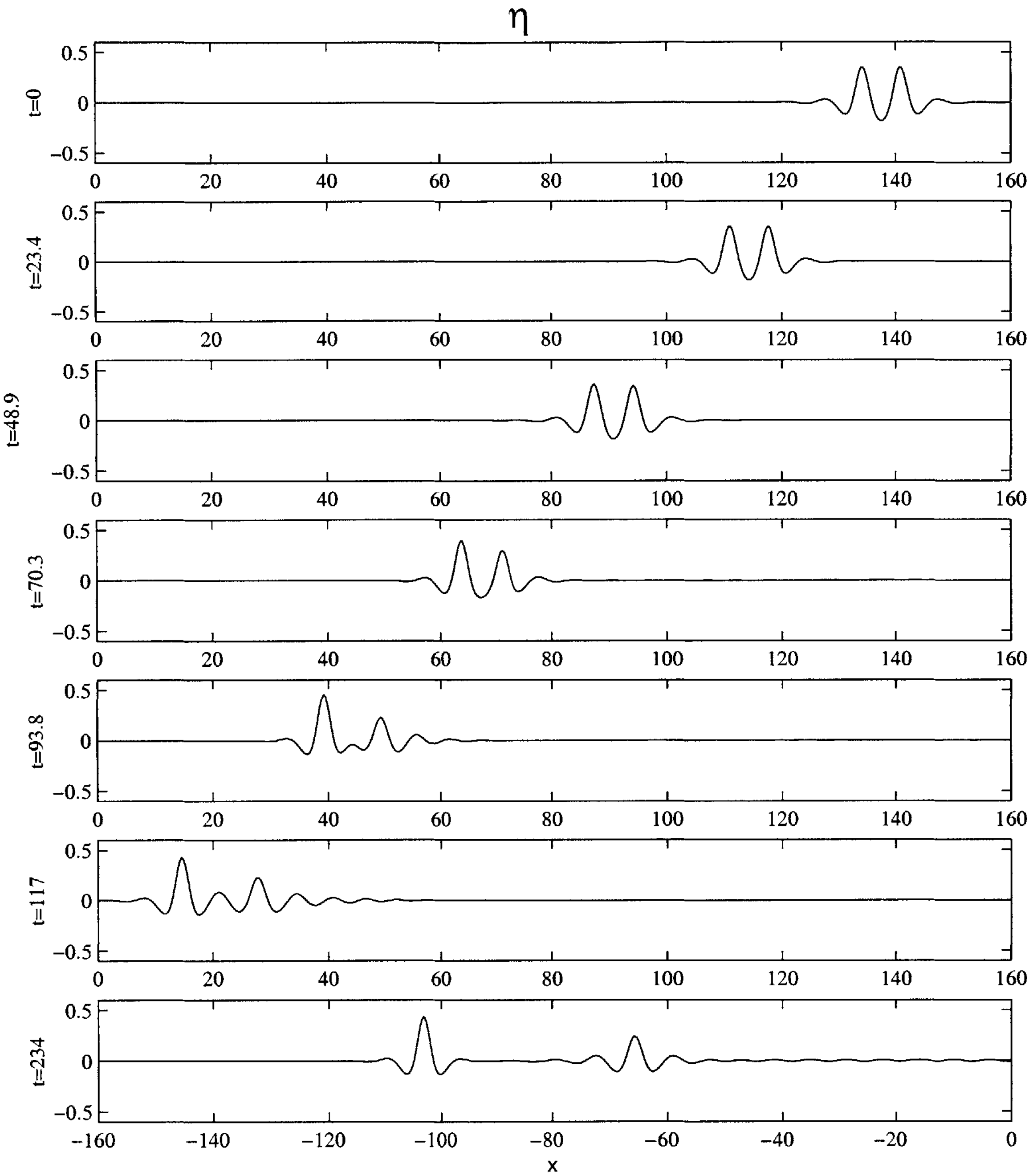

FIGURE 4–3. Numerical solution of the Benjamin equation (4.7) showing the unstable evolution of a depression solitary wave shown in Figure 4–1 with $\gamma = 0.94$. Two stable elevation waves are eventually obtained.

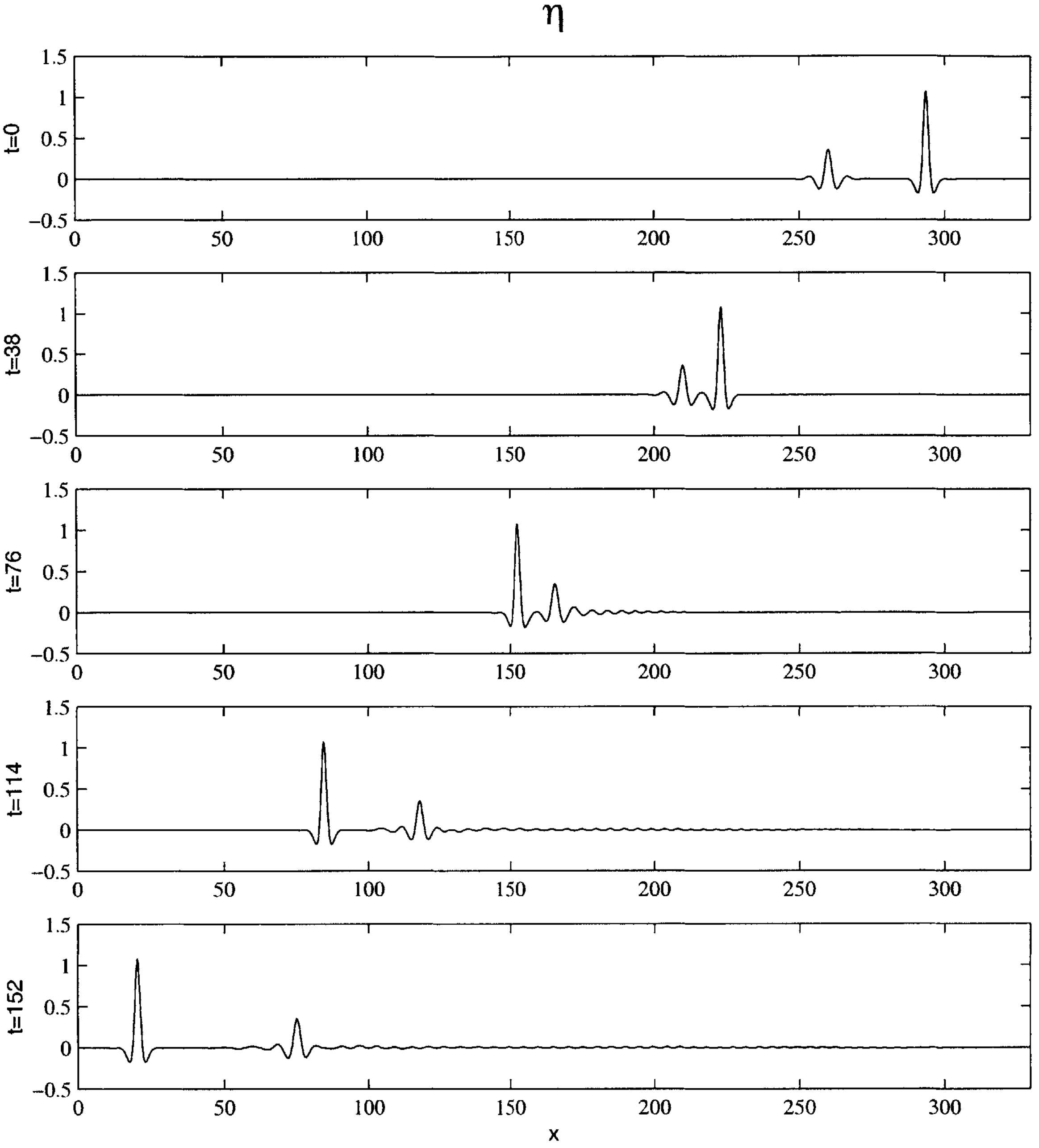

FIGURE 4–4. Numerical solution of the Benjamin equation (4.7) showing the collision of two elevation solitary waves. The parameter $\gamma = 0.94$. The larger amplitude wave has speed $C = 1.5$, while the small amplitude wave has $C = 1.0$.

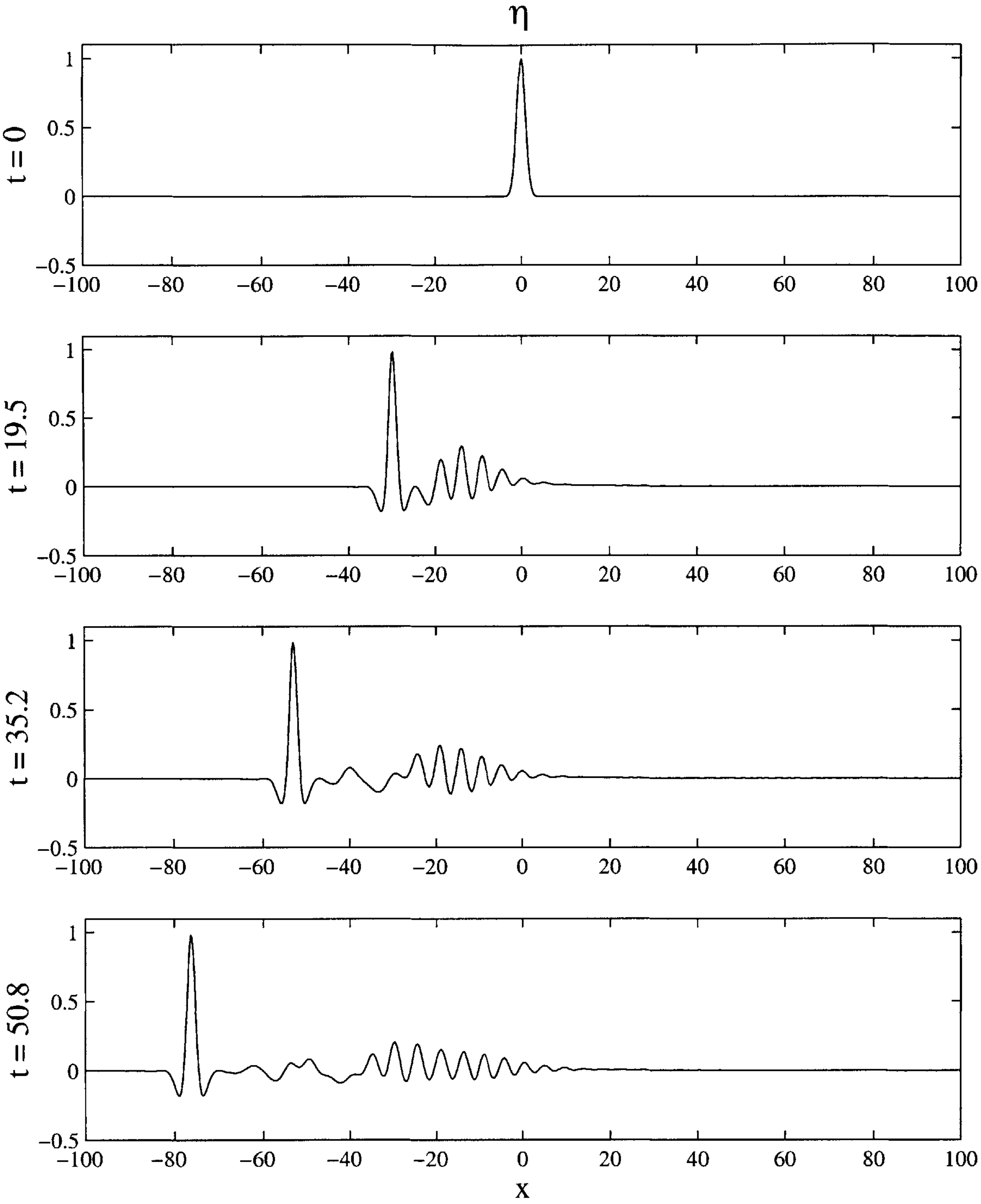

FIGURE 4–5. Numerical solution of the Benjamin equation (4.7) with $\gamma = 0.97$ using a Gaussian initial condition $u(x,0) = \exp(-0.5\,x^2)$.

Using h as a length scale and the solitary wave speed c as a speed scale the linear phase speed relation (4.2) becomes

$$D^2(R, W, F^2; K) = \frac{\frac{(1-R)}{F^2} + WK^2}{|K| + KR \coth K} = 1, \tag{4.9}$$

where

$$R = \frac{\rho_2}{\rho_1}, \qquad W = \frac{T}{\rho_1 h c^2}, \qquad F^2 = \frac{c^2}{gh}, \qquad K = kh. \tag{4.10}$$

A transition from a speed slightly above to slightly below the minimum phase speed corresponds to two real roots (wavenumbers) in (4.9) first coalescing and then taking on imaginary parts. As R, W and F^2 are varied, the condition which defines the minimum phase speed then is a double root of (4.9). Regarding R and K as parameters the critical speed then corresponds to critical values $W = W^*$ and $F^2 = F^{*2}$ which are given by the following relations

$$\frac{1}{F^{*2}} = \frac{K^*}{2(1-R)} \left[1 + R \ \coth K^* + \frac{RK^*}{\sinh^2 K^*} \right], \tag{4.11}$$

$$W^* = \frac{1}{2K^*} \left[1 + R \coth K^* - \frac{RK^*}{\sinh^2 K^*} \right]. \tag{4.12}$$

In Figure 4–6, the relations (4.11) and (4.12) have been plotted in terms of F^{*2} versus W^* for various values of the density ratio R. The region near the origin of the plot corresponds to large K^*, while in the long-wave limit ($K^* \to 0$), F^{*2} tends to $F_0^2 = (1-R)/R$ which corresponds to the long-wave speed c_0.

In terms of the current normalization, the conditions necessary for the Benjamin equation to be valid can be seen by expanding D in powers of $|K|$:

$$1 = \sqrt{\frac{1-R}{F^2 R}} \left\{ 1 - \frac{|K|}{2R} + \left[\frac{1}{2} \left(W - \frac{(1-R)}{3F^2} + \frac{(1-R)}{F^2 R^2} \right) \frac{F^2}{1-R} - \frac{1}{8R^2} \right] K^2 + O(|K|^3) \right\}.$$

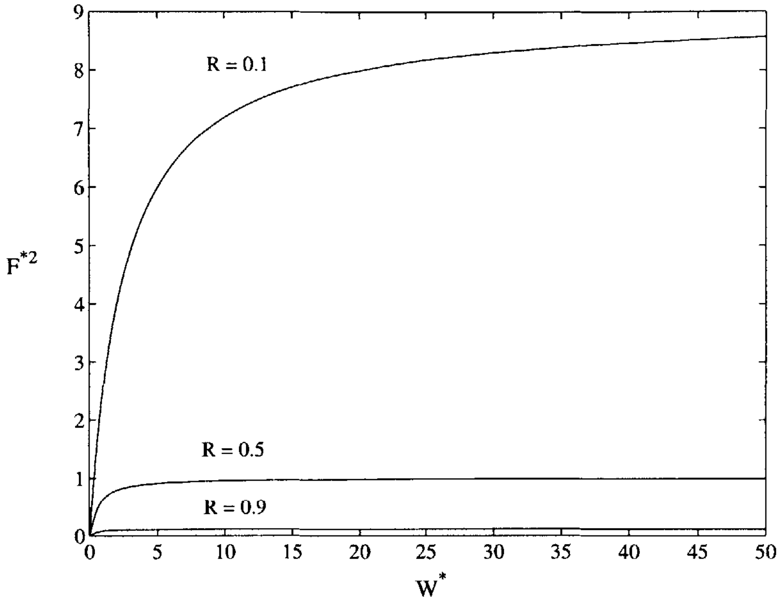

FIGURE 4–6. Curves relating the critical values of F^{*2} and W^* at which solitary wavepackets bifurcate from infinitesimal periodic waves plotted for different values of the density ratio R. The large K^* limit lies near the origin, while the small K^* limit corresponds to $W^* \to \infty$. In terms of F^2 and W, solitary waves bifurcate slightly below each curve.

(4.13)

If the Froude number is slightly less than F_0^2, i.e., $F_0^2 - F^2 = O(|K|) > 0$, we have then

$$\frac{1}{2}\left(1 - \frac{F^2}{F_0^2}\right) - \frac{|K|}{2R} + \frac{W_0}{2R}K^2 = 0, \tag{4.14}$$

provided that

$$W_0 = O\left(\frac{1}{K}\right), \tag{4.15}$$

where $W_0 = T/\rho_1 h c_0^2$. Condition (4.15) is equivalent to (4.5). Based on (4.14) and comparison with (4.6) the steady Benjamin equation in the current normalization reads

$$\frac{1}{2}\left(1 - \frac{F^2}{F_0^2}\right)\eta - \frac{3}{4}\eta^2 - \frac{1}{2R}\mathcal{H}(\eta_x) - \frac{W_0}{2R}\eta_{xx} = 0. \tag{4.16}$$

Benjamin's equation is then expected to yield a close approximation to solutions computed using the full equations provided that $F^2 \approx F_0^2$ and $W \gg 1$. In preparation for a comparison of the results of the two computational approaches, the details of the steady nonlinear computation using the boundary-integral-equation method will first be summarized.

4.4.2 Formulation of steady problem

The full equations for the steady nonlinear interfacial-wave problem read

$$\phi_{1xx} + \phi_{1yy} = 0 \qquad (-\infty < x < \infty,\ -\infty < y < \eta), \tag{4.17}$$

$$\phi_{2xx} + \phi_{2yy} = 0 \qquad (-\infty < x < \infty,\ \eta < y < h), \tag{4.18}$$

$$\rho_1\left[\phi_{1t} + \tfrac{1}{2}(\phi_{1x}^2 + \phi_{1y}^2) + g\eta\right] - \rho_2\left[\phi_{2t} + \tfrac{1}{2}(\phi_{2x}^2 + \phi_{2y}^2) + g\eta\right] - T\frac{\eta_{xx}}{(1+\eta_x^2)^{\frac{3}{2}}} = \tfrac{1}{2}(\rho_1 - \rho_2)c^2, \qquad (y = \eta) \tag{4.19}$$

$$\eta_t + \phi_{1x}\eta_x = \phi_{1y} \qquad (y = \eta), \tag{4.20}$$

$$\eta_t + \phi_{2x}\eta_x = \phi_{2y} \qquad (y = \eta), \tag{4.21}$$

$$(\phi_{1x}, \phi_{1y}) \to (c, 0) \qquad (x^2 + y^2 \to \infty,\ \ y < \eta), \tag{4.22}$$

$$\phi_{2y} = 0 \qquad (y = h), \tag{4.23}$$

$$\phi_{2x} = c \qquad (|x| \to \infty). \tag{4.24}$$

To compute nonlinear steady solutions of (4.17–4.24), the boundary-integral-equation method is used in the same way as before to handle the lower fluid, but now an additional integral equation must be included to account for the upper fluid. Using ϕ_1 (on the interface) as an independent variable, the unknowns are then $x_{\phi 1}$ and $y_{\phi 1}$ as before, but now the velocity potential of the upper fluid ϕ_2 (on the free surface) may be regarded as the additional unknown. It is convenient to introduce a link between the two potentials on the interfacial streamline ($\psi \equiv \psi_1 = \psi_2 = 0$):

$$\phi_2 = g(\phi_1) \qquad (\psi = 0). \tag{4.25}$$

If the subscript on ϕ_1 is now dropped, the normalized and transformed Bernoulli equation reads

$$\frac{1}{2(x_\phi^2 + \eta_\phi^2)}\left(1 - R{g_\phi}^2\right) + (1 - R)\frac{\eta}{F^2} + W\frac{\eta_\phi x_{\phi\phi} - x_\phi \eta_{\phi\phi}}{(x_\phi^2 + \eta_\phi^2)^{\frac{3}{2}}} = \tfrac{1}{2}(1 - R) \qquad (\psi = 0). \tag{4.26}$$

Applying Cauchy's theorem to $x_\phi + \mathrm{i}y_\phi - 1$ using a contour enclosing the lower-fluid region ($\psi < 0$) we obtain as before

$$x_\phi = 1 - \frac{1}{\pi}\int_{-\infty}^{\infty} \frac{\eta_\xi}{\xi - \phi}\mathrm{d}\xi \qquad (\psi = 0). \tag{4.27}$$

The solid boundary condition (4.23) which applies at $\psi = 1$ can be satisfied by defining an image system (a reflection of the upper-fluid between $\psi = 0$ and $\psi = 1$ about the line $\psi = 1$) and the properties

$$\frac{\partial x}{\partial \phi_2}(\phi_2, \psi = 0) = \frac{\partial x}{\partial \phi_2}(\phi_2, \psi = 2) \qquad \frac{\partial y}{\partial \phi_2}(\phi_2, \psi = 0) = -\frac{\partial y}{\partial \phi_2}(\phi_2, \psi = 2). \tag{4.28}$$

Applying Cauchy's theorem to $x_{\phi_2} + \mathrm{i}y_{\phi_2} - 1$ using a rectangular contour that encloses the upper fluid physical region and its image, the following expression is obtained upon taking the real part of the result and using ϕ as an independent variable

$$\frac{x_\phi}{g_\phi} = 1 + \frac{1}{\pi}\int_{-\infty}^{\infty} \frac{\eta_\xi}{g(\xi) - g(\phi)}\mathrm{d}\xi + \frac{1}{\pi}\int_{-\infty}^{\infty} \frac{[g(\xi) - g(\phi)]\eta_\xi + 2(x_\xi - g_\xi)}{[g(\xi) - g(\phi)]^2 + 4}\mathrm{d}\xi \qquad (\psi = 0) \tag{4.29}$$

where, again, the integral in (4.27) and the first integral in (4.29) are of the principal-value type. Because only symmetric waves are being considered, the two integral equations can be rewritten on the half domain $\phi \geq 0$. The numerical solution procedure is along the same lines as that used in the free-surface problem except here η_ϕ and g are solved for simultaneously. Specifically, during the iteration procedure (4.27) directly yields x_ϕ given some initial guess for η_ϕ; equations (4.26) and (4.29) can then be evaluated and η_ϕ and g are updated using Newton's method. The boundary conditions that must be applied to solve for symmetric solitary waves are

$$y_\phi(0) = y_\phi(\phi_{\max}) = 0 \qquad x_\phi(\phi_{\max}) = 1 \qquad g_\phi(\phi_{\max}) = 1.$$

For small values of R, initial guesses for elevation and depression waves were provided by the free-surface computations done in Chapter 3. For high values of R, (4.27) was modified to account for a lower fluid of finite-depth in which case an initial guess was provided by the steady KdV equation (Laget & Dias 1997). Once this solution was obtained, the depth of the lower fluid was increased to infinity. Alternatively, an asymptotic approximation of solitary waves can be made using the steady NLS equation for interfacial gravity–capillary waves when the lower fluid is deep. Yet another approach is to use solutions of the steady Benjamin equation (4.16) when $R \approx 1$, $W \gg 1$ and $F^2 \approx F_0^2$.

4.4.3 Comparison of solitary wave profiles

We have chosen for the comparison a density ratio $R = 0.9$ and a Weber number $W = 3.4$. The latter condition is expected to reasonably satisfy $W \gg 1$. For the critical value of $W^* = 3.4$, the corresponding bifurcation point value of F^2 is $F^{*2} = 0.1111$. By detuning F^2 below F^{*2}, the wave amplitude can then be increased. A comparison between solitary waves obtained by the two different approaches is shown in Figure 4–7. As can be seen, the error in $\eta(0)$ decreases as F^{*2} is approached; the maximum error is 14%, while the minimum error is 4%. The discrepancy in the shapes of the large-amplitude profiles is expected given the stronger nonlinearity in the full problem. The discrepancy between the wavelengths in the smallest amplitude case is expected to decrease as W is increased further since the dispersion relation of Benjamin's equation then becomes a better approximation to that of the linearized full equations.

4.4.4 Limiting wave forms

The aim of this section is to demonstrate how the shape of moderately steep gravity–capillary interfacial solitary waves changes as the density ratio is varied. Specifically, when $R = 0$ (the free-surface problem) solitary waves have deep troughs and short crests as was seen in Chapter 3; this differs from the approximations of elevation waves computed using the Benjamin equation which feature shallow troughs and a tall center crest. Roughly speaking, the profiles of moderately steep gravity–capillary solitary waves flips about the horizontal when the density ratio rises about a certain value which is hinted at by the fifth-order KdV equation discussed earlier.

To demonstrate this phenomenon and the associated changes in stability to be discussed in the next section, only the case $W = 1$ will be considered. As before, for a given value of R, F^2 can be decreased from its bifurcation point value to a point where the profile no longer resembles a wavepacket. The qualitative change in the profiles of elevation and depression waves is shown in Figure 4–8. The change in elevation wave profiles occurs for $R \approx 0.0325$, while that for the depression waves occurs for $R \approx 0.065$. Based on results presented in Section 4.3 and Chapters 2 & 3, an exchange of stability is expected to be

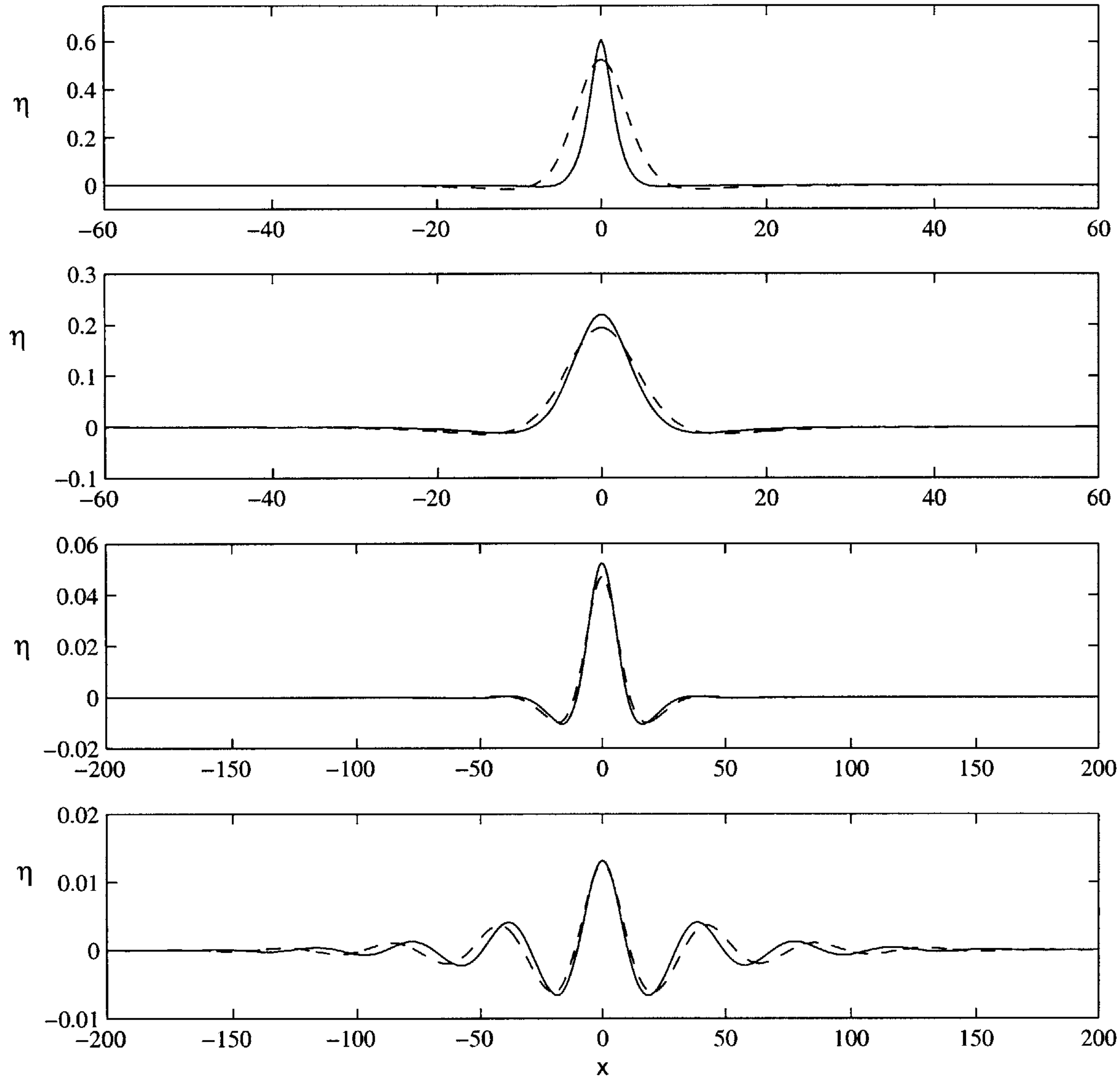

FIGURE 4–7. Comparison of solitary-wave solutions of the full hydrodynamic equations (solid line) with solutions of the steady Benjamin equation (4.16) (dotted line). The parameter values are $W = 3.4$, $R = 0.9$, and starting from the top down $F^2 = 0.04, 0.08, 0.098, 0.1017$. The bifurcation point corresponds to $F^{*2} = 0.1111$.

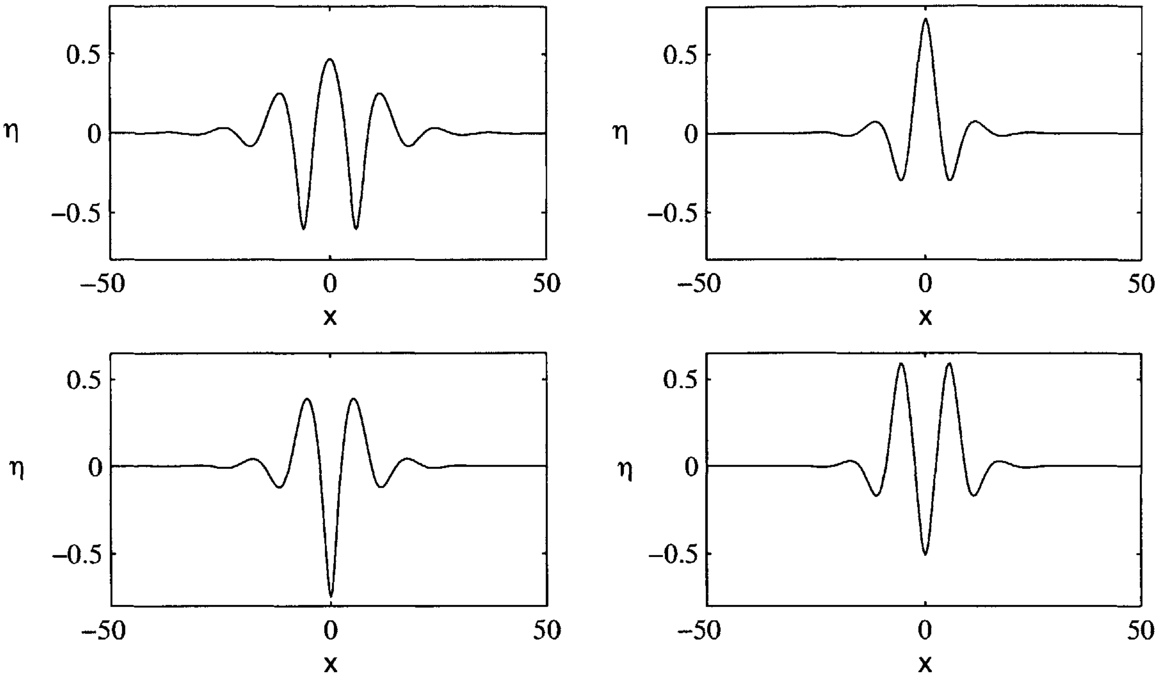

FIGURE 4–8. Change in the limiting forms of elevation and depression interfacial solitary waves as the density ratio R is varied. Elevation waves are shown in the top row with $R = 0.03, F^2 = 3.153$ (left) and $R = 0.035, F^2 = 2.799$ (right). Depression waves are shown in the bottom row with $R = 0.06, F^2 = 2.679$ (left) and $R = 0.07, F^2 = 2.325$ (right).

associated with the change in limiting wave forms. To pin down at what density ratio this is expected to occur, a logical starting point is to examine the stability of small-amplitude solitary waves using the full equations.

4.5 Exchange of stabilities

4.5.1 Formulation of stability problem

The stability analysis is along the same lines as that carried out in the free-surface case except now perturbations to the upper-fluid velocity potential and stream functions must be considered:

$$\phi_2(x,y,t) = \Phi_2(x,y) + \tilde{\phi}_2(x,y,t), \tag{4.30}$$

$$\psi_2(x,y,t) = \Psi_2(x,y) + \tilde{\psi}_2(x,y,t), \tag{4.31}$$

with $\tilde{\phi}_{2x} = \tilde{\psi}_{2y}$ and $\tilde{\phi}_{2y} = -\tilde{\psi}_{2x}$ so as to satisfy Laplace's equation.

Again, the arclength s of the undisturbed interfacial streamline is used as an independent variable, $s = 0$ being the point of symmetry. The steady state of the upper fluid may be represented in terms of the magnitude of the velocity vector on the interface, $q_2 = (\Phi_{2x}^2 + \Phi_{2y}^2)^{\frac{1}{2}}$, and the angle the velocity vector makes with the horizontal, $\theta = \arctan\,(\mathrm{d}H/\mathrm{d}x)$. Assuming normal-mode perturbations $\propto \exp(\lambda t)$ and making use of $\Phi_{2x} = q_2 \cos\theta$, $\mathrm{d}x = \mathrm{d}s \cos\theta$, the linearized form of (4.19) then transforms to

$$\begin{aligned}\lambda(\tilde{\phi}_1 - R\,\tilde{\phi}_2) = -q_1\frac{\mathrm{d}\tilde{\phi}_1}{\mathrm{d}s} + R\,q_2\frac{\mathrm{d}\tilde{\phi}_2}{\mathrm{d}s} - \left(q_1\frac{\mathrm{d}(q_1 \sin\theta)}{\mathrm{d}s} - R\,q_2\frac{\mathrm{d}(q_2 \sin\theta)}{\mathrm{d}s} + \frac{1-R}{F^2}\right)\tilde{\eta}\\ +W\frac{1}{\cos\theta}\frac{\mathrm{d}}{\mathrm{d}s}\left(\cos^2\theta\frac{\mathrm{d}\tilde{\eta}}{\mathrm{d}s}\right).\end{aligned} \tag{4.32}$$

By similar manipulations, the two kinematic boundary conditions become

$$\lambda\tilde{\eta} = -q_1\frac{\mathrm{d}\tilde{\eta}}{\mathrm{d}s} - \frac{1}{\cos\theta}\frac{\mathrm{d}\tilde{\psi}_1}{\mathrm{d}s} - \frac{1}{\cos\theta}\,\frac{\mathrm{d}(q_1 \cos\theta)}{\mathrm{d}s}\,\tilde{\eta}, \tag{4.33}$$

$$\lambda\tilde{\eta} = -q_2\frac{\mathrm{d}\tilde{\eta}}{\mathrm{d}s} - \frac{1}{\cos\theta}\frac{\mathrm{d}\tilde{\psi}_2}{\mathrm{d}s} - \frac{1}{\cos\theta}\,\frac{\mathrm{d}(q_2 \cos\theta)}{\mathrm{d}s}\,\tilde{\eta}. \tag{4.34}$$

By similar reasoning as before, the unstable eigenfunctions must be localized and so we can apply Cauchy's theorem to $\tilde{\phi}_1 + \mathrm{i}\tilde{\psi}_1$ as was done in the free-surface problem to yield the Hilbert-transform pair:

$$\tilde{\psi}_1 = \frac{1}{\pi}\int_{-\infty}^{\infty} \frac{\tilde{\phi}_1(s)}{s - \Phi}\mathrm{d}s = \mathcal{H}(\tilde{\phi}_1) \qquad (\Psi = 0), \tag{4.35}$$

where $\Phi \equiv \Phi_1$.

A relationship between $\tilde{\psi}_2$ and $\tilde{\phi}_2$ can be obtained in a manner similar to that used to obtain (4.29) using an image system and the properties

$$\tilde{\phi}_2(\Phi_2, \Psi_2 = 0) = -\tilde{\phi}_2(\Phi_2, \Psi_2 = 2), \qquad \tilde{\psi}_2(\Phi_2, \Psi_2 = 0) = -\tilde{\psi}_2(\Phi_2, \Psi_2 = 2).$$

Using Φ as an independent variable, the integral relation reads

$$\tilde{\psi}_2 + \frac{2}{\pi}\int_{-\infty}^{\infty} \frac{\tilde{\psi}_2\, g_\xi}{[g(\xi) - g(\Phi)]^2 + 4}\mathrm{d}\xi = -\frac{1}{\pi}\int_{-\infty}^{\infty} \frac{\tilde{\phi}_2\, g_\xi}{g(\xi) - g(\Phi)}\mathrm{d}\xi + \frac{1}{\pi}\int_{-\infty}^{\infty} \frac{[g(\xi) - g(\Phi)]\, \tilde{\phi}_2\, g_\xi}{[g(\xi) - g(\Phi)]^2 + 4}\mathrm{d}\xi. \tag{4.36}$$

Making the change d /d$s = q_1$ d /dΦ where $q \equiv q_1$, the eigenvalue problem (4.32–4.34) then takes the final form

$$\lambda(\tilde{\phi}_1 - R\tilde{\phi}_2) = -q^2\, \frac{\mathrm{d}\tilde{\phi}_1}{\mathrm{d}\Phi} + Rg'q^2\, \frac{\mathrm{d}\tilde{\phi}_2}{\mathrm{d}\Phi} - \left(q^2\, \frac{\mathrm{d}(q \sin\theta)}{\mathrm{d}\Phi} - Rg'q^2\, \frac{\mathrm{d}(g'q\sin\theta)}{\mathrm{d}\Phi} + \frac{(1-R)}{F^2}\right)\tilde{\eta}$$
$$+ \frac{q}{\cos\theta}\frac{\mathrm{d}}{\mathrm{d}\Phi}\left(q\cos^2\theta\frac{\mathrm{d}\tilde{\eta}}{\mathrm{d}\Phi}\right), \tag{4.37}$$

$$\lambda\tilde{\eta} = -q^2\frac{\mathrm{d}\tilde{\eta}}{\mathrm{d}\Phi} - \frac{q}{\cos\theta}\,\frac{\mathrm{d}\mathcal{H}(\tilde{\phi}_1)}{\mathrm{d}\Phi} - \frac{q}{\cos\theta}\,\frac{\mathrm{d}(q\cos\theta)}{\mathrm{d}\Phi}\,\tilde{\eta}, \tag{4.38}$$

$$\lambda\tilde{\eta} = -q^2 g'\frac{\mathrm{d}\tilde{\eta}}{\mathrm{d}\Phi} - \frac{q}{\cos\theta}\,\frac{\mathrm{d}\mathcal{G}(\tilde{\phi}_2)}{\mathrm{d}\Phi} - \frac{q}{\cos\theta}\,\frac{\mathrm{d}(q\cos\theta)}{\mathrm{d}\Phi}\,\tilde{\eta}, \tag{4.39}$$

where $\tilde{\eta}$, $\tilde{\phi}_1$ and $\tilde{\phi}_2$ decay to zero as $|\Phi| \to \infty$. The operator $\mathcal{G}$ represents the linear integral operator in (4.36), i.e., $\tilde{\psi}_2 = \mathcal{G}(\tilde{\phi}_2)$.

4.5.2 Numerical results

After discretizing this problem in a manner similar to the steady problem, we obtain a generalized eigenvalue problem

$$[C]\mathbf{x} = \lambda[B]\mathbf{x}.$$

For most computations, the inverse power method was used to track growth rates as parameters were varied starting with growth rates in the free-surface problem (Appendix C). In some cases, a modified QR algorithm with shifting was used to find a few eigenvalues scanning a reasonable growth rate range to detect instabilities.

Starting with the known growth rate of elevation waves at a surface steepness of 8.5 degrees, the density ratio was increased and a new growth rate was found by adjusting F^2 so as to maintain the same maximum surface steepness and thereby maintain roughly the same distance to the bifurcation point where the eigenvalue is always zero. For depression waves, an instability was first detected at $R = 0.2$; the growth rate was then monitored as the density ratio was decreased holding the maximum steepness at 7.7 degrees. The resulting growth rates of elevation and depression waves as R is varied are shown in Figure 4–9. Extrapolating the data, it appears that an exchange of stability occurs at about $R = 0.063$. For R less than this value, no instability could be detected for depression waves, while for R greater than this value no instability could be detected for elevation waves. As can be seen in the figure, as R increases the instability of the depression branch increases to substantial values even at the low surface steepnesses considered.

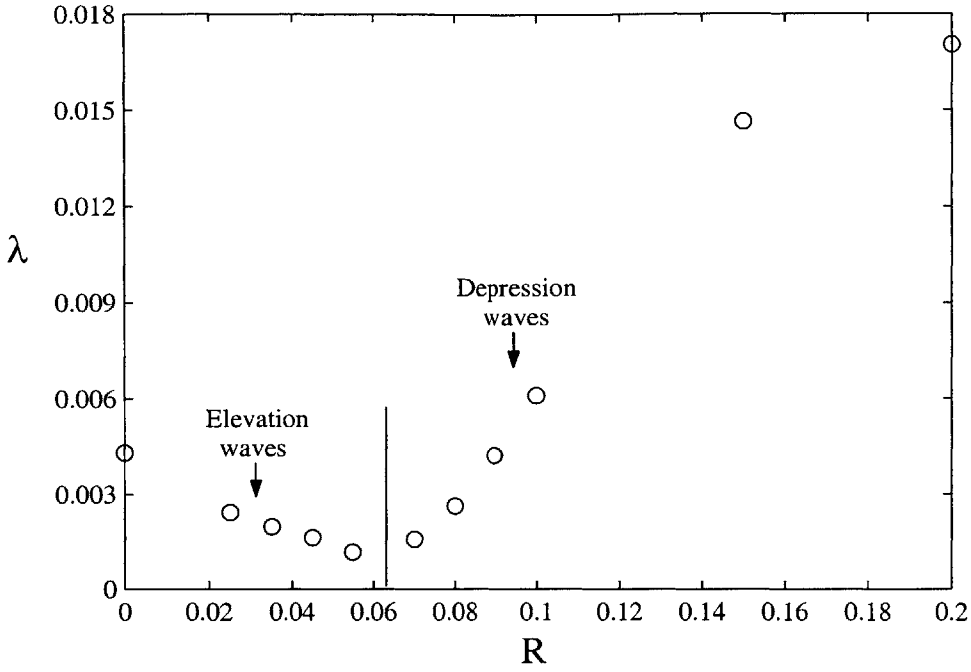

FIGURE 4–9. Instability growth rates λ of elevation and depression solitary waves near the bifurcation point as R is varied. For $R < 0.063$ depression waves are stable, while for $R > 0.063$ elevation waves are stable.

4.6 Discussion

For typical values of h, c, ρ_1/ρ_2, and T which result in values of $W \approx 1$ it appears that stable interfacial gravity–capillary solitary waves are of the elevation type, with high central crests and decaying oscillations in their tails. This stable profile appears to exist over much of the range of R between zero and one since an exchange of stability for small-amplitude elevation waves in the free-surface problem appears to occur at low density ratios. This appears to be the case, however, when a finite upper fluid is present. For two deep fluids, the growth rate does appear to be decrease as the density of the upper fluid increases from zero; the solution diagrams in the deep fluids case, however, differs dramatically from the case of a finite upper layer (see Laget & Dias 1997).

The dynamic picture given by time-dependent solutions of the Benjamin equation appears to suggest that elevation waves are stable to even large disturbances and appear to arise from general localized conditions. Moreover, because of the good agreement between large-amplitude solitary wave profiles computed using the Benjamin equation and the profiles computed using the full hydrodynamic equations, it is expected that the dynamical picture given by the time-dependent solutions might persist even when system conditions do not corresponds to the ideal Benjamin situation. This is particularly significant if experimental observations are attempted since, as was pointed out by Albert *et al.* (1999), it may be difficult to satisfy (4.5) with common fluids without using a small value of h. This would in turn increase the importance of viscous effects which is undesirable. According to the results presented here, it may be possible to satisfy (4.5) approximately and still obtain an experimental range where solitons might exist.

CHAPTER 5

RADIATING GRAVITY–CAPILLARY ENVELOPE SOLITONS

5.1 Introduction

In the small-amplitude limit, gravity–capillary solitary waves belonging to the new class may be interpreted as wavepackets with equal phase and group speeds; a condition attained when the carrier wavenumber corresponds to the minimum value of the linear phase speed. Under this condition, it may be shown that the envelope of the solitary wave is locally confined provided that enough accuracy is used in an asymptotic analysis and certain phase restrictions are accounted for (Yang & Akylas 1997). In this chapter, a more general situation will be considered in which the solitary wave speed lies above the minimum value of the linear phase speed where the phase and group speeds are unequal. In this situation, solitary waves are unsteady and are more precisely described as envelope solitons. Because of a resonance mechanism that is beyond the narrow-band approximation used to derive the nonlinear Schrödinger (NLS) equation and its higher-order counterparts, it will be shown that envelope solitons are generally nonlocal: oscillatory tails of non-decaying amplitude accompany the main wavepacket core. Although the amplitude of these tails is formally exponentially small, the tail amplitude turns out to be considerable when the steepness of the envelope soliton is large.

In deriving the NLS equation for the envelope of a narrow-band small-amplitude wave pulse, only the dominant nonlinear and dispersive effects are included. This approximation is bound to fail eventually, however, when higher-order effects come into play after a number of cycles depending on the steepness and the duration of the pulse. For example, according to laboratory observations of deep-water gravity waves in a tank, an initially symmetric pulse with uniform frequency becomes asymmetric after propagating for some distance along the tank (Su 1982), whereas the same pulse would remain symmetric based on the

NLS equation. This discrepancy can be explained theoretically by a more accurate envelope equation than the NLS that includes certain nonlinear modulation terms (Lo & Mei 1985, Akylas 1989), and the same theoretical approach has also been used to study higher-order effects in optical solitons (Hasegawa 1989).

In contrast to these prior studies, here we wish to explore a phenomenon that cannot be discussed within the narrow-band approximation, namely the radiation of tails by NLS solitary wave pulses. As it turns out, these tails comprise wavenumbers that, in general, are not sidebands of the carrier wavenumber so they cannot be properly described using an evolution equation for the wave envelope.

The first indication that NLS solitons may radiate tails was revealed by a numerical study of a modified NLS equation with a third-order-derivative dispersive term (Wai *et al.* 1986); this third-order NLS equation replaces the standard NLS in the vicinity of caustics (Akylas & Kung 1990), such as the zero-dispersion wavelength in optical fibers. Using an NLS soliton as initial condition, radiation manifests itself as small-amplitude periodic waves travelling with the same phase speed as the solitary-wave main core. Consequently, NLS envelope solitons become nonlocal — they develop oscillatory tails of non-vanishing amplitude — near caustics (Klauder *et al.* 1993, Calvo & Akylas 1997), and solitary waves of the KdV type also turn out to be nonlocal in certain instances owing to a similar resonance mechanism (Pomeau *et al.* 1988, Akylas & Grimshaw 1992).

In general, however, when the carrier wavelength of a solitary wave pulse is not close to a caustic, the tails implied by the third-order NLS equation have comparable wavelength to the carrier, violating the slowly-varying-envelope approximation. Therefore, the distinction between the carrier and its envelope is blurred at the tails of the pulse and one has to use the full governing equation rather than an envelope equation to investigate the form of the disturbance there. For this purpose, we shall work with the fifth-order KdV equation as a simple example of a dispersive wave system that supports solitary pulses of the NLS type.

On the basis of a purely kinematic argument, it is deduced that the wavenumbers that partake in the tails satisfy certain resonance conditions that depend on the dispersion relation of the problem at hand. Hence, given the carrier wavenumber, these resonant wavenumbers can be readily determined, suggesting that solitary pulses radiate tails in general. The tail amplitude cannot be found so easily, however, as it turns out to be exponentially small with respect to the steepness of the main pulse. To calculate the tail amplitude asymptotically, it is necessary to carry beyond all orders the usual multi-scale expansion underlying the NLS equation, and details are worked out here for solitary pulses governed by the fifth-order KdV equation.

Despite the fact that the tail amplitude is exponentially small in the asymptotic sense, numerical simulations of the long-time evolution of solitary pulses of the fifth-order KdV equation indicate that the radiated tails often form a significant part of the overall signal, causing considerable distortion of the main pulse. This suggests that radiation could be an important issue when dealing with solitary pulses of relatively short duration.

5.2 Wave pulses with solitary envelopes

In describing a wave pulse with an envelope of permanent form, rather than the space and time variables x and t, it is convenient to use the two phases

$$\theta = k_0(x - ct), \qquad \xi = \epsilon(x - Ct) \tag{5.1}$$

which move with the carrier and its envelope, respectively, c and C being their corresponding speeds. Also, to bring out the fact that the envelope is varying slowly relative to the carrier, ξ has been scaled with $0 < \epsilon \ll 1$, the ratio of the carrier wavelength $2\pi/k_0$ to a characteristic lengthscale of the envelope.

In terms of θ and ξ, then, a solitary wave pulse

$$u(x,t) = U(\theta, \xi;\ \epsilon) \tag{5.2}$$

is such that U is 2π-periodic in θ and locally confined in ξ:

$$U \to 0 \qquad (|\xi| \to \infty) \ . \tag{5.3}$$

Generally, the wave profile U satisfies a nonlinear partial differential equation, however, and is analytically intractable. In the small-amplitude limit, on the other hand, the standard solution procedure is to expand U

$$U = \epsilon \left\{ A(\xi)\, \mathrm{e}^{\mathrm{i}\theta} + \text{c.c.} \right\} + \epsilon^2 A_0(\xi) + \epsilon^2 \left\{ A_2(\xi)\, \mathrm{e}^{2\mathrm{i}\theta} + \text{c.c.} \right\} + \cdots \ , \tag{5.4}$$

as well as

$$c = c_0 + \epsilon^2 c_2 + \cdots , \tag{5.5a}$$

$$C = c_g|_0 + \epsilon^2 C_2 + \cdots , \tag{5.5b}$$

here, consistent with the linear theory, $c_0 = \omega_0/k_0$ denotes the linear phase speed at the carrier wavenumber k_0 and $c_g|_0 = d\omega/dk|_0$ the corresponding group speed as obtained from the linear dispersion relation $\omega = \omega(k)$.

Upon substitution of these expansions into the equation governing U, the fact that the higher harmonics in the Fourier series (5.4) are of progressively smaller amplitude allows one to solve for $A_0, A_2, \ldots$ in terms of A, the envelope of the primary harmonic which turns out to satisfy an evolution equation of the NLS type. Solitary wave pulses, consistent with the condition (5.3) that they remain locally confined, then correspond to solutions of this evolution equation such that

$$A \to 0 \qquad (|\xi| \to \infty) \ . \tag{5.6}$$

Although it is straightforward, the perturbation procedure outlined above typically involves a considerable amount of algebra. In the interest of brevity, here we shall work with a relatively simple example of a dispersive wave system, namely the fifth-order KdV equation in the normalized form

$$u_t + 6uu_x + u_{xxx} + u_{xxxxx} = 0 \ . \tag{5.7}$$

In this case, the linear dispersion relation is

$$\omega(k) = -k^3 + k^5 \ , \tag{5.8}$$

and the details of deriving the evolution equation governing A have already been worked out in Grimshaw *et al.* (1994). Specifically,

$$A_0 = 6 \, \frac{|A|^2}{c_g|_0} + O(\epsilon^2) \ , \tag{5.9a}$$

$$A_2 = \frac{A^2}{k_0^2(1-5k_0^2)} + 2\mathrm{i}\epsilon \, \frac{1-10k_0^2}{k_0^3(1-5k_0^2)^2} \, AA_\xi + O(\epsilon^2) \ , \tag{5.9b}$$

and A satisfies the evolution equation

$$-k_0c_2A + \mu A^2A^* + \lambda A_{\xi\xi} + \mathrm{i}\epsilon \left[\gamma A_{\xi\xi\xi} + C_2A_\xi - \frac{\mu}{k_0}(A^2A^*)_\xi + \nu|A|^2A_\xi \right] = O(\epsilon^2) \ , \tag{5.10}$$

where

$$\mu = \frac{6}{k_0} \, \frac{3-25k_0^2}{(1-5k_0^2)(5k_0^2-3)} \ , \qquad \lambda = k_0(3-10k_0^2) \ ,$$

$$\gamma = 10k_0^2 - 1 \ , \qquad \nu = \frac{12}{k_0^2} \, \frac{1-10k_0^2}{(1-5k_0^2)^2} \ .$$

In looking for solitary-wave solutions, it is convenient to introduce the polar form

$$A = S(\xi) \, \mathrm{e}^{\mathrm{i}\phi(\xi)} \ . \tag{5.11}$$

Upon substitution into (5.10), it is found that S and ϕ satisfy

$$\lambda S'' - k_0c_2S + \mu S^3 = O(\epsilon^2) \ , \tag{5.12a}$$

$$\phi' = -\frac{\epsilon}{\lambda} \left\{ \gamma \left[\frac{S''}{S} - \tfrac{1}{2} \left(\frac{S'}{S} \right)^2 \right] + \tfrac{1}{2} \, C_2 + \tfrac{1}{4} \left(\nu - \frac{3\mu}{k_0} \right) S^2 \right\} + O(\epsilon^2) \ . \tag{5.12b}$$

Hence, locally confined solutions for S consistent with (5.6) can be obtained only when $\lambda\mu > 0$ which occurs in the ranges $\sqrt{3/25} < k_0 < \sqrt{1/5}$ and $\sqrt{3/10} < k_0 < \sqrt{3/5}$. Taking k_0 so that this condition is met and normalizing the peak amplitude of the primary harmonic in (5.4) to be equal to ϵ, the appropriate solution of (5.12a) is

$$S = \tfrac{1}{2} \operatorname{sech} \beta\xi + O(\epsilon^2) \ , \tag{5.13}$$

where

$$\beta = \tfrac{1}{2}\left(\frac{\mu}{2\lambda}\right)^{1/2} , \qquad c_2 = \frac{\mu}{8k_0} \; .$$

Having determined S, the phase $\phi(\xi)$ can be found from (5.12b). Before doing so, however, to avoid secular terms in expansion (5.4), we fix the carrier wavenumber to be equal to k_0 at the tails of the pulse:

$$\phi' \to 0 \qquad (|\xi| \to \infty) \; ;$$

making use of (5.13) and (5.12b), this condition then specifies C_2:

$$C_2 = -\frac{\gamma\mu}{8\lambda} \, ,$$

and $\phi(\xi)$ is given by

$$\phi = \phi_0 + \epsilon \, \frac{\sigma}{\beta\lambda} \tanh \beta\xi + O(\epsilon^2) \; , \tag{5.14}$$

ϕ_0 being an arbitrary phase constant and

$$\sigma = \tfrac{3}{2}\,\gamma\beta^2 - \tfrac{1}{16}\left(\nu - \frac{3\mu}{k_0}\right) \; .$$

Finally, combining (5.4), (5.9), (5.11), (5.13) and (5.14), the following expression, correct to $O(\epsilon^2)$, for a solitary wave pulse is found

$$\begin{aligned} U \;\; = \;\; & \epsilon \,\mathrm{sech}\, \beta\xi \cos(\theta + \phi_0) + \epsilon^2 \Bigg\{ -\frac{\sigma}{\beta\lambda} \,\mathrm{sech}\, \beta\xi \tanh \beta\xi \sin(\theta + \phi_0) \\ & + \mathrm{sech}^2\, \beta\xi \left[\frac{3}{2c_g|_0} + \frac{\cos(2\theta + 2\phi_0)}{2k_0^2(1 - 5k_0^2)} \right] \Bigg\} + \cdots \; . \end{aligned} \tag{5.15}$$

While the expansion procedure outlined above can be carried to higher order with no apparent difficulty, previous experience indicates that it may still not be justified to conclude that the fifth-order KdV equation admits solutions in the form of locally confined solitary pulses: solitary waves that are seemingly locally confined based on approximate theories may in fact feature tails that do not decay at infinity (Akylas & Grimshaw 1992, Yang &

Akylas 1996); the amplitudes of these tails happen to be exponentially small with respect to that of the main solitary-wave core and cannot be captured by standard perturbation expansions in powers of ϵ, like the expansion (5.4) used here.

Of course, for such tails to appear, it is necessary that they are kinematically compatible with the main solitary-wave core. In the case of nonlocal solitary waves of the KdV type, for example, the tail wavenumber is such that the corresponding phase speed matches the speed of the main disturbance. But in the present situation where the main pulse cannot be made steady — the carrier and its envelope move at different speeds — this resonance condition is not appropriate. Accordingly, before revising our perturbation procedure to account for possible exponentially small terms, we shall derive, based on a kinematic argument, the conditions that determine whether tails can accompany a solitary pulse in the present setting.

5.3 Resonance conditions

For the purpose of understanding the generation of tails intuitively, it is helpful to think of the main solitary pulse as a known forcing disturbance; out of all possible waves that this disturbance can excite, only those that are forced resonantly and would appear in the steady-state response can form tails.

More specifically, according to expansion (5.4), a solitary pulse may be written as

$$U = \epsilon \sum_{n=-\infty}^{\infty} U_n(\xi;\, \epsilon)\, \mathrm{e}^{in\theta} \tag{5.16}$$

with $U_{-n} = U_n^*$. In this Fourier series, all harmonics other than the primary ($n = 1$) have carriers that, in general, do not satisfy the dispersion relation (5.8),

$$\omega(nk_0) \neq nk_0 c \qquad (n \neq 1)\ , \tag{5.17}$$

and, hence, are not resonant.

To see how resonance may arise, we decompose the envelope of each harmonic into Fourier components by taking its Fourier transform with respect to ξ:

$$\widehat{U}_n(K;\, \epsilon) = \frac{1}{2\pi} \int_{-\infty}^{\infty} U_n(\xi;\, \epsilon)\, \mathrm{e}^{-\mathrm{i}K\xi}\, \mathrm{d}\xi \ ;$$

combining then each of these Fourier components with the corresponding carrier in (5.16) using (5.1), U is seen to comprise terms of the form

$$\widehat{U}_n(K;\, \epsilon)\ \exp\{\mathrm{i}\,[(nk_0 + \epsilon K)\, x - (nk_0 c + \epsilon KC)\, t]\} \ . \tag{5.18}$$

From this expression, it is now clear that resonance is possible if for some wavenumber(s) $K = K_*$, say, the following condition is met

$$\omega_* = \omega(k_*) \ , \tag{5.19a}$$

where

$$k_* = nk_0 + \epsilon K_* \ , \qquad \omega_* = nk_0 c + \epsilon K_* C \ . \tag{5.19b}$$

For a given carrier wavenumber k_0 and each harmonic n, condition (5.19a) provides an equation to determine ϵK_*; the wavenumber k_* and frequency ω_* of the tail corresponding to each real solution of this equation are then given by (5.19b). For $n = 0$, in particular, the mean harmonic in (5.16) is a long-wave disturbance moving with speed C and (5.19a,b) imply that the tail wavenumber k_* is such that the phase speed of the tail matches C, consistent with the resonance condition that applies to the tails of solitary waves of the KdV type.

The values of the resonant wavenumbers k_* that partake in the tails of a solitary wave pulse depend on the linear dispersion relation of the particular problem at hand and can be computed numerically as will be discussed in the next section for the fifth-order KdV equation. From (5.19), however, it is clear that, in general, the tail wavenumbers are not sidebands of the carrier wavenumber k_0 so the tails cannot be described by an evolution equation, like (5.10), for the envelope of the primary harmonic.

Moreover, in view of (5.17), conditions (5.19) indicate that generally $\epsilon K_* = O(1)$; hence, the tail amplitude, being proportional to $|\widehat{U}_n(K_*; \epsilon)|$ according to (5.18), is expected to be exponentially small with respect to ϵ — the Fourier transform of a smooth function decays exponentially as $|K| \to \infty$. This, in fact, suggests a criterion for determining the asymptotically dominant contribution to the tails: out of all k_* that satisfy the resonance conditions (5.19), the one corresponding to the smallest value of $|K_*|$ gives the tail with the relatively largest amplitude. On the other hand, to obtain a precise asymptotic expression for the tail amplitude as $\epsilon \to 0$ is not a straightforward matter and requires techniques of exponential asymptotics (see Section 5.5).

Before proceeding with the asymptotic analysis, we turn to numerical simulations of the evolution of solitary wave pulses of the fifth-order KdV equation, in an effort to confirm the resonance conditions (5.19) and to gain further insight into the generation of tails.

5.4 Numerical evidence

We shall solve the fifth-order KdV equation (5.7) numerically using as initial condition expansion (5.15) correct to $O(\epsilon^2)$ which includes only the fundamental, mean and second harmonics ($n = 1, 0, 2$ respectively) in the Fourier series representation (5.16) of a solitary wave pulse. Thus, attention is focussed on the generation of tails by resonances associated with these three harmonics.

The numerical scheme used in integrating the fifth-order KdV equation is the split-step Fourier method (see Appendix A). To accommodate radiated waves, the computational domain was expanded once a threshold value near the boundaries was reached. For most of the computations the step sizes $\Delta t = 0.0087$, $\Delta x = 0.6$ were used; it was verified that increasing this resolution did not change the results significantly. Also, as a further check, the conservation law

$$\frac{\partial}{\partial t} \int_{-\infty}^{\infty} u^2 \, \mathrm{d}x = 0$$

was satisfied within 0.5%.

As a preliminary step, it is straightforward to find the values of the tail wavenumbers $k_*^{(n)}$ $(n = 1, 0, 2)$ predicted by the resonance conditions (5.19). Using the dispersion relation (5.8), it follows that they are the real roots of the polynomial

$$k_*^5 - k_*^3 - Ck_* + nk_0(C - c) = 0 \ , \tag{5.20}$$

where c and C are given by (5.5). Also, based on the resonance mechanism proposed earlier, the wave with the largest amplitude at the tails is induced by the harmonic n which yields the smallest value of envelope wavenumber $|K_*^{(n)}|$. The wavenumber $k_*^{(n)}$ that, according to this criterion, makes the dominant contribution to the tails is plotted in Figure 5–1 as a function of the carrier wavenumber k_0 (using the lowest-order approximations $c \approx c_0$, $C \approx c_g|_0$).

In interpreting the results of the numerical simulations against the quasi-steady state envisaged in deriving the resonance conditions (5.19), the group speed, being the energy-transport speed, plays an important part. Specifically, the front associated with each resonant wavenumber $k_*^{(n)}$ is expected to propagate with speed $c_g(k_*^{(n)}) - C$ relative to the main pulse. As a result, it is possible for a resonant wavenumber having a relatively large value of $|c_g(k_*^{(n)}) - C|$ to generate a tail faster, and be more apparent during the early stages of the pulse evolution, than the asymptotically dominant wavenumber which ultimately contributes the tail with the largest amplitude. Also, since the main pulse has finite energy, the radiation of tails will eventually lead to some loss of form of the wavepacket envelope, this effect being more pronounced as the wave steepness ϵ is increased.

We begin by considering the evolution of a pulse with carrier wavenumber $k_0 = 0.4$ and steepness $\epsilon = 0.01$. In this instance, the dominant resonant wavenumber according to the theory is provided by the second harmonic $n = 2$ (see Figure 5–1) and, from (5.19), $k_*^{(2)} = 0.8971$.

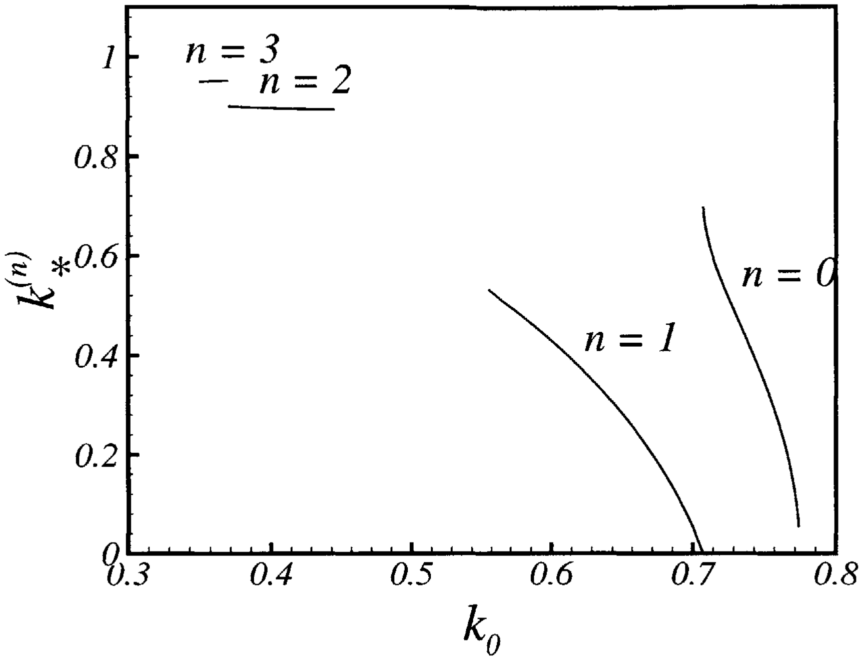

FIGURE 5–1. Dominant resonant wavenumbers $k_*^{(n)}$ plotted as a function of carrier wavenumber k_0 over the two intervals $\sqrt{3/25} < k_0 < \sqrt{1/5}$ and $\sqrt{3/10} < k_0 < \sqrt{3/5}$ where the NLS equation associated with the fifth-order KdV equation accepts locally confined envelope soliton solutions.

Also since $c_g(k_*^{(2)}) = 0.82 > 0$ and $c_g(k_0) = -0.35 < 0$, one expects radiation to be emitted towards the positive x-direction, opposite to the propagation direction of the main pulse. Figure 5–2 shows snapshots of the pulse at $t = 0$, $t = 500$ and $t = 750$ along with the corresponding spectra in the wavenumber domain. The initial profile (Figure 5–2a) is in the form of a packet with approximately 18 cycles within the envelope and, as expected, its spectrum comprises three peaks associated with the fundamental, mean and second harmonics. At $t = 500$ (Figure 5–2b), however, a front has developed ahead of the pulse in physical space and a peak is apparent in wavenumber space at $k \approx 0.9$, very close to the theoretically predicted resonant wavenumber $k_*^{(2)}$. At the later time instant $t = 750$ (Figure 5–2c), this peak is even sharper and its attendant radiation more pronounced, with nearly uniform amplitude away from the front. As a second example, we discuss a pulse with $k_0 = 0.6$ and $\epsilon = 0.02$. For this carrier wavenumber, conditions (5.19) predict that the dominant resonant wavenumber (corresponding to the smallest value of $|K_*|$) is

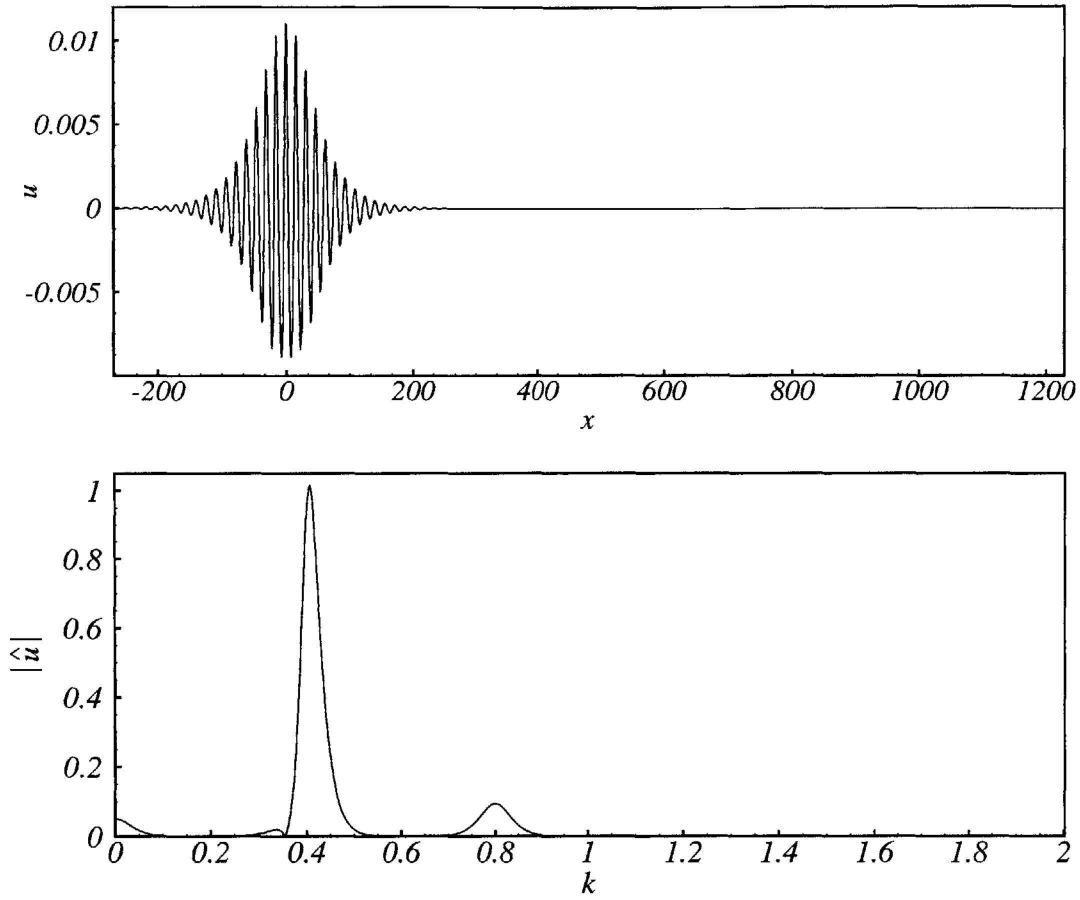

FIGURE 5–2(A). Pulse evolution shown at the instants (a) t = 0, (b) t = 500 and (c) t = 750. Expression (15) is used as the initial condition with parameters $k_0 = 0.4$, $\epsilon = 0.01$, and ϕ_0=0. The pulse is displayed in both physical (top portion) and wavenumber (bottom portion) spaces. The origin of x has been chosen to coincide with the pulse center. The magnitude of the spectral amplitude $|\hat{u}|$ is computed by a base-2 FFT routine using N = 4096 pints.

$k_*^{(1)} = 0.4410$ for $n = 1$, while the next dominant one (corresponding to the second smallest value of $|K_*|$) is $k_*^{(2)} = 0.8939$ for $n = 2$. A snapshot of the pulse at $t = 1100$ and the corresponding spectrum are shown in Figure 5–3. Although a peak is seen in the wavenumber domain at $k \approx 0.37$ in rough agreement with $k_*^{(1)}$, the most striking feature is the dominance of the peak at $k \approx 0.88$ which is close to $k_*^{(2)}$. Note, however, that $c_g(k_*^{(1)}) - c_g(k_0) = 0.038$ while $c_g(k_*^{(2)}) - c_g(k_0) = 1.23$. Hence, the $n = 1$ front is very slow and naturally it takes a long time for the corresponding tail to develop relative to the

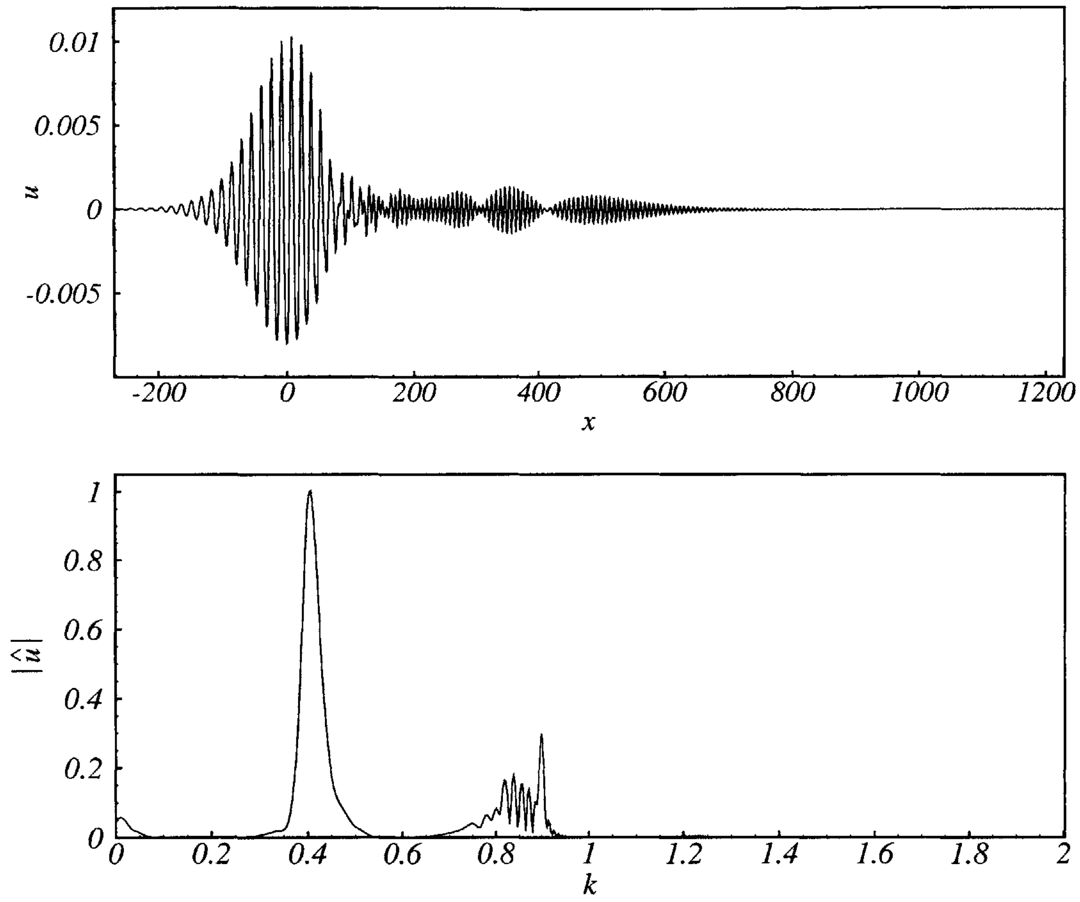

FIGURE 5–2(B). t = 500

$n = 2$ front. Also, as these front speeds are positive, both radiated tails appear ahead of the main pulse, leading to the complicated pattern seen in Figure 5–3. Finally, we wish to explore a case in which the $n = 0$ harmonic in the initial condition furnishes the dominant resonant wavenumber. For $n = 0$, equation (5.20) in fact reduces to a biquadratic and real roots corresponding to propagating waves can be found only when $1/\sqrt{2} < k_0 < \sqrt{3/5}$. Accordingly, we consider a pulse with carrier wavenumber $k_0 = 0.75$ and steepness $\epsilon = 0.025$. For this choice, it turns out that $n = 0$ yields both the dominant resonant wavenumber $k_{*1}^{(0)} = 0.4347$ and the next dominant one $k_{*2}^{(0)} = 0.9006$ according to the resonance conditions (5.19).

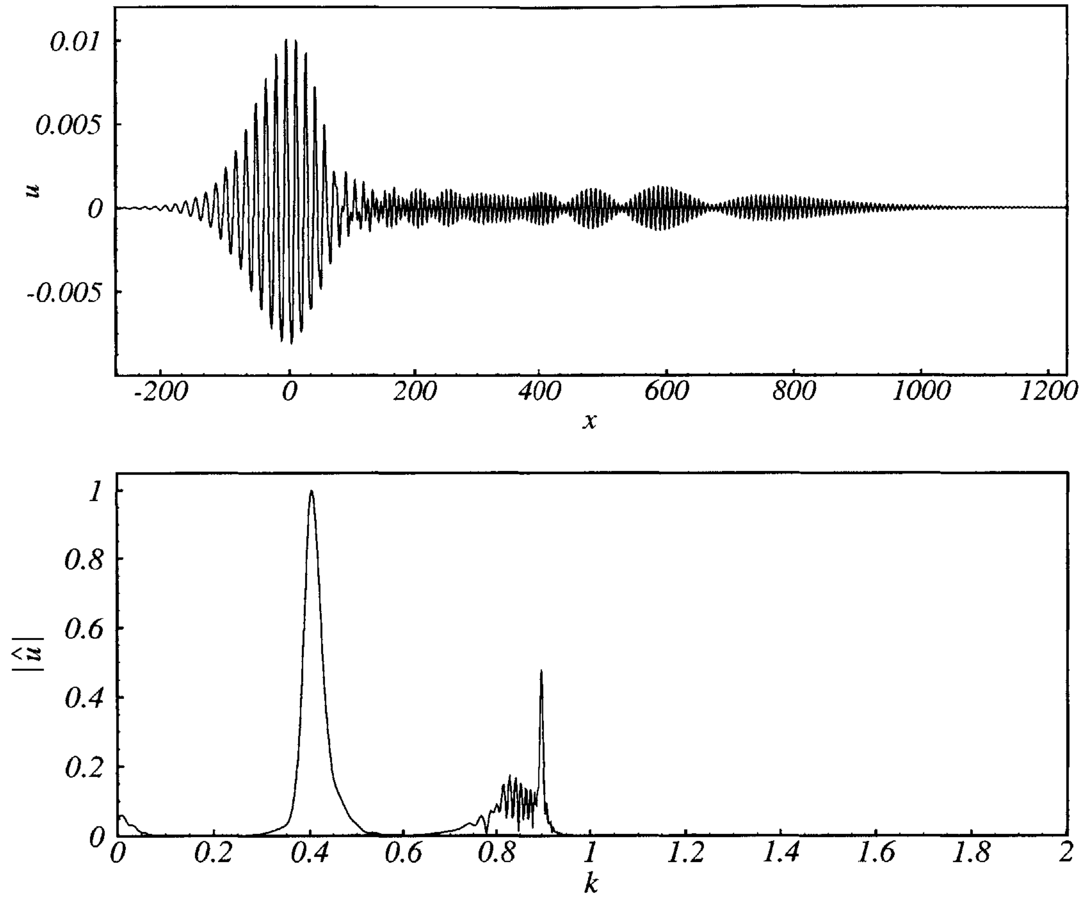

FIGURE 5–2(C). t = 750

These predictions are confirmed by the results of the numerical simulation at $t = 750$ shown in Figure 5–4: there are sharp peaks in the wavenumber domain at $k \approx 0.44$ and at $k \approx 0.9$, in excellent agreement with the theory. Moreover, the radiated tail with the longer wavelength is found behind the main pulse (since $c_g(k_{*1}^{(0)}) < c_g(k_0)$) and has larger amplitude than the other tail which appears ahead of the main pulse (since $c_g(k_{*2}^{(0)}) > c_g(k_0)$). The numerical results presented thus far certainly support the resonance mechanism proposed earlier; the radiated tails comprise wavenumbers in agreement with those predicted by the resonance conditions (5.19). More detailed comparisons between analytical and numerical results will be made later, after obtaining an asymptotic expression for the tail amplitude

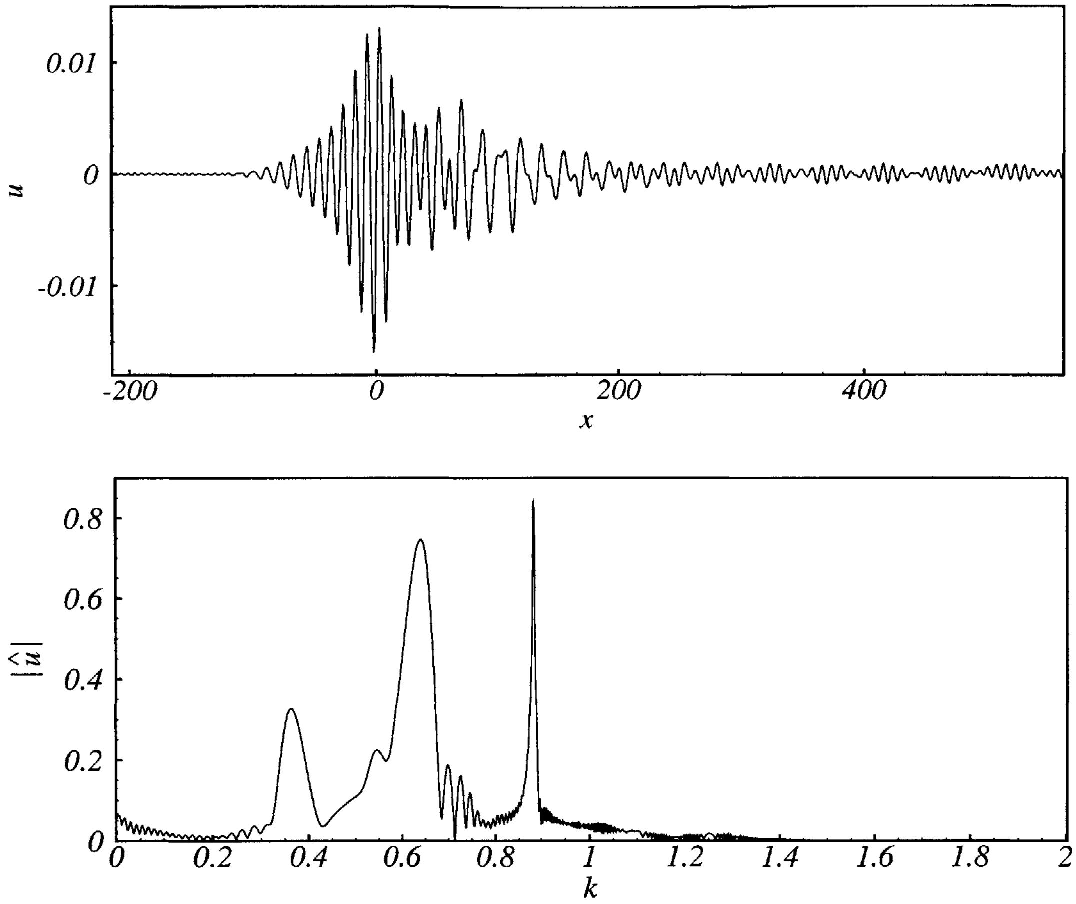

FIGURE 5–3. Snapshot of pulse evolution at $t = 1100$ for the conditions $k_0 = 0.6$, $\epsilon = 0.02$ and $N = 8192$.

in the weakly nonlinear regime $\epsilon \ll 1$.

5.5 Tail amplitude

On the basis of a heuristic argument, it was deduced in Section 5.3 that the tails emitted by a small-amplitude solitary wave pulse have exponentially small amplitude with respect to ϵ. This suggests that, in order to capture these tails, it is necessary to carry expansion (5.20) beyond all orders in ϵ using techniques of exponential asymptotics. The procedure for calculating the tail amplitude asymptotically closely parallels that followed in a previous

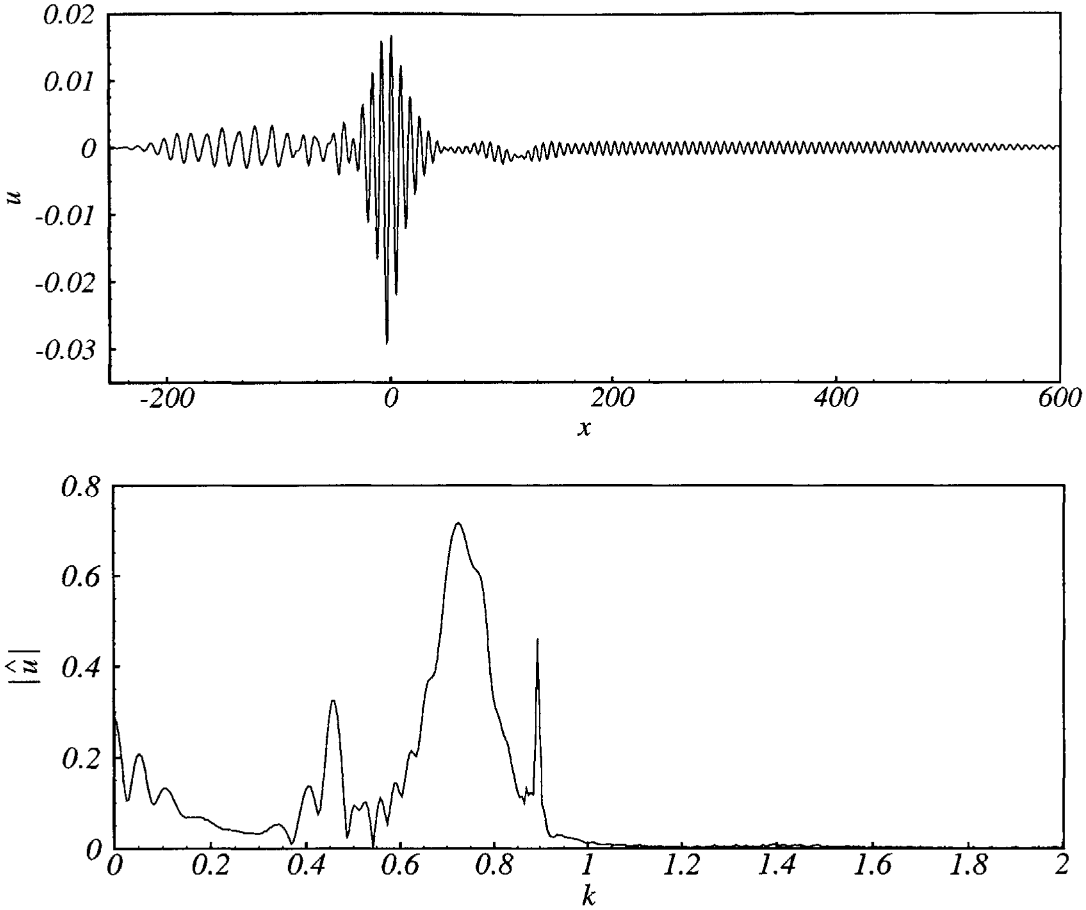

FIGURE 5–4. Snapshot of pulse evolution at $t = 750$ for the conditions $k_0 = 0.75$, $\epsilon = 0.025$ and $N = 2048$.

study (Yang & Akylas 1997) of steady solitary-wave solutions of the fifth-order KdV equation in the vicinity of the special carrier wavenumber $k_0 = 1/\sqrt{2}$ where the phase speed c_0 matches the group speed $c_g|_0$.

Here, this asymptotic procedure also provides formal justification of the resonance conditions (5.19) that determine the tail wavenumbers.

The fact that a solitary pulse is accompanied by tails in physical space implies the presence of pole singularities on the real axis at the tail wavenumbers in the wavenumber domain, and the goal is to compute the corresponding residues which determine the tail amplitudes. To this end, it is convenient to work in the wavenumber domain.

We begin by returning to expansion (5.15) for $U(\theta, \xi;\, \epsilon)$ and taking its Fourier transform with respect to the envelope variable ξ:

$$\begin{aligned}\widehat{U}(\theta, K;\, \epsilon) &= \epsilon \operatorname{sech} \frac{\pi K}{2\beta} \left\{ \frac{1}{2\beta} \cos(\theta + \phi_0) + \mathrm{i}\, \frac{\sigma}{2\beta^3 \lambda}\, \epsilon K \sin(\theta + \phi_0) \right. \\ &\qquad \left. + \frac{\epsilon K}{2\beta^2} \left[\frac{3}{2c_g|_0} + \frac{\cos(2\theta + 2\phi_0)}{2k_0^2(1 - 5k_0^2)} \right] \coth \frac{\pi K}{2\beta} + \cdots \right\} .\end{aligned}$$

This expansion becomes non-uniform when $\epsilon K = O(1)$ and suggests the uniformly valid two-scale expression

$$\widehat{U} = \epsilon \operatorname{sech} \frac{\pi K}{2\beta}\, \widetilde{U}(\theta, \kappa;\, \epsilon)\ , \tag{5.21}$$

where $\kappa = \epsilon K$ and

$$\begin{aligned}\widetilde{U} &\sim \frac{1}{2\beta} \cos(\theta + \phi_0) + \mathrm{i}\, \frac{\sigma}{2\beta^3 \lambda}\, \kappa \sin(\theta + \phi_0) \\ &\qquad + \frac{|\kappa|}{2\beta^2} \left[\frac{3}{2c_g|_0} + \frac{\cos(2\theta + 2\phi_0)}{2k_0^2(1 - 5k_0^2)} \right] + \cdots \qquad (\kappa \to 0)\ .\end{aligned} \tag{5.22}$$

Next, $\widetilde{U}(\theta, \kappa;\, \epsilon)$, being 2π-periodic in $\widetilde{\theta} = \theta + \phi_0$, may be expanded in a Fourier series

$$\widetilde{U} = \sum_{n=-\infty}^{\infty} \mathcal{A}_n(\kappa;\, \epsilon)\, \mathrm{e}^{\mathrm{i}n\widetilde{\theta}}\ , \tag{5.23}$$

where, from (5.22),

$$\mathcal{A}_0 \sim \frac{3}{4\beta^2 c_g|_0} |\kappa| + \cdots \qquad (\kappa \to 0)\ , \tag{5.24a}$$

$$\mathcal{A}_{\pm 1} \sim \frac{1}{4\beta} \pm \frac{\sigma}{4\beta^3 \lambda} \kappa + \cdots \qquad (\kappa \to 0)\ , \tag{5.24b}$$

$$\mathcal{A}_{\pm 2} \sim \frac{1}{8\beta^2 k_0^2 (1 - 5k_0^2)} |\kappa| + \cdots \qquad (\kappa \to 0)\ . \tag{5.24c}$$

and $\mathcal{A}_n = O(\kappa^{|n|-1})$ for $|n| > 2$.

In view of (5.21) and (5.23), attention is now focussed on the coefficients $\mathcal{A}_n$ and their possible singularities on the real κ-axis. Upon substitution of (5.21) and (5.23) into the fifth-order KdV equation (5.7) after having taken its Fourier transform with respect to ξ, it follows that the $\mathcal{A}_n$ are governed by

$$\begin{aligned}&\{\omega(\kappa + nk_0) - C\kappa - nk_0 c\}\,\mathcal{A}_n \\ &\qquad + 3(\kappa + nk_0)\,\cosh\frac{\pi\kappa}{2\beta\epsilon}\sum_{p=-\infty}^{\infty}\int_{-\infty}^{\infty}\frac{\mathcal{A}_{n-p}(\kappa-\lambda)\,\mathcal{A}_p(\lambda)}{\cosh\dfrac{\pi(\kappa-\lambda)}{2\beta\epsilon}\,\cosh\dfrac{\pi\lambda}{2\beta\epsilon}}\,\mathrm{d}\lambda = 0 \\ &\qquad\qquad (n = 0, \pm 1, \cdots)\ ,\end{aligned} \tag{5.25}$$

$\omega(k)$ denoting the linear dispersion relation (5.8). However, in the limit $\epsilon \to 0$, the main contribution to the convolution integrals above comes from the ranges $0 < \lambda < \kappa$ $(\kappa > 0)$ and $\kappa < \lambda < 0$ $(\kappa < 0)$. Also, since U is real, $\mathcal{A}_{-n}(\kappa) = \mathcal{A}_n(-\kappa)$ on the real κ-axis so it suffices to consider $\mathcal{A}_n$ $(n \geq 0)$ only, and using the leading-order approximations to c and C in (5.5) the equation system (5.25) is replaced by

$$\begin{aligned}&\{\omega(\kappa + nk_0) - c_g|_0\,\kappa - nk_0 c_0\}\,\mathcal{A}_n + 6(\kappa + nk_0)\sum_{p=0}^{n}\operatorname{sgn}\kappa\int_0^{\kappa}\mathcal{A}_p(\lambda)\,\mathcal{A}_{n-p}\,(\kappa-\lambda)\,\mathrm{d}\lambda \\ &\qquad + 12(\kappa + nk_0)\sum_{p=1}^{\infty}\operatorname{sgn}\kappa\int_0^{\kappa}\mathcal{A}_p(-\lambda)\,\mathcal{A}_{n+p}\,(\kappa-\lambda)\,\mathrm{d}\lambda = 0 \qquad (n \geq 0)\ .\end{aligned} \tag{5.26}$$

In spite of the fact that it appears more complicated than the original partial differential equation (5.7), the integral-equation system (5.26) is most suitable for analyzing the singularities of $\mathcal{A}_n(\kappa)$ on the real κ-axis that are of interest here. These singularities are expected to occur at $\kappa = \kappa_*^{(n)}$, say, where the coefficient of $\mathcal{A}_n$ in (5.26) vanishes. Recalling that $\kappa = \epsilon K$, it is clear from (5.8) and (5.19) that this happens at the real roots of the polynomial (5.20) which in turn correspond to the resonant wavenumbers $k_*^{(n)} = \kappa_*^{(n)} + nk_0$

(in the limit $\epsilon \to 0$ so $c \approx c_0$ and $C \approx c_g|_0$). Hence, the formal asymptotic theory is consistent with the resonance conditions obtained earlier on physical grounds.

The next task is to examine the local behavior of $\mathcal{A}_n$ close to each singularity at $\kappa = \kappa_*^{(n)}$ according to the equation system (5.26). Using the asymptotic behavior of $\mathcal{A}_n$ as $\kappa \to 0$ noted in (5.24), dominant balance suggests that

$$\mathcal{A}_n \sim \frac{D_n}{\kappa_*^{(n)} - \kappa} \qquad (\kappa \to \kappa_*^{(n)},\ n > 0)\ , \tag{5.27a}$$

$$\mathcal{A}_0 \sim \frac{D_0}{\kappa_*^{(0)} \mp \kappa} \qquad (\kappa \to \pm\kappa_*^{(0)})\ , \tag{5.27b}$$

where D_n $(n \geq 0)$ are constants to be determined.

To verify these simple-pole singularities and compute the residues D_n, we pose the solution to the system (5.26) in the form of power series as suggested by expansions (5.24):

$$\begin{aligned} \mathcal{A}_0 &= \sum_{p=2}^{\infty} b_{0,p}\,|\kappa|^{p-1}\ , \\ \mathcal{A}_n &= \sum_{p=n}^{\infty} b_{n,p}^{\pm}\,\kappa^{p-1} \qquad (\kappa \gtrless 0, n > 0)\ , \end{aligned}$$

with

$$b_{0,2} = \frac{3}{4\beta^2\, c_g|_0}\ , \qquad b_{1,1}^{\pm} = \frac{1}{4\beta}\ , \qquad b_{1,2}^{\pm} = \frac{\sigma}{4\beta^3\,\lambda}\ ,$$

$$b_{2,2}^{+} = -b_{2,2}^{-} = \frac{1}{8\beta^2\, k_0^2(1 - 5k_0^2)}\ ,$$

etc. Substituting then these series into (5.26), it follows that $b_{0,2p+1} = 0$ while the rest of the coefficients satisfy certain recurrence relations similar in form to those found in Yang (1996) (Appendix F) that can be readily solved, given the carrier wavenumber k_0. Based on the asymptotic behavior of $b_{n,p}$ as $p \to \infty$, one may thus infer the nature of the singularity of $\mathcal{A}_n$ at $\kappa = \kappa_*^{(n)}$ and compute the corresponding residue as well. Implementing this procedure, the presence of simple-pole singularities at $\kappa = \kappa_*^{(2)}$, $\kappa_*^{(1)}$ and $\kappa_*^{(0)}$, respectively,

k_0	n	D_n	$\kappa_*^{(n)}$	β
0.4	2	0.358	0.0965	2.76
0.6	1	−0.128	−0.170	4.66
0.75	0	−0.369	0.346	4.07

TABLE 5–1. Numerically determined residues D_n and parameters appearing in (5.28) for the dominant $n = 0$, 1 and 2 resonances.

was verified for the three choices of $k_0 = 0.4$, 0.6 and 0.75 considered in Section 5.4, and the results are given in Table 5–1.

Combining (5.21) with (5.23) and (5.27), each singularity of $\mathcal{A}_n$ at $\kappa = \kappa_*^{(n)}$ translates into a singularity of $\widehat{U}$ at $K_*^{(n)} = \kappa_*^{(n)}/\epsilon$. Moreover, since $\mathcal{A}_n(\kappa) = \mathcal{A}_{-n}(-\kappa)$ on the real κ-axis, there is an additional simple-pole singularity at $-K_*^{(n)}$. Hence,

$$\widehat{U} \sim \epsilon \frac{D_n}{\kappa_*^{(n)} \mp \epsilon K} \operatorname{sech} \frac{\pi \kappa_*^{(n)}}{2\beta\epsilon} \, \mathrm{e}^{\pm i n\theta} \qquad (K \to \pm\kappa_*^{(n)}/\epsilon, \ n \geq 0) \ . \tag{5.28}$$

Note that all these singularities have exponentially small residues and, upon inverting the Fourier transform, the one that contributes the tail with the relatively largest amplitude corresponds to the smallest value of $|\kappa_*^{(n)}|$, consistent with the heuristic reasoning presented in Section 5–3.

More specifically, inverting the Fourier transform, we write

$$U = \int_{\mathcal{C}} \widehat{U}(\theta, K;\, \epsilon)\, \mathrm{e}^{\mathrm{i}K\xi}\, \mathrm{d}K \ ,$$

and, since $\widehat{U}$ has simple poles on the real K-axis according to (5.28), the contour $\mathcal{C}$ is chosen so as to satisfy causality: $\mathcal{C}$ is indented to pass below (above) $K = \pm\kappa_*^{(n)}/\epsilon$ when $c_g(k_*^{(n)})$ is greater (less) than $c_g(k_0)$, $k_*^{(n)} = \kappa_*^{(n)} + nk_0$ being the tail wavenumber and $\omega_*^{(n)} = c_g|_0\, \kappa_*^{(n)} + nk_0c_0$ the corresponding tail frequency. Hence, the induced tail

$$u \sim 8\pi s\, D_n \exp\left(\frac{-\pi|\kappa_*^{(n)}|}{2\beta\epsilon}\right) \sin\left(k_*^{(n)}x - \omega_*^{(n)}t + n\phi_0\right) \tag{5.29}$$

is found in $\xi > 0$ ($\xi < 0$) when $s > 0$ ($s < 0$) where $s \equiv \operatorname{sgn}\left(c_g(k_*^{(n)}) - c_g(k_0)\right)$. This criterion for determining the position of the tail relative to the main pulse is in line with the results of the numerical simulations in Section 5–4.

5.6 Discussion

Using the fifth-order KdV equation as a simple example, we have presented analytical and numerical evidence that solitary wave pulses of the NLS type are generally accompanied by oscillatory tails owing to a resonance mechanism: each of the harmonics that make up the main pulse, acting as a forcing disturbance, can induce small-amplitude dispersive wave tails of the form (5.29) either ahead or behind of the main pulse. While the resonant wavenumbers that appear in the radiated tails are determined by this essentially linear process, the precise values of the tail amplitudes are controlled by a fully nonlinear mechanism in which all harmonics are coupled.

The radiation of tails, of course, eventually leads to a decay of the main pulse but the asymptotic analysis of Section 5–2 clearly neglects radiation damping. To estimate the time scale over which this approximation is expected to be valid, we recall from basic linear wave theory that the energy flux through an oscillatory tail of constant amplitude is proportional to the square of the tail amplitude. Given that the main pulse has $O(\epsilon)$ energy, conservation then implies that radiation damping becomes important when $t = O(\epsilon \exp(\pi|\kappa_*^{(n)}|/\beta\epsilon))$, where n corresponds to the dominant radiated tail. For times less than this exponentially long time scale, the pulse envelope is quasi-steady and the radiated tails extend over a long distance in comparison with the envelope lengthscale $1/\epsilon$, as assumed in the asymptotic theory.

In the weakly nonlinear regime ($\epsilon \ll 1$), we may then attempt a comparison of the asymptotic result (5.29) with the tails radiated by a pulse, initially in the form of an NLS solitary wave group given by expansion (5.15), as it evolves towards the quasi-steady state that the analysis predicts. For this purpose, the carrier wavenumbers $k_0 = 0.4$ and $k_0 = 0.75$ are chosen again so the $n = 2$ and the $n = 0$ resonances, respectively, contribute

resonance	ϵ	predicted	numerical
$n = 2$	0.0050	1.5E − 4	9.0E − 5
	0.0045	4.5E − 5	3.5E − 5
	0.0040	9.8E − 6	9.8E − 6
$n = 0$	0.0140	6.6E − 4	2.0E − 4
	0.0113	6.7E − 5	4.5E − 5
	0.0100	1.4E − 5	1.2E − 5

TABLE 5–2. **Comparison of asymptotically predicted and numerically determined tail amplitudes for the $n = 2$ and $n = 0$ resonances.**

the dominant tails. The numerically determined tail amplitudes are averages over 300 cycles in the $n = 2$ case and 100 cycles in the $n = 0$ case; this averaging was done after the tails had formed clearly, specifically at time $t = 6000 - 7000$ for the $n = 2$ resonance and $t = 8000 - 9500$ for the $n = 0$ resonance. For the relatively small values of ϵ considered here, only one peak corresponding to the dominant radiated wavenumber according to the resonance conditions (5.19) was visible in the wavenumber spectrum. The comparisons are summarized in Table 5–2.

As expected, agreement between the asymptotic and numerical results improves as ϵ is decreased. On the other hand, for larger values of ϵ, like those used in the simulations depicted in Figures 2 and 4, the asymptotic expression (5.29) grossly overpredicts the tail amplitude.

Although radiation damping of the main pulse occurs on an exponentially long (with respect to ϵ) time scale, it is worth emphasizing that the radiated tails develop on a much shorter time scale: as discussed in Section 5–4, the spatial extent of a radiation front with wavenumber $k_*^{(n)}$ is controlled by the relative group speed $c_g(k_*^{(n)}) - c_g(k_0)$ which is essentially independent of ϵ. This fact must be kept in mind when assessing the usefulness of the NLS approach for modelling the long-time dynamics of weakly nonlinear pulses which, according to the NLS theory, evolve on an $O(1/\epsilon^2)$ time scale. For instance, if we consider the example with carrier wavenumber $k_0 = 0.4$ discussed in Section 5–4 in which the pulse has moderate steepness ($\epsilon = 0.01$), we find that $1/\epsilon^2 = 10,000$ while it is clear from Figure

5–2 that after only $t = 750$ the initial signal has been modified substantially owing to the radiated tails, and this would be completely missed by the NLS equation. On the other hand, for a pulse with a very small steepness the radiation amplitude is entirely negligible and the NLS approach is certainly adequate.

Apart from the fifth-order KdV equation, the mechanism explored here for the generation of tails is expected to be applicable in general to nonlinear dispersive wave systems that admit NLS envelope solitons to leading order. From the resonance conditions (5.19) it is relatively straightforward to predict the wavenumbers that will be radiated by a pulse in a given system but there is no simple criterion, besides direct numerical simulation, to decide whether the radiation amplitude will be significant for moderate values of the pulse steepness. A relative measure, however, may be developed using the current study as a guideline. In particular, it may suffice to determine the form of the exponential factor appearing in (5.29) which is the dominant controlling factor of the radiation amplitude; this requires carrying the asymptotic analysis as far as (5.21) and computing the values of $\kappa_*^{(n)}$ which are easily related to the tail wavenumbers $k_*^{(n)}$.

Theoretically, the fact that an initially locally confined solitary wave pulse of the NLS type radiates tails of non-decaying amplitude indicates that nonlinear wave pulses with envelopes of permanent form, as predicted by the NLS equation, would fail to be locally confined in general owing to exponentially small terms. Evidence of this nonlocal behavior has also been presented in a study by Bryant 1984 who investigated oblique wave groups in deep water numerically without invoking the narrow-band assumption. Starting with periodic wave groups, he approached, in the large envelope length-to-carrier wavelength limit, a wave group close to an NLS envelope soliton but with additional small resonant peaks in the wavenumber spectrum. These resonant components satisfied the dispersion relation for deep water waves and amounted to small-amplitude waves outside of the main group.

Nevertheless, it is now known that there exist special circumstances under which locally confined pulses can be obtained. In the case of the fifth-order KdV equation for instance, steady locally confined wavepackets in the form of solitary waves are possible near the minimum of the phase speed (at $k_0 = 1/\sqrt{2}$) where the phase speed and the group speed can be made equal, and the same is true near the minimum of the gravity–capillary phase speed in the water-wave problem.

CHAPTER 6

CONCLUDING REMARKS

In this thesis, the dynamics and stability of gravity–capillary solitary waves in both the small and large-amplitude regimes of the free-surface and interfacial-wave problems have been studied. In addition, the stability of small-amplitude solitary waves was briefly discussed in the context of solid mechanics using a nonlinear Bernoulli–Euler beam equation.

In Chapter 2, it was demonstrated how instability of this new class of solitary wave cannot be captured without accounting for exponentially small effects: an analysis using the NLS equation, derived using straightforward two-scale perturbation theory, is inadequate. In all three problems, it was found that of the two types of solitary wave solutions that bifurcate from zero amplitude, only one is stable: depression waves in the free-surface problem, depression waves for the quadratic-beam problem, symmetric waves in the modified KdV case, and elevation waves in the interfacial-wave problem (provided the density ratio is high enough and the depth of the lower fluid is many times that of the upper fluid). Moreover, direct simulation of weakly nonlinear model equations indicate that stable gravity–capillary solitary waves have soliton properties, and it would be interesting to see if this situation is obtained in the fully nonlinear case. To probe this point further would require time-dependent simulation of the full hydrodynamic equations with surface tension.

Although exponentially small effects translate to very small growth rates near the bifurcation points, they tend to decide the stability of much of each solitary wave solution branch emanating from zero amplitude. Furthermore, as was seen in Chapter 3, a large-amplitude (stable) elevation wave solution was obtained after passing a limit point which resembled a pairing of two (stable) depression solitary waves and so effects which influence stability near the bifurcation point at zero amplitude appear to propagate through solution diagrams even at large amplitude.

In contrast to the exponentially small growth rates found in the small-amplitude free-wave problem, growth rates found in the forced-wave problem scale algebraically with the wave amplitude and can be captured by the forced NLS equation. This difference in growth rate order appears to be tied to translational invariance. Specifically, in the forced problem the crests of the solitary wave solution cannot be shifted relative to their envelope due to the presence of the localized pressure distribution. The phase of the solitary wave is therefore fixed by the pressure distribution: for a symmetric pressure distribution, either depression or elevation wave types are possible depending on the sign of the pressure, and so it is not necessary to resort to exponential asymptotics to resolve the phase. Given the apparent connection between the accuracy needed to resolve phase details in the steady free-wave problem and the accuracy needed to determine instability (as was shown in Chapter 2), this interpretation seems plausible.

The instability of forced solitary waves found in Chapter 3 have interesting physical implications. Although experiments have indicated that some solitary depressions in the water surface can be found that are in good agreement with free-wave profiles (Zhang 1995;1999), albeit in the presence of wind forcing, these depressions do not appear to be generated as resonantly as other short-scale features such as parasitic capillary waves. In particular, at low wind speeds before parasitic capillaries riding on gravity waves begin to appear, one might expect the free surface to be populated with depression solitary waves initiated by pressure fluctuations in the air but this is not observed. The instability that has been found in the forced problem may play a role, but a precise explanation would need to account for the details of the often complicated and unsteady wind field.

From the analysis of Chapter 3, it is clear that viscous effects can be very important in describing the dynamics of steep solitary waves; although, when the pressure amplitude is large unstable effects do tend to be larger than viscous effects. Nevertheless, a formulation that takes into account viscosity and forcing in a coupled manner would be desirable for predicting steady-state response curves and stability when the pressure amplitude is only moderate. This type of formulation has been carried out for the steep periodic gravity–capillary water-wave problem by Fedorov & Melville (1998).

In Chapter 4, it was demonstrated that gravity–capillary interfacial solitary waves of the elevation type appear to be stable over a wide range of density ratios and Weber numbers provided that the depth of the lower fluid is many times that of the upper fluid. The results presented here may be helpful in planning experiments on interfacial solitary waves of this new kind. The effects of viscosity, however, are expected to be important and an evaluation of dissipative effects similar in spirit to that performed in Chapter 3 would be helpful.

Finally, in Chapter 5 it was demonstrated that the existence of wavepackets with solitary envelopes appears to be the exception more than the rule: resonances which lie beyond the narrow-band approximation lead to nonlocal envelope solitons. Gravity–capillary solitary waves appear to be the exception; in this case, a wavepacket with a solitary envelope can be obtained to all orders of approximation.

APPENDIX A

TIME-DEPENDENT NUMERICAL SOLUTION OF THE FIFTH-ORDER KDV AND BENJAMIN EQUATIONS

Here, the key details of the numerical methods used to solve the time-dependent fifth-order KdV equation (used in Chapters 2 and 5) and the time-dependent Benjamin equation (used in Chapter 4) are presented.

A.1 Fifth-order Korteweg–de Vries equation

A split-step Fourier pseudospectral method (Tappert 1974) was used that is similar to the technique presented in Lo (1986) to solve a higher-order NLS equation. A review of split-step schemes for the KdV and NLS equations can be found in Taha & Ablowitz (1984). General background on pseudospectral methods can be found in the book by Fornberg (1995).

The split-step algorithm to solve the fifth-order KdV equation

$$u_t + u_{xxx} + u_{xxxxx} + 6uu_x = 0 \qquad (A.1)$$

consists of advancing the initial condition a full time step by first using only the nonlinear part of the equation (by a predictor-corrector method in this case), and then modifying this result using the linear part of the equation (exactly in Fourier space).

Labelling the spectral representation of $u(x)$ (which is collocated on a uniformly spaced grid) at time level n as u^n, the discrete Fourier transform of u^n may be represented symbolically as $\mathcal{F}\{u^n\}$ (see Fornberg 1996, Appendix F). The sequence of numerical steps to propagate from level n to level $n+1$ separated by a time step Δt reads:

Nonlinear step — a half step (predictor of u at n + 1/2):

$$\bar{u}^{n+1/2} = u^n - \frac{\Delta t}{2}\, u^n \mathcal{F}^{-1}\{\mathrm{i}k\mathcal{F}\{u^n\}\}, \tag{A.2}$$

Nonlinear step — the full step (derivative based on the estimate of u at n + 1/2):

$$\tilde{u}^{n+1} = u^n - \Delta t\, \bar{u}^{n+1/2}\mathcal{F}^{-1}\{\mathrm{i}k\mathcal{F}\{\bar{u}^{n+1/2}\}\}, \tag{A.3}$$

Linear step:

$$u^{n+1} = \mathcal{F}^{-1}\{\exp[\mathrm{i}(k^3 - k^5)\Delta t]\mathcal{F}\{\tilde{u}^{n+1}\}\}. \tag{A.4}$$

The sequence then repeats in the same order. This scheme is accurate to second order in Δt and to all orders in Δx since the differentiation step is exact given a finite number of Fourier modes. A large enough computational domain (typically 7 pulse widths) must be used, however, so that the wave disturbance does not reach the boundaries. Given this domain size, a large enough number of modes must be used such that any high-frequency information lying above the Nyquist frequency which might be present in the actual continuous problem is small.

A.2 Benjamin equation

From Chapter 4, the Benjamin equation reads

$$u_t - 2uu_x - 2\gamma\mathcal{H}(u_{xx}) - u_{xxx} = 0. \tag{A.5}$$

The spatial derivatives on a uniform grid were approximated using the fourth-order accurate finite-differences (Chapra & Canale 1988):

$$u_{x,i} = (-u_{i+2} + 8u_{i+1} - 8u_{i-1} + u_{i-2})/(12\Delta x), \tag{A.6}$$

$$u_{xx,i} = (-u_{i+2} + 16u_{i+1} - 30u_i + 16u_{i-1} - u_{i-2})/[12(\Delta x^2)], \qquad (A.6)$$

$$u_{xxx,i} = (-u_{i+3} + 8u_{i+2} - 13u_{i+1} + 13u_{i-1} - 8u_{i-2} + u_{i-3})/[8(\Delta x^3)], \qquad (A.7)$$

while the computation of the Hilbert transform was performed using a discrete Fourier transform implemented in MATLAB. Alternatively, a completely spectral approach can be taken but using finite-differences provides better flexibility in adjusting the domain size.

Rewriting (A.5) as

$$u_t = S^n(u^n), \qquad (A.8)$$

the explicit time stepping scheme applied at each node i reads

$$\tilde{u}^{n+1/2} = u^n + \frac{\Delta t}{2} S^n, \qquad (A.9)$$

$$u^{n+1} = u^n + \Delta t \tilde{S}^{n+1/2} \qquad (A.10).$$

This scheme is $O[(\Delta t)^2]$ accurate and is stable provided that $\Delta t \leq 0.05(\Delta x)^3$. Note that because the highest derivative is only third order in this case, stability requirements are not unreasonable (especially using fourth-order spatial differences). In the fifth-order KdV case, however, stability requirements imposed by a finite-difference spatial approach would render the time step size impractical.

APPENDIX B

SOLUTION OF FORCED PROBLEMS ARISING FROM PERTURBATION EXPANSIONS OF CHAPTER 2

Upon substitution of expansions (2.44), (2.45) and (2.46) into (2.43) and collecting terms proportional to $e^{i\theta}$, $e^{i2\theta}$ and 1 it is found that

$$\frac{i}{\sqrt{2}}[q - q_{XX} + 3(\bar{A}_0\, q - 24(\bar{A}^2 q^* + |\bar{A}|^2 q) - \frac{8}{3}|\bar{A}|^2 q + \bar{A}_2 q^*)] = f(X),$$

$$q_2 = -\frac{8}{3}\bar{A} q + O(\epsilon),$$

$$q_0 = -24(\bar{A} q^* + \bar{A}^* q) + O(\epsilon).$$

Using the fact that $\bar{A}_0 = -24|\bar{A}|^2$ and $\bar{A}_2 = -\frac{4}{3}\bar{A}^2$, q is then found to satisfy

$$q - q_{XX} - 76(\bar{A}^2 q^* + 2|\bar{A}|^2 q) = -\frac{i}{\sqrt{2}} f(X),$$

with

$$\bar{A} = \frac{1}{\sqrt{38}}\,\mathrm{sech}X.$$

Considering first the $O(\lambda)$ problems, the forced problem for $U_1^{(1)}$ reads, using the notation $S \equiv \mathrm{sech}X$ and $R \equiv \tanh X$,

$$q - q_{XX} - 6S^2 q = -\frac{1}{\sqrt{76}}\, S, \tag{2.52}$$

which has the solution $q = -\frac{1}{2\sqrt{76}}(XSR - S)$. The forced problem for $U_2^{(1)}$ reads

$$q - q_{xx} - 2S^2(2q + q^*) = -\frac{i}{\sqrt{76}}\, SR$$

which has the solution $q = -\frac{i}{2\sqrt{76}} XS$. The solutions for $U_1^{(1)}$ and $U_2^{(1)}$ are then given by

$$U_1^{(1)} = -\frac{1}{\sqrt{76}\,\epsilon}\,(XSR - S)\cos\theta,$$

$$U_2^{(1)} = \frac{1}{\sqrt{76}\,\epsilon}\,XSR\sin\theta.$$

Proceeding to the $O(\lambda^2)$ problems, it is found that the forced problem for $U_1^{(2)}$ reads

$$q - q_{xx} - 2S^2(2q + q^*) = \frac{1}{4\sqrt{38}\epsilon^2}\,XS,$$

and has the general solution

$$q = \frac{C_1}{\epsilon^2}\,SR + \frac{C_2}{\epsilon^2}\,(XSR + \frac{1}{3\,S} - S) + \frac{1}{16\sqrt{38}\,\epsilon^3}(X^2SR - 2XS - \frac{R}{S}).$$

The forced problem for $U_2^{(2)}$ reads

$$q - q_{XX} - 2S^2(2q + q^*) = \frac{\mathrm{i}}{4\sqrt{38}\epsilon^2}\,(XSR - S),$$

and has the general solution

$$q = \frac{C_1}{\epsilon^2}\,S + \frac{C_2}{\epsilon^2}\,(XS + \frac{R}{S}) + \frac{\mathrm{i}}{16\sqrt{38}\,\epsilon^3}(X^2S - S - \frac{1}{S}).$$

Requiring that both $U_1^{(2)}$ and $U_2^{(2)}$ go to zero as $x \to -\infty$ it is found that

$$U_1^{(2)} \sim -\frac{1}{8\sqrt{38}\,\epsilon^3}\mathrm{e}^X\cos\theta \qquad (x \to \infty),$$

and

$$U_2^{(2)} \sim -\frac{1}{8\sqrt{38}\,\epsilon^3}\mathrm{e}^X\sin\theta \qquad (x \to \infty),$$

which feature the growing tails as expected.

APPENDIX C

CALCULATION OF EIGENVALUES AND UNSTABLE MODES

Discretizations of the linear stability problems encountered in this thesis result in generalized matrix eigenvalue problems:

$$[C]\mathbf{u} = \lambda[B]\mathbf{u}.$$

Except in the case of the interfacial-wave problem in which there is coupling between ϕ_{1t} and ϕ_{2t} stemming from the Bernoulli equation, $[B] = 1$.

The eigenvalue problem was first solved on a coarse grid using a global eigenvalue solver (EISPACK routines implemented on MATLAB). Based on estimates of the eigenvalues corresponding to unstable modes, the inverse power method with shifting (inverse iteration) was employed on a finer grid to improve the eigenvalue accuracy and mode shape resolution. The method (Fröberg 1965) is as follows. Provided that a random vector $\mathbf{x}_0$ can be represented as a linear combination of the eigenvectors, it follows that

$$\mathbf{x}_0 = a_0\,\mathbf{u}_0 + a_1\,\mathbf{u}_1 + \ldots + a_n\,\mathbf{u}_n.$$

Repeated multiplication by $[C]$ k-times yields

$$\mathbf{x}_k = [C]^k\mathbf{x}_0 = [B]^k[a_0\,\lambda_0^k\mathbf{u}_0 + a_1\,\lambda_1^k\mathbf{u}_1 + \ldots + a_n\,\lambda_n^k\mathbf{u}_n].$$

As $k \to \infty$, the term involving the largest eigenvalue dominates. If each time $\mathbf{x}_k$ is normalized by $||\,\mathbf{x}_k||_\infty$ then $||[B]^{-1}\mathbf{x}_{k+1}||_\infty$ tends to $|\lambda_{\max}|$ and $\mathbf{x}_{k+1}$ tends to the corresponding eigenvector.

To search for the smallest eigenvalue, the inverse problem can be considered

$$[C]^{-1}\mathbf{u} = \lambda^{-1}[B]^{-1}\mathbf{u}$$

so

$$\mathbf{x}_k = ([C]^{-1})^k \mathbf{x}_0 = ([B]^{-1})^k [a_0\,(\lambda_0^{-1})^k \mathbf{u}_0 + a_1\,(\lambda_1^{-1})^k \mathbf{u}_1 + \ldots + a_n\,(\lambda_n^{-1})^k \mathbf{u}_n].$$

and the smallest eigenvalue dominates. Because finding $[C]^{-1}$ is costly we may instead solve

$$[C]\mathbf{x}_k = [B]\frac{\mathbf{x}_{k-1}}{||\mathbf{x}_{k-1}||_\infty}$$

repeatedly. Since $[C]$ does not change, this requires only one LU decomposition. Finally, we may locate any eigenvalue λ_t of $[C]$ by shifting the eigenvalues by a quantity $\lambda_t{}'$ which is the initial guess for λ_t. Provided that $\lambda_t{}'$ is close to λ_t then the smallest eigenvalue of $[C]' = [C] - [B]\lambda_t{}'$ will be $\lambda_t - \lambda_t{}'$ which can be found by the inverse power method. The eigenvalue of interest can then be found from

$$\lim_{k\to\infty} \mathbf{x}_{k,\text{imax}} = \frac{1}{\lambda_t - \lambda_t'}$$

where imax corresponds to the index of $||\mathbf{x}_k||_\infty$. In this study, when one LU decomposition was performed on $[C]'$, convergence was usually obtained within seven iterations. The rate of convergence could be increased by reshifting [C] by an improved value of $\lambda_t{}'$ found after three or so iterations. This caused $1/(\lambda_t - \lambda_t{}')$ to dominate even faster and so convergence could be obtained within five iterations.

APPENDIX D

DETAILS ON COMPUTATIONS PERFORMED IN CHAPTERS 3 & 4

Here details on software used, computational resources, and code performance are listed with a slant towards the more demanding computations performed in Chapters 3 and 4. The code to compute solitary-wave solutions was written in FORTRAN 77 and utilized LAPACK linear algebra routines available on Athena. The compiler command taking into account compiler optimization and linking to libraries reads

```
f77 -O5 codename.f -L/mit/lapack/sun4lib -llapack -lblas
```

for the Sun workstation platform. Compiler optimization (-O5) was extremely important as it nearly doubled execution time.

To compute a well converged solitary wave solution for the free-surface problem on a Sun Ultra 10 workstation using a good initial guess, $N = 650$ grid points, and going through 5 iterations took about 6.5 minutes. This resolution was more than adequate to explore solution diagrams which was usually done with $N = 400$ points. To obtain well converged stability results, however, the underlying solitary wave solution had to be refined further. For $N = 1200$ for instance, a solitary wave refinement can usually be performed on a Sun Ultra 10 in about 42 minutes.

Computations first become mostly costly for the stability problem. For $N > 600$ for example, a Sun Ultra 10 does not have enough free RAM to perform the computation without using the hard drive for memory which slows the computations to an impractical speed. For these larger problems the NCSA SGI/Cray *Origin2000* supercomputing array was used where large blocks of memory were easily available. Further information on this resource can be found at the NCSA web page *http://www.ncsa.uiuc.edu/*.

If solitary wave profiles had to be further refined, this could be done on the *Origin2000* in a matter of minutes (typically using 8 processors). For the stability calculations, the MATLAB compiler and MATLAB C/C^{++} software library (available at NCSA) were used to compile the MATLAB .m files into stand-alone C language executables which could be run on the *Origin2000.*

REFERENCES

ABLOWITZ, M.J. & CLARKSON, P.A. 1991 *Solitons, nonlinear evolution equations and inverse scattering*, London Mathematical Society Lecture Notes, 149, Cambridge: Cambridge University Press 516pp.

AKYLAS, T.R. 1984 On the excitation of nonlinear water waves by a moving pressure distribution oscillating at resonant frequency. *Phys. Fluids* **27**, 2803–2807.

AKYLAS, T.R. 1989 Higher-order modulation effects on solitary wave envelopes in deep water. *J. Fluid Mech.* **198**, 387–397.

AKYLAS, T.R. & KUNG, T.-J. 1990 On nonlinear wave envelopes of permanent form near a caustic. *J. Fluid Mech.* **214**, 489–502.

AKYLAS, T.R. & GRIMSHAW, R.H.J. 1992 Solitary internal waves with oscillatory tails. *J. Fluid Mech.* **242**, 279–298.

AKYLAS, T.R. 1993 Envelope solitons with stationary crests. *Phys. Fluids A* **5**, 789–791.

AKYLAS, T.R., DIAS, F., & GRIMSHAW, R.H.J. 1998 The effect of the induced mean flow on solitary waves in deep water. *J. Fluid Mech.* **355**, 317–328.

ALBERT, J.P., BONA, J.L. & RESTREPO 1999 Solitary-wave solutions of the Benjamin equation. *SIAM Jl Appl. Math.***59** 2139-2161.

ARANHA, J.A., YUE, D.K.P, & MEI, C.C. 1982 Nonlinear waves near a cut-off frequency in an acoustic duct – a numerical study *J. Fluid Mech.* **121**, 465–485.

BARNARD, B.J.S., MAHONY, J.J., & PRITCHARD, W.G. 1977 The excitation of surface waves near a cut-off frequency. *Phil. Trans. Roy. Soc. Lond.* **286**, 87–123.

BENNEY, D.J. & NEWELL, A.C. 1967 The propagation of nonlinear wave envelopes. *J. Math. & Phys.* **46** 133–139.

BENJAMIN, T.B. 1967 Internal waves of permanent form in fluids of great depth. *J. Fluid Mech.* **29**, 559–592.

BENJAMIN, T.B. 1992 A new kind of solitary wave. *J. Fluid Mech.* **245**, 401–411.

BENJAMIN, T.B. 1996 Solitary and periodic waves of a new kind. *Phil. Trans. R. Soc. Lond. A* **354**, 1775–1806.

BRYANT, P.J. 1984 Oblique wave groups in deep water. *J. Fluid Mech.* **146**, 1–20.

BUFFONI, B., CHAMPNEYS, A.R., & TOLAND, J.F. 1995 Bifurcation and coalescence of a plethora of homoclinic orbits for a Hamiltonian system. *J. Dynamics Diff. Eqns* **8**, 221–281.

BUFFONI, B., GROVES, M.D., & TOLAND, J.F. 1996 A plethora of solitary gravity–capillary water waves with nearly critical Bond and Froude numbers. *Phil. Trans. R. Soc. Lond. A* **354**, 575–607.

BURYAK, A.V. & CHAMPNEYS, A.R. 1997 On the stability of solitary wave solutions of the fifth-order KdV equation. *Phys. Lett. A* **233**, 58–62.

CALVO, D.C. 2000 Dynamics and stability of gravity–capillary solitary waves. PhD Thesis, MIT.

CALVO, D.C., YANG, T.-S. & AKYLAS, T.R. 2000 On the stability of solitary waves with decaying oscillatory tails. *Proc. Royal Soc. Lond.* **456**, 469-487.

CHAMPNEYS, A.R., HUNT, G.W. & THOMPSON, J.M.T. 1997 Localization and solitary waves in solid mechanics. *Phil. Trans. R. Soc. Lond. A* **355**, 2077–2081.

CHAMPNEYS, A.R. & TOLAND, J.F. 1993 Bifurcation of a plethora of multi-modal homoclinic orbits for autonomous Hamiltonian systems. *Nonlinearity* **6**, 665–722.

CHAPRA, S.C. & CANALE R.P. 1988 *Numerical methods for engineers*, New York: McGraw–Hill.

CHEN, Y. & MCKENNA, P.J. 1997 Travelling waves in a nonlinearly suspended beam: some computational results and four open questions. *Phil. Trans. R. Soc. Lond. A* **355** 2175-2184.

CRAIK, A.D.D. 1985 *Wave Interactions and Fluid Flows*, Cambridge: Cambridge University Press 322pp.

DIAS, F. & KHARIF, C. 1999 Nonlinear gravity and capillary–gravity waves. *A. Rev. Fluid Mech.* **31**, 301-346.

DIAS, F. & KUZNETSOV, E.A. 1999 On the nonlinear stability of solitary wave solutions of the fifth-order Korteweg–de Vries equation. *Phys. Lett. A* **263**, 98–104.

DIAS, F., MENASCE, D. & VANDEN-BROECK, J.-M. 1996 Numerical study of capillary-gravity solitary waves. *Eur. J. Mech. B/Fluids* **15**, 17–36.

FEDOROV, A.V. & MELVILLE, W.K. 1998 Nonlinear gravity-capillary waves with forcing and dissipation. *J. Fluid Mech.* **354**, 1–42.

FORNBERG, B. 1995 *A Practical Guide to Pseudospectral Methods.* Cambridge University Press.

FRÖBERG, C.-E. 1965 *Introduction to Numerical Analysis.* Addison-Wesley.

GRIMSHAW, R., MALOMED, B., & BENILOV, E. 1994 Solitary waves with damped oscillatory tails: an analysis of the fifth-order Korteweg-de Vries equation. *Physica D* **77**, 473–485.

HASEGAWA, A. 1989 *Optical Solitons in Fibers*, Berlin: Springer-Verlag 75pp.

HASEGAWA, A. & TAPPERT, F.D. 1973 Transmission of stationary nonlinear optical pulses in dispersive dielectric fibers. I. Anomalous dispersion. *Appl. Phys. Lett.* **23**, 142–144.

HUNT, G.W., BOLT, H.M. & THOMPSON J.M.T. 1989 Structural localization phenomena and the dynamical phase-space technology. *Proc. R. Soc. Lond. A* **425**, 245–267.

HUNTER, J.K. & SCHEURLE, J. 1988 Existence of perturbed solitary-wave solutions to a model equation for water waves *Physica D* **32**, 253–268.

IOOSS, G. & KIRCHGÄSSNER, K. 1990 Bifurcations d'ondes solitaires en presence d'une faible tension superficielle. *C.R. Acad. Sci. Paris* **311**. (Sér. 1), 265–268.

KLAUDER, M., LAEDKE, E.W., SPATSCHEK, K.H., & TURITSYN, S.K. 1993 Pulse propagation in optical fibers near the zero dispersion point. *Phys. Rev. E* **47**, R3844–R3847.

LAGET, O. & DIAS, F. 1997 Numerical computation of capillary-gravity interfacial solitary waves. *J. Fluid Mech.* **349**, 221–251.

LANDAU, L.D. & LIFSHITZ, E.M. 1965 *Quantum Mechanics*, Pergamon Press.

LINDBERG, H.E. & FLORENCE, A.L. 1987 *Dynamic pulse buckling: theory and experiment*, Dordrecht.

LO, E. 1985 Long-time evolution of surface waves in coastal waters. PhD Thesis, MIT.

LO, E. & MEI, C.C. 1985 A numerical study of water-wave modulation based on a higher-order nonlinear Schrödinger equation. *J. Fluid Mech.* **150**, 395–416.

LONGUET-HIGGINS, M.S. 1989 Capillary-gravity waves of solitary type on deep water. *J. Fluid Mech.* **200**, 451–470.

LONGUET-HIGGINS, M.S. 1993 Capillary–gravity waves of solitary type and envelope solitons on deep water. *J. Fluid Mech.* **252**, 703–711.

LONGUET-HIGGINS, M.S. 1995 Parasitic capillary waves: a direct calculation. *J. Fluid Mech.* **301**, 79–107.

LONGUET-HIGGINS, M.S. 1997 Viscous dissipation in steep capillary–gravity waves. *J. Fluid Mech.* **344**, 271–289.

LONGUET-HIGGINS, M.S. & ZHANG, X. 1997 Experiments on capillary–gravity waves of solitary type on deep water. *Phys. Fluids A* **9**, 1963–1968.

MALOMED, B. & VANDEN-BROECK, J.-M. 1996 Solitary wave interactions for the fifth-order KdV equation. *Contemp. Math.* **200**, 133–143.

MOLLENAUER, L.F., STOLEN, R.H., & GORDON, J.P. 1980 Experimental Observation of Picosecond Pulse Narrowing and Solitons in Optical Fibers. *Phys. Rev. Lett.* **45**, 1095–1098.

NEWELL, A.C. 1985 *Solitons in Mathematics and Physics*, Philadelphia: SIAM 244pp.

ONO, H. 1975 Algebraic solitary waves in stratified fluids. *J. Phys. Soc. Japan* **39**, 1082–1091.

PERLIN, M., LIN, H., & TING, C.-L. 1993 On parasitic capillary waves generated by steep gravity waves: an experimental investigation with spatial and temporal measurements. *J. Fluid Mech.* **255**, 597–620.

POMEAU, Y., RAMANI, A., & GRAMMATICOS, B. 1988 Structural stability of the Korteweg-de Vries solitons under perturbation. *Physica D* **31**, 127–134.

SAFFMAN, P.G. & YUEN, H.C. 1978 Stability of a plane soliton to infinitesimal two-dimensional perturbations. *Phys. Fluids* **21**, 1450–1451.

SANDSTEDE, B. 1997 Instability of localized buckling modes in a one-dimensional strut model. *Phil. Trans. R. Soc. Lond. A* **355**, 2083–2097.

SHEMER, L. & CHAMESSE, M. 1999 Experiments on nonlinear gravity–capillary waves. *J. Fluid Mech.* **380**, 205–232.

SU, M.Y. 1982 Evolution of groups of gravity waves with moderate to high steepness. *Phys. Fluids* **26**, 2167–2174.

TAHA, T.R. & ABLOWITZ, M.J. 1984 Analytical and numerical aspects of certain nonlinear evolution equations, III. Numerical, Korteweg-de Vries equation. *J. Comp. Phys.* **55**, 231.

TANAKA, M. 1986 The stability of solitary waves. *Phys. Fluids* **29**, 650–655.

TAPPERT, F. 1974 *Lect. Appl. Math. Am. Math. Soc.* **15**, 215.

VANDEN-BROECK J.-M. & DIAS, F. 1992 Gravity–capillary solitary waves in water of infinite depth and related free-surface flows *J. Fluid Mech.* **240**, 549–557.

WAI, P.K.A., MENYUK, C.R., LEE, Y.C., & CHEN, H.H. 1986 Nonlinear pulse propagation in the neighborhood of the zero-dispersion wavelength of monomode optical fibers. *Optics Letters* **11**, 464–466.

WHITHAM, G.B. 1974 *Linear and Nonlinear Waves* Wiley-Interscience.

YANG, T.-S. & AKYLAS, T.R. 1996 Weakly non-local gravity-capillary solitary waves. *Phys. Fluids* **8**, 1506–1514.

YANG, T.S. 1996 Nonlinear interaction of long-wave disturbances with short-scale oscillations in stratified flows. PhD Thesis, MIT.

YANG, T.-S. & AKYLAS, T.R. 1997 On asymmetric gravity–capillary solitary waves. *J. Fluid Mech.* **330**, 215–232.

ZAKHAROV, V.E. & RUBENCHIK, A.M. 1974 Instability of waveguides and solitons in nonlinear media. *Sov. Phys.-JETP* **38**, 494–500.

ZHANG, X. 1995 Capillary–gravity and capillary waves generated in a wind wave tank: observations and theories. *J. Fluid Mech.* **289**, 51–82.

ZHANG, X. 1999 Observations on waveforms of capillary and gravity–capillary waves. *Eur. J. Mech. B/Fluids* **18**, 373–388.

ZUFIRIA, J.A. 1987 Symmetry breaking in periodic and solitary gravity–capillary wave on water of finite depth. *J. Fluid Mech.* **184**, 183–206.